

P-118

Copy Number 045

NASA CR 174791

(NASA-CR-174791) SR-7A AEROELASTIC MODEL
DESIGN REPORT (Hamilton Standard) 118 p
CSCL 21E

N88-28928

G3/07 Unclas
0164890

NASA
SR-7A AEROELASTIC MODEL DESIGN REPORT
October 1986

Prepared by: D. Nagle
S. Auyeung
J. Turnberg

HAMILTON STANDARD
UNITED TECHNOLOGIES CORPORATION

Prepared for
National Aeronautics and Space Administration
NASA-Lewis Research Center
Contract NAS3-23051



SR-7A AEROELASTIC MODEL DESIGN REPORT
October 1986

Prepared by: D. Nagle
S. Auyeung
J. Turnberg

HAMILTON STANDARD
UNITED TECHNOLOGIES CORPORATION

Prepared for
National Aeronautics and Space Administration
NASA-Lewis Research Center
Contract NAS3-23051

TABLE OF CONTENTS

<u>SUBJECT</u>	<u>PAGE</u>
1.0 SUMMARY	1
2.0 INTRODUCTION	3
2.1 Origin of Prop-Fans	3
2.2 Origin of SR-7L and Aeroelastic Model	3
2.3 Analytical Methodology	4
3.0 REQUIREMENTS AND GOALS	5
4.0 SELECTION OF AEROELASTIC MODEL	7
4.1 Similarity Requirements for Aeroelastic Models	7
4.2 Retention Stiffness Scaling	9
4.3 Origin of New-construction Model Blade	11
4.4 Finite Element Modeling Iterations	12
5.0 FINAL BLADE CONCEPT	15
6.0 STRUCTURAL EVALUATION	17
6.1 Methodology	17
6.2 Analytical Results	21
7.0 HUB AND SPINNER	29
7.1 Blade Retention Design	29
7.2 Blade Retention Loads and Stresses	30
7.3 Hub Lip Stresses	31
7.4 Bolt Stresses	32
8.0 PITCH CHANGE MECHANISM	33
8.1 Blade Angle Adjustments	33
8.2 Blade Twisting Loads	34
8.3 Blade Pitch Adjustment Pins	35
8.4 Face and Blade Gears Stresses	36
9.0 CONCLUSIONS	39
APPENDIX A Blade Angle Setting Table	41
APPENDIX B Figures	47
APPENDIX C Tables	111
APPENDIX D Design Layouts	117
REFERENCES	123

1.0 SUMMARY

A .62 meter (2 ft) diameter Prop-Fan model has been designed to simulate the aeroelastic characteristics of the 2.74 meter (9 ft) diameter SR-7L Prop-Fan. The model is to be tested first in a wind tunnel at the NASA Lewis Research Center and then at high altitude, 10668 m (35,000 ft), mounted atop a NASA Jetstar aircraft. Since it will be tested in advance of the large-scale Prop-Fan, the model should provide valuable preliminary information about the aeroelastic behavior of the large Prop-Fan.

The model blade construction consists of a shortened, solid, titanium spar, covered with a fiberglass shell, locally reinforced with graphite. This differs from the large blade, which has a full-length, solid, aluminum spar and an all fiberglass shell, with rigid foam fill. The differences are due to manufacturing and dimensional tolerance limitations arising from the 4.5/1 reduction in size between both designs. For similar reasons, the bending flexibility of the large blade, ball-bearing retention was approximated with a fixed, small diameter, extended length, model blade shank. This led to the use of titanium as the spar material, for increased fatigue endurance. Also, the minimum thickness required for resin injection of the shell, coupled with a thin tip on this blade, forced a reduction in spar length to about 2/3 the span. The loss of spar tip stiffness and mass in the model was offset by the addition of a few bridging plies of graphite in the shell and the use of solid fiberglass fill in the tip, respectively. This blade matches the scaled mass and stiffness distributions of the large blade relatively well.

Results of finite element and stability analyses show that, for the high-altitude Jetstar test case, the aeroelastic characteristics of the model blade match those of the large blade very well, thus satisfying the primary objective of this design effort. The match for the wind tunnel case is less desirable, however, because the air density is high, causing a reduction in high speed flutter stability. Application of new empirical factors, derived from recent tests on composite blade Prop-Fan models, shows that though it is marginal, the aeroelastic model stability should be adequate up to 0.8 Mach number, required to evaluate aerodynamic performance in the wind tunnel.

Stress results show that the model blade, hub, and pitch change components can be safely operated at all test conditions analyzed. However, since stress analyses were limited to steady-state conditions, model blade cyclic stresses should be monitored in key stress regions. Calculated steady stress levels are moderate, and sufficient cyclic stress capacity should exist for most conditions. However, if tests are planned at significantly different operating conditions, further analyses should be conducted to re-establish key steady stresses and corresponding levels of allowable cyclic stress.

2.0 INTRODUCTION

2.1 Origin of Prop-Fans

The Aircraft Energy Efficiency (ACEE) Program was funded by Congress in 1975. This program, directed by NASA, was established to increase the fuel efficiency of subsonic commercial aircraft. Of the concepts studied to achieve this goal, the Advanced Turboprop offers the greatest potential fuel savings. For years, turboprops have been providing transportation efficiently at speeds up to Mach .6 and altitudes up to 6096 meters (20,000 feet).

The Advanced Turboprop Program (ATP) was created to develop the technology required for efficient, reliable, and acceptable operation of advanced turboprop-powered aircraft at cruise speeds and altitudes up to Mach .8 and 9144 meters (30,000 feet) respectively. At the same time cabin comfort levels (noise and vibration) will have to be similar to those of modern turbofan-powered aircraft. Results of previous engine studies have shown that the use of multi-bladed, swept-tip propellers, called Prop-Fans, extends the efficiency advantage of turboprop propulsion systems to the higher speeds required. Potential fuel savings of 15 to 20 percent can be obtained using turboprop aircraft equipped with Prop-Fans, as opposed to turbofans with the same level of core engine technology. Relative to current in-service turbofan powered aircraft, this would be a 30 to 40 percent fuel savings.

2.2 Origin of SR-7L and Aeroelastic Model

The feasibility of the high-speed (.7 to .8 Mach no) turboprop concept was verified early under the ATP using small scale propeller models. Although high levels of aerodynamic performance were obtained with these models, the Large-scale Advanced Prop-Fan or LAP program was created to develop technology for testing a large scale Prop-Fan in a real flow environment. This large scale Prop-Fan was designated SR-7L. Because the SR-7L will simulate as closely as possible a full scale Prop-Fan, it will be similar in construction. The blades will be lightweight composite structures which are very sensitive to steady and dynamic air loads. These elastic structures are therefore more likely to encounter flutter than the heavier and stiffer metal blades used for past models.

It is for this reason that a small scale aeroelastic model, 62.23 cm. (24.5 inch) tip diameter, designated SR-7A, will be constructed. Properly designed, the model should behave like the SR-7L at the same operating conditions. If the aeroelastic characteristics of the model, determined by analysis, are confirmed by testing, it is assumed that the behavior of the SR-7L, designed with the same analytical techniques and similar in construction, can be correctly predicted.

2.3 Analytical Methodology

In early Prop-Fan studies at Hamilton Standard, beam programs were determined to be insufficient for structural analysis of the geometrically complex (wide, thin, and swept) Prop-Fan blades. An in-house FEA (finite element analysis) computer code, BESTRAN, was selected to analyze the aeroelastic model blade because it offers pre- and post-processing capabilities for geometry and stress data. It was used for steady state stress analysis and for computing the stiffness and mass matrices used in subsequent vibration analysis. MSC/NASTRAN, with its more efficient eigenvalue solver, was used to calculate natural frequencies and mode shapes.

The preliminary FEA model of the blade was first developed by direct scaling of an SR-7L blade FEA model. As model blade construction methods were refined, and the final static shape of the SR-7L blade was determined, a completely new FEA model of the SR-7A model blade was developed. The external shape of the new model was scaled directly from that of the large blade, but the internal structure was varied to meet manufacturing and retention constraints, due to the smaller size. Several iterations of the internal structure were required to obtain the final match of deflection and aeroelastic characteristics of the SR-7L blade.

3.0 REQUIREMENTS AND GOALS

The main objective of this design effort is to simulate the aeroelastic characteristics of the SR-7L by means of a small-diameter scale model. It was established that the aeroelastic model be an eight-bladed configuration with a tip diameter of 62.23 cm. (24.5 inches). The hub and spinner contours are to match the spinner contour of the SR-7L (i.e., dimensions of the SR-7L spinner are scaled down by the ratio of the tip diameters - $62.23/274.32 = .22685$). Similarly, the external shape of the blade (statically) is to match that of the 2.74 meter (9 foot) diameter SR-7L blade. A pitch change mechanism is to be designed to adjust the blade angle (static, non-rotating adjustment only).

The aeroelastic model is to be tested on the Jetstar aircraft at the Model Design Condition 1 of Table 3-1. In order to simulate aeroelastic characteristics, the vibration characteristics (natural frequencies and mode shapes) and flutter behavior of the model must match, as closely as possible, those of the SR-7L blade at the same operating conditions. This is the primary design requirement for the model blade. This requirement is, of course, to be met within the practical limitations of materials, manufacturing, and design and analysis procedures.

Also desired is that the model be able to withstand testing in the NASA/Lewis 2.44 meter (8 ft.) by 1.83 meter (6 ft.) wind tunnel, so that the performance and stability of the model can be evaluated at wind tunnel conditions. Vibration and flutter analyses of the aeroelastic model must be performed at Model Design Condition 2 of Table 3-1 to predict behavior in the wind tunnel.

Finally, stress analysis of the model must be conducted to ensure that the blades are structurally capable of operating at tip speeds up to 290 meters/sec (950 fps). This is Model Design Condition 3 of Table 3-1.

Because this is a test model program, the model blade does not have to meet all the safety requirements of a full-scale blade which propels an aircraft. For instance, the extent of foreign object damage (FOD) was not investigated. Also, no sheath or erosion coating is required because the model will not be subjected to the high erosive environment normally encountered by propeller blades during ground maneuvering.

4.0 SELECTION OF AEROELASTIC MODEL

4.1 Similarity Requirements for Aeroelastic Models

To properly conduct a model test that will simulate the aeroelastic properties of the SR-7L, it is necessary to understand the parameters to be matched in order to determine the type of construction required for the simulation.

There are several basic parameters generally considered in evaluating scale model tests of rotating lifting surfaces. (See references 1 through 3). These are listed as follows:

- Mach Number
- Advance Ratio
- Reynolds Number
- Lock Number
- Cauchy Number
- Reduced Frequency
- Froude Number
- Aerodynamic Damping

The following discussions of these parameters are based on the assumption that all the geometry is scaled proportionately, i.e., the ratio of chord to blade radius and blade built-in twist remains the same. This assumption is valid based on the previous discussion of the requirement that the external blade shape of the aeroelastic model be exactly scaled down from the SR-7L.

In order to achieve proper aerodynamic similarity, the local blade section velocities need to be identical to those of the SR-7L. This is done by simultaneously maintaining the SR-7L tip-speed and advance ratio. Keeping the tip-speed constant requires that the rotational speed for the model be inversely proportional to the radius between configurations. Maintaining constant advance ratio means that forward speed remains constant.

Because the flow at forward speed involves local blade section velocities in the transonic range, it is important that the Reynolds Number be the same for the model and the SR-7L. The Reynolds Number is also important to high speed flows because of compressibility effects and boundary layer effects. Flows with different Reynolds Numbers will have shocks located on the blade sections at different positions, different types of flows in the boundary layer, and different attachment points.

Unfortunately, constant Reynolds Numbers cannot be maintained easily at the same time that Mach Number and density ratios are kept constant. Reynolds Number is defined as follows:

$$RE = \rho Vc / \mu \quad \text{where: } \begin{array}{l} \rho = \text{air density} \\ V = \text{air velocity} \\ c = \text{chord length} \\ \mu = \text{absolute viscosity of air} \end{array}$$

indicating proportionality to length for constant velocity. Because altitude, tip-speed, and forward velocities are constant, the ratio of the Reynolds Number is equal to the ratios of the tip diameters, i.e., $62.23/274.32 = .22685$, generally not considered too far apart. Accepting the differences due to Reynolds Number was agreed to be the best path to follow.

The ratio of air forces to inertial forces is called Lock Number defined by:

$$\text{Lock Number} = (\rho C_e a R^4 \Omega') / (I \bar{\Omega}')$$

where: ρ = air density
 C_e = mean chord of blade
 a = blade lift-curve slope
 R = blade radius
 Ω = angular velocity
 I = inertia of blade about propeller axis

This must remain constant for scaling similarity. For a given advance ratio, V/R , the air forces are proportional to $\rho \Omega^2 R^4$ and the inertial forces are proportional to $\sigma \Omega^2 R^4$. The Lock Number simply breaks down to density ratio equals a constant.

$$\rho/\sigma = \text{constant}$$

where: σ = mean structural density of propeller blade

This indicates that the aeroelastic model should be tested at the same air density if the structure is scaled from the SR-7L blade.

Similarity in structural stiffness is often evaluated through the use of the Cauchy Number. This number represents the ratio of the flatwise elastic force to the aerodynamic inertial force at each blade station.

$$\text{Cauchy Number} = EI/\rho V' R^4$$

where: E = Young's Modulus
 I = moment of inertia of blade cross section
 ρ = air density
 V = air velocity
 R = blade radius

Since inertia, I , is proportional to R^4 , the Cauchy Number is proportional to:

$$E/\rho V' = \text{constant}$$

For constant density and velocity, the effective Young's modulus has to be constant between configurations. For proper coupling between the modes, it is necessary to properly scale the edgewise stiffness and torsional stiffness distributions. Therefore, the ratio of edge wise and torsional stiffness

distributions to flatwise stiffness distributions has to remain the same. The stiffness parameters can also be simulated by matching the P-order frequency placement to those of the SR-7L blade. This assumes that the mode shapes and inertial distributions are the same. Keeping P-order placement constant requires that frequencies be kept inversely proportional to blade size.

Flutter boundaries are generally a function of reduced frequency and are generally evaluated at the 3/4 radius.

$$\text{Reduced Frequency} = b\omega/V$$

where: b = semi-chord length
 V = velocity
 ω = frequency

If the velocity, V , is constant, the semi-chord, b , is proportional to size and since ω is inversely proportional to size, the reduced frequency must be constant between configurations.

Gravitational forces are usually represented by the Froude Number which is defined as the ratio of centripetal force to gravitational acceleration.

$$\text{Froude Number} = R\Omega/\sqrt{g}$$

where: R = radius to blade cg
 Ω = angular velocity
 g = gravitational acceleration

It is felt that the ratio of inertial forces and airloads are much greater than the gravitational force such that the effect of gravity is negligible.

Lastly, the effect of damping on scaling has to be determined. Aerodynamic damping is a very important factor in dynamic response considerations, since it is a primary item in classical type flutter. Except for the effects of Reynolds Number discrepancies, this damping is a function of the airloads which vary as the radius squared. The unit loading per square cm is constant for constant Mach Number scaling or constant reduced frequency.

4.2 Retention Stiffness Scaling

The previous discussion on similarity is predicated on the assumption that the scaled model has similar mode shapes, P-order frequencies, and inertial distributions as the large blade. This might occur if the model structure were identical to the SR-7L structure in composition as well as geometry. Therefore, the first step was to review the SR-7L model characteristics and to investigate whether a scaled version with identical geometry and composition would demonstrate matching characteristics, analytically. This would establish a baseline. To do this, an FEA model of the preliminary design review (PDR) SR-7L blade was scaled down and analyzed.

A problem arose in scaling the retention stiffness of the SR-7L blade. One approach involved scaling the stiffness directly by the ratio of the blade loads. The blade bending moments are a function of the tip diameter to the third power. Therefore, the ratio of the bending springs, K_{ox} , K_{oy} , and K_{oz} (see Figure 4-1 for definition of coordinate system) of the model to those of the SR-7L is:

$$(62.23/274.32)^3 = .01167$$

Similarly, the thrust and axial spring rates are functions of the square of the tip diameter. In this case the spring constants, K_x , K_y , and K_z were scaled from the SR-7L by the ratio:

$$(62.23/274.32)^2 = .05146$$

A vibration analysis was performed on this scaled FEA blade model and it was found that the frequencies and mode shapes showed good correlation to the SR-7L blade (compare Figures 4-2 and 4-3). This tended to substantiate the retention stiffness scaling procedure.

At this point the use of a solid metal blade was investigated by changing all FEA material properties to the same material. This would have provided the simplest model blade construction. However, as anticipated, material composition and geometry were so different that no match was obtained.

Next, a means had to be found to simulate physically the reduced retention stiffness which was required analytically. Due to space limitations within the hub, and the fact that critical bearing tolerances do not scale directly, a ball bearing retention such as used on the SR-7L could not be used on the model. Since the bending spring rate of the ball bearing is much lower than the other retention spring rates, it has the greatest effect on the blade natural frequencies and mode shapes. Therefore, ways of simulating the bearing bending spring rate on the model were investigated. The approach selected was to rigidly clamp the model blade at the root and use a long, small-diameter shank to simulate bending of the retention bearing. No attempt was made to match thrust and shear spring rates. The diameter and length of the shank were calculated by applying the formula for the bending spring rate of a cantilevered rod with an applied bending moment (see Figure 4-4):

$$K = EI/L.$$

A titanium shank with a 1.588 cm. (.625 inch) diameter was substituted for the scaled-down aluminum shank on the FEA model. Titanium was selected because the shank diameter, necessary to simulate the retention stiffness desired, was suitable in this material for the small hub envelope. Also, from a stress standpoint, the reduced diameter shank required for stiffness dictated a higher strength material than aluminum, which is the material of the large blade.

Again, subsequent vibration analysis of the scale FEA model with a reduced-diameter, extended titanium shank, confirmed the validity of this approach of modeling bearing flexibility (compare Figure 4-5 to Figure 4-2).

4.3 Origin of New-construction Model Blade

At this point a scaled model has been developed which had a reasonable retention and correlated well, dynamically, with the SR-7L. It is convenient to refer to this model as the "exact scale model". However, it could only be considered a theoretical model because it violated practical construction methods. The spar was composed of titanium in the shank region and aluminum outboard of the shank. The shell thicknesses (which were scaled down from the SR-7L) were not adequate. Because the minimum thickness to which a spar could be machined was .5 mm (.020 inch), the spar would have to be truncated a considerable distance inboard of the blade tip.

In a previous discussion about scaling parameters, it was noted that similarities of mode shapes, P-order frequencies, and inertial distributions occurred if the model structure were identical to the SR-7L in construction and geometry. However, due to manufacturing limitations for the model which did not exist for the SR-7L, the stiffness and mass distributions had to be adjusted to provide similar P-order frequencies. This could be accomplished by matching the inertial, mass, and stiffness radial distributions to those of the exact scale model. Since an exact match of mass and stiffness was nearly impossible, it was decided to favor matching stiffness inboard (less than 50% of the blade span) while also trying to match the mass outboard (greater than 50% of the blade span) to that of the exact scale model. This is of importance to the primary modes in torsion, edgewise bending, and flatwise bending because of the way inertial energy is transferred to the structural displacements during each oscillation for these modes.

A "new-construction" model blade, based on current manufacturing techniques, reasonable shell thicknesses, and a titanium spar was developed. The section properties (major and minor moments of inertia and area) of the new model were made as similar as possible to those of the exact scale model at several radial locations along the span of the blade.

It became necessary to utilize a graphite/fiberglass composite shell in the region adjacent to the titanium spar, and in the region extending beyond the tip of the fore-shortened spar. Graphite provided stiffness in the flatwise sense and its low density offset the heavy titanium spar.

The Hamilton Standard computer program H349, a section properties program, was used to evaluate the match of stiffness and mass of the exact scale model. The procedure was to draw a plan view of the spar based on the exact scale model spar. An "educated guess" of the shell thicknesses was made using previously agreed upon ply thicknesses of .140 mm (.0055 inch) and .178 mm (.0070 inch) for the fiberglass and graphite, respectively. Section properties were then calculated using the H349 program. These properties were compared against those of the exact scale model at every station. Spar

widths and shell thicknesses were adjusted as necessary. A new smooth spar was drawn and analyzed using H349. These steps were repeated until section properties were as close as possible to those of the exact scale model.

4.4 Finite Element Modeling Iterations

The next step was to create a finite element model of the new-construction model blade. Previous experience with the SR-7L demonstrated that a three-layered configuration, i.e., center layer of spar and foam elements, and two offset layers of shell elements (face and camber), would be an acceptable model. Since a finite element model requires considerable effort to construct, a preprocessor was written to reduce the time required to construct anticipated trial models by generating the material, elemental, and nodal data necessary for the finite element analysis. This preprocessor also calculated the equivalent material properties of the fiberglass/graphite composite so that it could be modeled as a single offset layer.

At the time the first finite element representation of the aeroelastic model was created, the SR-7L was in the early phase of detail design. Final geometry had not yet been determined. Thus, the geometry of the finite element model had been scaled down from the SR-7L PDR static geometry. The results of the finite element vibration analysis of this model were encouraging. Frequencies and mode shapes were in good agreement with those of the SR-7L PDR blade (compare Figure 4-6 to Figure 4-2). The aeroelastic model was also slightly more stable than the PDR blade.

When information became available concerning the final design geometry of the SR-7L blade, a new finite element model was created. This model reflected the static (pre-deflected and pre-twisted) shape of the large blade. Steady-state loads were applied analytically and frequencies and stability were calculated in the deflected position. Because this new model reflected changes in only the external geometry of the previously successful model blade (i.e., no shank and spar geometry changes), the rather poor match of vibration analysis results was not expected (compare Figures 4-7 and 4-8). Since the frequencies were generally lower than those of the SR-7L blade, the shank diameter of the model was increased to 1.727 cm (.68 inch). Subsequent frequency analysis showed some improvement, but the surprising result was that the stability dropped significantly. Part of the drop was attributed to starting the model from the static geometry position. Tip deflections were greater than anticipated.

A closer look into the problem revealed that the graphite plies had inadvertently been modeled at a ± 75 degree orientation to the blade spanwise axis. The basis for previous work with the H349 section properties program had included graphite plies oriented at ± 15 degrees. A review of the frequencies and mode shapes up to that point indicated that it might be advantageous to orient the graphite plies at 0 degree and 30 degrees. This was an attempt to raise the torsional frequency (fourth mode) by aligning the graphite plies relative to the sweep angle (approx. 15 degrees) near the blade tip. Vibration analysis of this new finite element model revealed that the mode shapes

were quite similar, but the frequencies were somewhat higher than those of the SR-7L blade. The model was also slightly more stable than the SR-7L blade. The model was identified as 9C (corrected graphite plies).

Two other finite element models were constructed, varying the shank diameter and graphite ply orientation, and adding leading edge mass near the tip (to simulate a sheath). These models failed to yield any improvement in dynamic/stability correlation to the SR-7L blade. Therefore, the model discussed above, 9C, was selected as the final design. See Table 4-1 for a summary of the frequency and stability results of the various models analyzed.

5.0 FINAL BLADE CONCEPT

The final model blade, 9C, selected from the analytical iterations described in the previous section, satisfies the requirements outlined in Section 3 of this report. The external geometry is identically scaled from the SR-7L blade. Even the .254 mm. (.010 inch) thick erosion coating of the SR-7L blade has been simulated by the addition of an outer shell layer of fiberglass cloth, .051 mm. (.002 inch) thick. Figure 5-1 shows a comparison of the planforms of the final model blade and the scaled SR-7L blade.

The aeroelastic model blade is composed of three structural layers: a central spar-and-filler layer enveloped by two graphite-reinforced fiberglass shell outer layers (face and camber). Four plies of fiberglass cloth, each .140 mm. (.0055 inch) thick with fiber orientations of -25 degrees and +65 degrees to the blade axis, cover most of the blade. The shells are locally reinforced over the spar with three layers of graphite, each .178 mm. (.007 inch) thick, sandwiched between fiberglass plies, with alternating ply orientations at 0 degree and 30 degrees to the blade axis. See Figure 5-2 for typical shell cross sections.

The titanium spar is somewhat narrower and thinner than a scaled down SR-7L aluminum spar. Also, because of space limitations inside the shell cavity, the spar is truncated inboard of the tip, at the 25.07 cm. (9.87 inch) station. Two graphite reinforcing plies extend beyond the tip of the spar to provide stiffness continuity, simulating that of the SR-7L full-length spar. Outboard of the 22.86 cm. (9 inch) station, center layer cavities contain solid fiberglass fill. The solid fiberglass fill helps compensate for the lack of spar mass at the tip. Low density foam, .128 gms/cm³ (8 lbs per cu. ft.), fills the cavities fore and aft of the spar inboard of the 22.86 cm. (9 inch) station. The shank diameter, 1.727 cm. (.68 inch), is considerably reduced for reasons previously explained (Section 4). Figure 5-3 is a planform of the final blade concept with the spar, fill cavities, and graphite plies indicated.

6.0 STRUCTURAL EVALUATION

6.1 Methodology

6.1.1 FEA Modeling

The aeroelastic model blade was analyzed using a finite element program developed at Hamilton Standard called BESTRAN. BESTRAN has been used for several years in the design of blades, during which time several pre- and post-processors have been developed to simplify and improve the design tasks. Particularly beneficial is the ability of the BESTRAN program to readily obtain informative plots, such as stress, strain, and deflection contours, as well as model plots (with node and element numbers) and thickness contour plots.

Previous experience in the analysis of blades with spar/foam/shell configurations has shown that a three-layered finite element model with triangular elements yields quite satisfactory results. The three-nodes triangular elements are similar to those used in NASTRAN finite element analysis in that both exhibit constant stress and strain across the element, and both have a linear variation of thickness from node to node (grid points). Figure 6-1 shows a typical blade cross section which consists of a center layer of spar and foam elements to which offset layers of shell elements are rigidly linked.

The procedure used for the formation of a finite element model follows. A full-size planform of the aeroelastic model, showing the airfoil and spar leading and trailing edge outlines, was drawn by scaling down the SR-7L by the ratio of tip diameters. Several parallel lines (blade station lines) were drawn connecting the leading and trailing edges of the airfoil. A network of grid points (nodes) and triangles (elements) was created between adjacent station lines. A fine break-up of triangles (small triangles) was desired at structurally crucial areas such as in the shank and at the transition zone between the shank and the airfoil. Prior finite element analyses of blades had demonstrated that a coarser break-up of triangles would be acceptable fore and aft of the spar where stresses are usually lower. To obtain more accurate results, equilateral triangles, generally thought to be ideal, were drawn wherever possible especially in the above-mentioned critical areas of the blade. In areas of the blade where equilateral triangles could not be easily or practically achieved, the aspect ratios (i.e., ratio of the longest side to the shortest side) of the triangles were kept below two. In addition, no angle within a triangle exceeded 90 degrees wherever possible. The station lines and triangles were redrawn until the desired break-up and triangular shapes were obtained.

Next, an input data deck to the BESTRAN processor had to be created. Part of the required data were the node table, which defined the thickness and global coordinates of the nodes; the element table, which connected the nodes to form elements; the configuration table, which connected the offset layer to the center layer; and the material table, which defined the material properties and stress angles of the elements. The bookkeeping tasks were enormous. It was for this reason, and also because it was suspected that several

model revisions would be made, that a preprocessor was written to create nodal, elemental, and material data. The preprocessor, also called on a sub-routine, was derived from a Hamilton Standard laminates program (H250), to calculate the material properties of the various shell laminates. This allowed the composite shell layer (fiberglass and graphite) to be modeled as single offset layers, saving considerable computation time.

The inputs required for the preprocessor were the node and spar leading and trailing edge locations along the station line, and the definition of the shell (material, thickness, and ply orientation, and ply drop locations as percent of chord). Material properties for each element were derived by averaging the material properties at the three nodes which comprised the element. Because several elements had the same materials, a check was written into the preprocessor to eliminate duplicate material inputs.

Figure 6-2 is a flow chart of the steps used in generating a finite element data deck. The final FEA model contained 562 nodes (center layer only), 2165 elements (three layers), and 193 materials.

6.1.2 Retention Simulation

Once a satisfactory FEA model was created, it was necessary to determine what the boundary conditions were. Because a ball bearing retention could not be used as a means of retaining the blade within the hub, the blade shank was rigidly clamped to the hub. The reasons for this were discussed at length in Section 4.2 of this report. Figure 6-3 shows the shank of the blade clamped to the hub. The dashed line in the figure represents the FEA model blade shank. A constant diameter shank was used for ease of modeling. The location of the model shank inboard surface was determined by drawing a 45 degree line from the center of the radius, R , to the contact surface between the blade shank and the hub, as shown in the figure. The fact that the FEA model blade diameter, at the contact point, was slightly less than that of the actual model blade, compensated for the fact that the contact angle was probably higher than 45 degrees (dictating a longer shank) under load. In other words, the bending stiffness of the FEA model shank is probably the same as that of the actual blade which has a slightly longer and larger diameter shank in the vicinity of the contact zone.

To simulate a clamped retention, the nodes at the inboard end of the shank were restrained in all six degrees of freedom (three translational and three rotational). See Figure 6-4.

6.1.3 Loads Application

The aeroelastic model blade will be subjected to centrifugal loads and air loads (thrust and torque) during testing. The BESTRAN processor automatically imposes centrifugal loads on a rotating blade when the rotational speed of the blade is included in the BESTRAN data deck. In order to account for centrifugal stiffness, BESTRAN was executed twice. The first execution creates a centrifugal stiffening matrix. In the second execution, the centrifugal stiffness matrix is used, in addition to the structural stiffness matrix, to

analyze the blade. Experience with other blades has shown that for the relative amounts of deformation (deflection and twist) predicted with this blade, this type of analysis provides results that are within 5% of alternate, costlier, non-linear, converged solutions.

Airloads had previously been applied to the FEA models at only one node per blade station. Usually the node selected was close to the aerodynamic center of pressure along the chord. Because Prop-Fan blades are generally very thin blades, it was felt that local distortions might be considerable if the air loads were applied as concentrated loads. Therefore, a program to simulate the distributed air loads by loading all the nodes along the chord was created. The program resolved power (in-plane) and thrust (out-of-plane) forces on each section into lift and drag loads at all nodes of the section and distributed the lift forces in such a way as to preserve the center-of-pressure specified at the section. The discrete loads at each node were then finally resolved into global coordinates consistent with the axial conventions of the blade FEA model.

6.1.4 Steady State Analysis

Stress analyses of the aeroelastic model blade under all flight conditions of the SR-7L blade were unwarranted. The model blade will be tested at cruise conditions, 10,668 meters (35,000 ft.) altitude on the Jetstar aircraft and at several angle settings, including cruise, in the wind tunnel. The cyclic loads will be small compared with those encountered during a takeoff/climb condition. It was assumed that the model blade will be wind-milling at a cruise blade angle when the Jetstar is climbing. However, the takeoff/climb condition was investigated because NASA had requested it to provide more data for stability evaluation.

Only steady state stress analyses were performed for the Jetstar wind tunnel and takeoff/climb conditions. The maximum allowable cyclic stress could be readily determined by plotting the maximum steady stress on a Goodman Diagram. It is important that strain gauges be installed at several locations on the blade, especially in the shank, to monitor the cyclic stresses.

As noted earlier, the blade will be subjected to centrifugal and air loads. The centrifugal loads cause axial (membrane) stresses in the blade, and can also cause bending stresses if the blade has built-in offset and/or sweep. The air loads primarily cause bending stresses. Thin blades such as Prop-Fan blades can develop high flatwise bending stresses. Previous experience in blade design has shown that with the correct selection of offset, centrifugally induced bending moments can be used to counteract the aerodynamically induced bending moments, and thus reduce bending stresses for a selected operating condition. The SR-7L blade utilizes offset optimization to reduce stress in the blade inboard region; however, the same could not be done in the tip region without risking aeroelastic instability. Therefore, the tip offset in the large blade was a compromise between stress and stability. The offset of the aeroelastic model matches that of the large blade because it was scaled down exactly from the SR-7L static geometry, determined through several predeflection iterations.

There was some concern as to whether or not the model would deflect to the same relative position under load as the SR-7L. The deflection of the model blade will give an indication as to how well the stiffness and mass distributions of the model blade (titanium/graphite/fiberglass construction) are matched to those of the SR-7L blade (aluminum/fiberglass construction).

In order to determine the stresses and deflections of the aeroelastic blade, BESTRAN was executed. As stated before, BESTRAN was run twice in order to incorporate the centrifugal stiffening effects of the rotating blade. The BESTRAN postprocessor was used to obtain stress and deflection plots. Because the shell is a composite laminate of fiberglass and graphite in an epoxy matrix, the stresses calculated are average stresses through the thickness of the laminate. To review the results, it was decided to plot strain contours for the shell such that stresses in each layer could be evaluated by multiplying the strain by the modulus of the layer in question. BESTRAN was run for those operating conditions noted in Section 3 of this report.

6.1.5 Resonant Frequencies and Mode Shapes

It has been stated that in order to simulate the aeroelastic characteristics of the SR-7L blade, the corresponding frequencies and mode shapes would have to be very similar. Because of the difficulty in matching the stiffness and mass exactly to the SR-7L blade, several fine adjustments to the blade construction were anticipated. A vibration analysis was required for each revision. An efficient means of calculating those frequencies and mode shapes involved converting the BESTRAN data deck to an equivalent NASTRAN input deck, and entering the re-formatted BESTRAN mass and stiffness matrices (structural and centrifugal) directly into the NASTRAN solver. Frequencies from test cases analyzed in this manner have been found to correlate extremely well with the BESTRAN-calculated frequencies and are achievable at a fraction of the time and cost. A postprocessor was utilized to read the NASTRAN modal output and create mode shape plots.

Plotting the SR-7L blade and aeroelastic model blade frequencies on a "modified" Campbell Diagram proved to be an effective way to compare frequencies at a glance. Normally, a Campbell Diagram is a plot of "Frequency" (vertical axis) versus "propeller RPM" (horizontal axis). In this case, however, it was difficult to compare frequencies because the model and SR-7L blades did not operate at the same rotational speeds. The ratio of the rotational speeds of the aeroelastic model blade to the SR-7L blade is inversely proportional to the ratio of the diameters, as shown in the following equation:

$$W_m/W_l = D_l/D_m$$

where: W_m - rotational speed of aeroelastic model
 W_l - rotational speed of SR-7L
 D_m - tip diameter of aeroelastic model
 D_l - tip diameter of SR-7L

Therefore, to negate the diameter effects, the Campbell Diagram was modified by plotting "frequency times tip radius" versus "propeller RPM times tip radius" versus "propeller RPM times tip radius". Figure 6-5 shows a comparison of a Campbell Diagram and a modified Campbell Diagram for a typical design iteration. This type of modified diagram is used to compare results of the final blade in Section 6.2.4.

6.1.6 Stability

The final step in the verification of aeroelastic similarity between the .67 meter (24.5 in.) diameter SR-7A aeroelastic model and the 2.74 meter (9 ft.) diameter SR-7L is a comparison of the stability predictions using a common aeroelastic stability analysis. Verification of the model was determined by comparing its stability to the SR-7L blade at the design cruise condition: Mach .8 flight speed, 10,668 meters (35,000 ft.) altitude, and 243.8 m/sec (800 ft/sec) tip speed. Stability checks at this condition were performed on a number of model configurations because the construction of a .62 meter (24.5 in.) diameter model differs substantially from that of the full size Prop-Fan. However, results of only the final selected aeroelastic model configuration will be reviewed in this report. Additional stability checks at other conditions were performed on the selected design to lend guidance to future testing of the model on the Jetstar aircraft and the 2.44 meter (8 ft.) by 1.83 meter (6 ft.) NASA Lewis wind tunnel. The conditions for these check cases correspond to a takeoff/climb condition and a design cruise performance simulation in the wind tunnel.

To make the aeroelastic stability comparison, the same aeroelastic analysis used in conjunction with the SR-7L was utilized. This program is a modal analysis, developed in-house, that uses mode shapes from finite element analysis predictions and couples unsteady aerodynamic loads to the mode shapes to determine blade stability. A modified version of the stability analysis was used for the wind tunnel operating condition. The modifications include the addition of three-dimensional blade tip effects in terms of a tip loss factor, and empirical airfoil data.

6.2 Analytical Results

6.2.1 Deflections

A statement was made earlier in this report that the deflections under load can indicate how similar the model blade mass and stiffness distributions are to those of the SR-7L blade. Plots containing contours of the deflections resolved normal to the chord at the 75% blade radial station (referred to hereafter as the 3/4 chord) were generated by selecting the applicable BESTRAN post-processing option. When plotted on a view of the blade taken normal to the 3/4 chord, the contours reflect deflection into and out of the plane of the paper. A convenient way to compare deflections was to multiply the SR-7L blade deflections by the ratio of the diameters of the model blade to the SR-7L blade (i.e., $62.23/274.32 = .22685$). These would theoretically be the deflections of an exact-scale model.

The locations and magnitudes of maximum positive (out of the paper) and maximum negative (into the paper) deflections were compared on both blades, as shown in Figure 6-6. These are the calculated deflections for the 10,668 meters (35,000 ft.) cruise condition. The maximum negative deflection occurs at the trailing edge of the tip station for both blades. The 2.29 mm (.09 inch) deflection of the model blade compares very well with the scaled-down deflection, 2.79 mm (.11 inch) of the SR-7L blade.

The maximum positive deflections occurred at the leading edge of the blade at approximately the 85% blade radial station. Again, the deflections compare very well - 3.05 mm (.12 inch) for the scaled-down SR-7L versus 3.30 mm (.13 inch) for the aeroelastic model. Deflection contours and node lines of the respective blades were also quite similar.

The aeroelastic model blade will be tested in the NASA/Lewis 2.44 meter (8 ft.) by 1.83 meter (6 ft.) wind tunnel as well. Wind tunnel pressures equivalent to a 2292 meter (7520 ft.) altitude and rotational speeds of 8622 rpm will cause the blade to experience higher air and centrifugal loads. Because of this, the model blade will deflect more in the wind tunnel than at 10,668 meters (35,000 ft.). This is clearly illustrated in the deflection plot shown in Figure 6-7. The maximum negative deflection, again at the trailing edge tip station, is 5.33 mm (.21 inch), more than twice the deflection at a 10,668 meter (35,000 ft.) altitude. The maximum positive deflection is 2.79 mm (.11 inch), very similar to that for the 10,668 meter (35,000 ft.) altitude case. These facts, and the location of the deflection contours (node line in particular) indicate that most of the difference in deflection occurs in the outer 10% of the blade span.

Another way to compare deflections is shown in Figure 6-8. The translation and rotation of the tip are shown. It is felt that if both the displacement and twist of the model blade are similar to those of the SR-7L blade, the stabilities should compare well. The deflection and twist comparisons between both blades are summarized in Figure 6-8. As can be seen from the table in that figure, the twist and total deflection agree quite well at the 10,668 meter (35,000 ft.) design cruise case. The twist change in the wind tunnel is also quite close to the large blade, and should permit valid testing of aerodynamic performance. The fact that the wind tunnel deflection is larger, however, will result in a decrease in aeroelastic stability. This was deemed acceptable and will be discussed in greater detail in the stability section, 6.2.6.

6.2.1 Shank Loads

As with any test model program, strain gauges will be mounted at several locations on the blade. Since this is an aeroelastic model, gauges should be positioned so that edgewise, flatwise, and torsional mode shapes can be differentiated. It is also important, though, to locate strain gauges at predetermined locations of maximum stresses so that they can be carefully monitored. As will be described in the next section about stress/strength comparisons, the highest spar stresses are found in the shank. In order to monitor these stresses, the direction of the applied moments should be known.

Shear loads, moments, and their directions are provided in Table 6-1 for several load conditions. These loads and moments are taken at the blade retention. Sign conventions for blade loads and moments are given in Figure 6-9.

Because the blade loads and moments listed in Table 6-1 were determined at the blade retention, these will be the same loads which will be applied to the hub. The bending moment will be used to determine the contact stresses at the shank/hub interface and the hub lip stresses. Note that one of the conditions given in Table 6-1 is a takeoff/climb condition with no air loads. This is a hypothetical condition of running the model blades in a vacuum at high rpm. At this condition, the blades would apply a high bending moment to the hub. The conservative approach was taken that if the hub was designed to withstand this high bending moment, it should endure any of the operating conditions encountered.

The blade twisting moments will be needed to design pitch change components such as the gears and pitch locking pins. Twisting moments will be discussed later in Section 8.2.

6.2.3 Stress/Strength Comparison

Simulating the aeroelastic characteristics of the SR-7L blade with a 62.23 cm (24.5 inch) diameter model was a lengthy task. Several iterations of attempting to match stiffness and mass distributions, and running frequency and stability analyses were required until a satisfactory aeroelastic model has been designed. Each time the construction of the blade varied, the stress magnitudes and distributions changed. Attempting to simultaneously satisfy vibration, stability, and stress requirements for each iteration was thought to be too time consuming. Therefore, the decision was made that the iterations would entail frequency and flutter analyses only. Once a model exhibiting the desired aeroelastic behavior had been designed, the stresses would be checked.

This is not to say that no consideration was given to stresses during the early design stages. When the shank diameter was reduced to simulate a bearing type retention, as described in Section 4.2 of this report, titanium was selected as a spar material to accommodate the higher stresses anticipated. Also, stress checks were made on the first model blade iteration to see if there were any areas in which stresses approached or exceeded allowable limits. Because none was found, it was assumed that small changes in blade construction would not increase the stresses enough to cause problems. The stress results of the final blade concept proved this assumption to be valid.

Just as with deflections, blade stresses are most easily determined by reviewing contour plots. The BESTRAN postprocessing options for generating stress plots are numerous, including radial (spanwise), chordwise, principal, and effective stress plots. Usually, effective stresses are plotted for blade spars made with isotropic materials such as aluminum or titanium. Effective stresses, based on the von Mises failure criterion, can be compared directly with tensile allowables. Although effective stresses are generally

acknowledged to be conservative, the radial spar stresses of the aeroelastic model were found to be higher than the effective stresses. Therefore, radial stress contour plots were generated for the spar for comparison to tensile allowables.

Figures 6-10, 6-11, and 6-12 are stress contour plots for the following conditions: 10,668 meter (35,000 ft.) cruise, wind tunnel (8622 rpm), and takeoff/climb, respectively. In all cases, the stresses are higher on the camber (suction) side of the spar, indicating that for the model blade construction, centrifugally induced bending stresses tend to overcome the air-load bending stresses. The maximum stresses in the shank and farther outboard in the airfoil region are indicated for each condition. Maximum shank stresses were consistently located at the leading edge. This is explained by the fact that since the center of gravity of the blade is toward the leading edge, the centrifugal bending effects cause high tensile stresses along the leading edge. These add to the centrifugal membrane stresses. The same logic can be used to explain why the maximum stresses in the airfoil region of the spar were found at the trailing edge near the spar mid-span. In this case, the center of gravity of the blade outboard of the spar mid-span was located toward the trailing edge of the airfoil.

Since the spar "necked-down" (going inboard) to a rather small diameter, there was a sizeable stress concentration in the shank. The fatigue strength of the shank is consequently increased by glass bead peening, which leaves the surface in a state of residual compressive stress.

Maximum shank and airfoil stresses are compared with allowable stresses on the Goodman Diagrams of Figures 6-13 and 6-14 respectively. The acceptable cyclic stresses are also indicated. It is important to note here that the cyclic stress limits shown are associated with the peak steady stresses. Because the section modulus in the shank is constant and the cyclic moment will probably increase going inboard, the stresses will be higher at the retention than at the point of maximum steady stress. Strain gauges should be mounted far enough outboard on the blade shank to avoid interference with the hub, and, therefore, will not be located at the point of highest cyclic stress. Care must be taken not to exceed predetermined allowable stresses in the retention.

For reasons noted in Section 6.1.4, radial strain plots were generated for the shell layers. The strains were converted to stresses for the graphite and fiberglass plies which comprised the shell. Figures 6-15 through 6-17 indicate the locations and magnitudes of peak graphite and fiberglass stresses, for the test conditions mentioned. Maximum graphite stresses occurred at the trailing edge of the spar on the camber side, in every case. The peak fiberglass stresses were found on the face side beyond the spar tip. Graphite and fiberglass stresses are compared against allowables on the Goodman Diagrams shown in Figures 6-18 and 6-19 respectively. Again, the cyclic stress margins are indicated.

The effective stresses of the foam were observed to be considerably higher than the radial stresses. This was in contrast to spar stress results. Effective stress contour plots, Figures 6-20 through 6-22, are provided for the 10,668 meter (35,000 ft. cruise), wind tunnel (8622 rpm), and takeoff/climb conditions. As the figures indicate, the peak stresses are located forward of the spar near the shank. Although stresses were generally higher on the face side of the foam, camber side stresses, equivalent to the maximum stresses, were found for the wind tunnel and takeoff/climb conditions. The Goodman Diagram illustrated in Figure 6-23 shows the foam stress/strength relationship for each operating condition. Allowable cyclic stresses are shown in the same figure.

6.2.4 Frequencies and Mode Shapes

The final model blade concept was the result of several compromises. Various design iterations of the model have shown that frequencies, mode shapes, and stability could not be simultaneously matched, within practical constraints of schedule, to those of the SR-7L blade. It is appropriate here to define the term "match" when applied to frequencies and mode shapes. Early in this program, guidelines for a match were established, requiring that the first five frequencies be within 10% of the SR-7L blade, and that corresponding mode shapes look similar. The five mode shapes include flatwise and edge wise bending as well as the erosion mode, and as such, provide a good indication of the mass and stiffness similarities between the model and the SR-7L blade.

Figure 6-24 is a modified Campbell Diagram (defined in Section 6.1.5) which shows a direct comparison of the model and SR-7L blade frequencies for the 10,668 meter (35,000 ft.) altitude condition. With the exception of the fourth mode, which is generally accepted to be a torsional mode, the model blade frequencies are higher than those of the SR-7L blade. However, all five frequencies do satisfy the 10% guideline described above. As the diagram also indicates, the frequencies (except the fifth mode) of the model tend to fall closer to P-order lines. In particular, the second mode crosses the 3P line at the operating rpm. An attempt was made to lower the model blade frequencies by reducing the shank diameter. Unfortunately, the stability dropped significantly. It was decided to accept the more stable concept since the frequencies were within the 10% allowed. Also, it is anticipated that 3P excitations will be low in magnitude. The frequency comparisons are summarized in Table 6-2. Figure 6-25 is a conventional Campbell Diagram which shows the frequency placement of the aeroelastic model blade with respect to the P-order lines.

The model blade frequencies for the wind tunnel operating environment are also plotted in Figure 6-25, as well as in Figure 6-24. As can be seen, the P-order placement of the first three modes, in the wind tunnel, is quite similar to that of the large blade. Although it is not required that the frequencies of the model match those of the SR-7L for this condition, they are provided to help predict the behavior of the model in the wind tunnel.

Mode shape plots, shown in Figures 6-26 through 6-30, are similar to the deflection contour plots described in Section 6.2.1. Normalized deflections, resolved perpendicular to the 3/4 chord, are plotted. Contour lines which are in a chordwise, or nearly chordwise, direction indicate that the blade is bending in a flatwise sense. Torsional modes are recognized by the spanwise, or nearly spanwise, direction of the contours. Edgewise modes are difficult to recognize on such plots. Since blades are very stiff about their major axis of bending, edgewise modes are generally determined by checking the directions of shank bending moments.

The first mode of the model blade is compared to that of the SR-7L blade in Figure 6-26. The mode shapes are very similar. It is apparent from this figure that mode 1 is the first flatwise bending mode. Mode 2, as shown in Figure 6-27, also shows a close agreement between blades. Although not obvious from the figure, the second mode is the first edge wise bending mode. This was verified by checking the direction of the shank angular displacements. It is interesting to note the amount of flatwise bending in the tip region of the blade associated with this mode. This indicates that there is considerable coupling of the edgewise and flatwise modes.

The similarities in the third mode, Figure 6-28, are less favorable, although still quite acceptable. A tip-to-hub view of the mid chord deflections along the blade span was drawn to determine that this was the second flatwise bending mode.

Figure 6-29 shows that the fourth mode is the first torsional mode. The comparison between blades is quite good in spite of the fact that the node line of the model sweeps back at a shallower angle toward the trailing edge of the blade.

The contours and node lines of the fifth mode agree well, as shown in Figure 6-30. It is apparent from the number of node lines and the directions of deflection contours that this is the third flatwise bending mode; also, the angularity of the contours indicates some amount of torsional coupling is occurring.

As found with adjustments to frequencies, any attempt to improve mode shape correlation to the SR-7L blade resulted in lower stability or poor frequency match. In general, though, the mode shapes of the final model blade concept were similar to those of the SR-7L blade.

The first five mode shapes for the wind tunnel operating condition are shown in Figure 6-31. The mode shape patterns are essentially the same for the respective modes as those discussed above for the 10,668 meter (35,000 ft.) cruise condition.

6.2.5 Stability

Using the aeroelastic stability analysis described in Section 6.1.6, model blade stability was evaluated. Results of the stability predictions are shown in Figure 6-32 in terms of damping ratio versus Mach Number for the

model Prop-Fan at the design cruise operating condition. The model Prop-Fan undergoes instability at Mach .95 in mode 3 with an interblade phase angle of 315 degrees, just as occurred for the SR-7L stability predictions. Figure 6-33 clarifies the damping similarities and differences between the SR-7L and the SR-7A blades. In addition to the zero damping value of mode three, the damping magnitude, mode order, and trends are similar for both blades. This similarity in damping predictions illustrates the aeroelastic similarity between the SR-7A and the SR-7L.

Two additional stability predictions were performed on the SR-7A for the purpose of lending guidance to future testing. The first case corresponds to the takeoff/climb condition of Mach .2 flight speed, sea level, and 243.8 m/sec (800 ft/sec) tip speed. Figure 6-34 shows the model damping predictions for this operating condition. Instability is predicted to occur in mode 3 at Mach .56. This flutter Mach number prediction shows the limit flight speed of the Jetstar test at sea level. The predicted stability for the SR-7L under the same operating conditions showed a mode 3 instability at Mach .6. The difference in the blades is due to the effect of blade retention. The SR-7L has a bearing retention with distinct in-plane and out-of-plane stiffnesses that do not change with blade angle setting. As noted previously, a bearing retention could not be included in the design of the model; therefore, the bearing stiffness was approximated by a small diameter blade shank. The blade shank design was optimized to simulate the design cruise condition. The blade angle difference at takeoff/climb alters the retention stiffness so that the simulation is no longer optimum. This affects the stability similarity between the two blades. The important aspect of the calculation is that the stability results for the model and full size Prop-Fans do not show any gross differences that would deteriorate aeroelastic stability at off-design conditions.

The second additional stability case corresponds to a design cruise performance simulation in the NASA Lewis wind tunnel. The operating conditions for this simulation are Mach .8 tunnel speed, which corresponds to an altitude of 2292 meters (7520 ft.), and a tip speed of 277.9 m/sec (911.7 ft/sec). The combination of high tip speed and low altitude results in low blade stability, as shown by Figure 6-35, the blade damping ratio plot. Figure 6-35 shows an instability in mode 3 at Mach .43, which is well below the desired Mach .8 tunnel speed.

A further examination of the stability was made using the modified version of the stability analysis which includes tip loss effects and empirical airfoil data. These modifications resulted in better agreement between predicted and measured stability on previous Prop-Fan models. The results using the modified analytical procedure, Figure 6-36, show the SR-7A to be marginally stable up to the desired Mach .8 wind tunnel speed.

7.0 HUB AND SPINNER

It was established in Section 3 of this report that the external hub and spinner contour of the aeroelastic model would be scaled down from the 2.74 meter (9 ft.) diameter SR-7L spinner by the ratio $62.23/274.32 = .22685$. It was accepted that the Reynold's number for the model and the SR-7L would differ directly by the ratio of tip diameters. This approach was judged to be the best option available without major changes in the model test environment. Reynold's number and its effects were addressed in Section 4.

The SR-7L blade shank is retained in the hub by a ring of ball bearings set in a hardened steel race on the shank and an integrally hardened steel race on the hub. As discussed in Section 4.2, the aeroelastic model hub will not be able to utilize this approach because of space limitations, and the complexity and cost of scaling all the hub and retention hardware down to such a small size. The alternative approach selected was to provide an extended small diameter shank to simulate the scaled flexibility of the SR-7L hub and retention bearing.

For conservatism the spinner/hub assembly was designed to support the maximum blade loading condition as listed in Table 6-1 in Section 6.2.1. The operating condition that generated the highest loads on the spinner/hub assembly is the vacuum condition at 8886 rpm, with a blade angle setting which matches the takeoff/climb condition. At this operating condition one blade generates 24,402 newtons (5486 lbs.) of centrifugal force and 102.8 n-m (910 in-lbs.) of steady bending moment.

7.1 Blade Retention Design

A schematic drawing of the hub/spinner retention design is shown in Figure 7-1. From Figure 7-1 it can be seen that the hub/spinner assembly consists of three structural members. These components are the spinner, forward hub half, and rear hub half. The spinner which is the forward most part is made of aluminum. The primary function of the spinner is to establish a smooth flow path for the air stream prior to impingement on the blades.

The spinner is fastened to the forward half of the hub by a left-handed screw thread. A left-handed thread is used because the inertial most of the spinner tends to generate a tightening torque when the hub is accelerated. To guard against potential loosening of the spinner during deceleration, three nylon inserts are installed 120 degrees apart in the spinner threads.

The remaining aerodynamic contour in the vicinity of the blades is formed by the external surfaces of the front and rear halves of the hub. The split hub concept facilitates installation and removal of the blades in the hub cavities. Both hub halves are made of steel.

The front and rear halves of the hub assembly are aligned by three pins. The pins are located such that there is only one position at which the two hub halves can be assembled. The pins are sized to be non-load carrying members.

To hold the front and rear hub halves together, eight alignment bolts were used. The bolts are serialized to assure that they are always assembled in the same hole. Dynamic balance of the spinner/hub assembly is accomplished by removal of material (by drilling) on the back face of the rear hub half.

7.2 Blade Retention Loads and Stresses

Blade loads to be reacted by the blade retention are graphically illustrated in Figure 7-2. A study of the magnitude of these loads reveals that the combined effect of centrifugal force (CF) and steady bending moment (SBM) yields the highest radial force.

Bending moments generated by the aeroelastic model blades can be resolved into equivalent radial and normal components, parallel and perpendicular to the shank axis, respectively. The maximum radial component can be combined with the centrifugal load as follows:

$$\text{Maximum Radial Force} = (4 \times \text{SBM/PD} + \text{CF})\text{Pd}$$

Where: SBM - Steady bending moment (in-lb)
 CF - Centrifugal force (lb)
 Pd - Pitch diameter of blade shank contact circle

Because of its magnitude, this radial force becomes the governing load, and the blade retention is designed to support this load for safe continuous operation.

In analyzing the hub retention area, contributions from the vibratory bending moment (VBM) were omitted because (1) design stresses in components affected by the bending moments are low compared to the allowables, (2) VBM is small compared to SBM, and (3) the direction of VBM is different from that of the SBM.

The blade contacts the hub circumferentially along a fillet radius at the in-board end of the shank. A matching convex radius in the hub is slightly smaller and dimensionally adjusted such that contact occurs at a nominal static angle of 45 degrees, measured from the plane of the fillet radius.

A circular line load at the pitch diameter of the contact circle was then calculated based on the maximum radial force. Using a Hamilton Standard developed contact stress program, contact stresses of the blade shank and the hub retention were then generated. Geometric dimensions and loading patterns at the blade shank and hub retention interface area are illustrated in Figure 7-3. The resulting maximum contact stress was found to be 31,576 newtons/cm² (45,800 psi). Low cycle fatigue stresses were then computed based on start-stop cycles. Goodman design allowables for the blade shank are provided in Figures 7-4. As can be seen, the stresses are very low, only about 25% of the allowable. Goodman design allowables for the hub retention, which is made of steel, were not shown because steel has a such higher contact stress allowable than titanium. Thus the safety margin for the steel hub retention is even higher than that for the titanium blade shank.

7.3 Hub Lip Stresses

In the schematic drawing of the hub/spinner assembly in Figure 7-1, the hub lip is shown on the forward half of the hub as the thinnest section in the hub. To analyze the forward hub and the hub lip, a Hamilton Standard two-dimensional body of revolution program was used. A shell of revolution model of the forward hub is shown in Figure 7-5. In Figure 7-6 the undeflected model is outlined by dotted lines and an exaggeration of the deflected position is shown in solid lines.

The model was loaded with uniformly distributed axial and radial forces. The total axial and radial forces applied to the two-dimensional forward hub stress model were developed by averaging contributions from all eight (8) blades. For the vacuum operating condition analyzed, each blade generates 24,402 newtons (5486 lbs.) of radial force and 102.8 n-m (910 in-lbs.) of steady bending moment. However, only one-half the total (sum of all eight blades) centrifugal force is reacted on the forward half of the hub; the other half is reacted by the rear half of the hub. Resolving the steady bending moments to obtain radial forces and then combining these with centrifugal load results in a radial force of 258,900 newtons (58,208 lbs.) or 40,400 newtons/cm (23,074 lbs/in) acting on the circumference of the hub/shank contact circle. Because the contact point is 45 degrees, an axial force identical in magnitude to the radial force was generated and applied to the 2-D shell of revolution model of the forward hub.

It must be explained at this point that the axial forces which tend to separate both halves of the hub are reacted either by the eight (8) close fitting bolts located between adjacent blade shanks, or by the large central bolt or mounting shaft which loads against cone seats located at the ends of each hub half along the rotation axis, or most likely, by both clamping systems. However, for analysis of lip stresses in the forward half hub it was assumed for conservatism that the eight (8) bolts do not carry any separation load. The separation load is actually the axial component of the contact force (force P_n in Figure 7-3) acting on the hub retention. Admittedly, the omission of the eight (8) bolts from the hub lip stress analysis introduces extreme conservatism in the design, but this was the established practice for six prior model hub designs, and conceivably could represent a case where one or more bolts is loose, broken, or simply omitted during assembly.

Stresses on two planes in the hub lip area are of primary interest. These two planes are labeled planes A-A and B-B in Figure 7-5. The 2-D shell of revolution analysis shows that radial and hoop stresses are about equal, and both are much higher than axial stresses. However, for low-cycle fatigue, a K_f factor must be applied to the cyclic portion of the radial stress. Thus the radial stress listed becomes the governing stress for low-cycle fatigue structural evaluation. Final results of the analysis are tabulated on the following page.

	<u>Plane A-A</u>	<u>Plane B-B</u>
Axial stress, n/cm ² (psi)	1502 (2179)	-1058 (-1535)
Hoop stress, n/cm ² (psi)	5488 (7960)	4477 (6493)
Radial stress, n/cm ² (psi)	4441 (6442)	4373 (6343)
Kf (ND)	1.60	1.20
Low cycle fatigue based on radial stress, n/cm ² (psi)	2221+3553 (3221+5154)	2188+4812 (3173+3806)

Low cycle fatigue radial stresses for both planes A-A and B-B are plotted in Figure 7-7; both cases showed large design margins.

7.4 Bolt Stresses

As mentioned above, eight 9.525 mm (0.375 in.) diameter bolts are used to clamp the forward and rear halves of the hub assemblies together. These bolts are needed to support the separation force developed by the centrifugal load and the steady bending moment (SBM). Because the contact angle between the blade shank fillet radius and hub retention is set at 45 degrees, loads applied radially are capable of generating appreciable hub separation forces.

Resolution of the centrifugal force load is illustrated in the left half of Figure 7-8. The shank steady bending moment is also capable of generating hub separation forces when resolved into its parallel and perpendicular components, as illustrated in the right half of Figure 7-8.

Based on the maximum shank loads from the vacuum condition, discussed in the previous section, the centrifugal force of 24,400 newtons (5486 lbs) generates 7766 newtons (1746 lbs) per bolt of separation force. Similarly, the SBM of 102.8 n-m (910 in-lbs) produces 4088 newtons (919 lbs) of hub separation force. The sum of these two separation forces is 11,854 newtons (2665 lbs) per bolt.

Bolt stresses are summarized in Figure 7-9. Note that the bolts have a design margin of safety of 249%. The calculated preload torque required is 16.6 n-m (147 in-lbs.) minimum, but to provide margin for cyclic moments and potential overspeeds, a preload torque of 28.2 - 39.5 n-m (250 - 350 in-lbs) is called for in the actual hardware.

8.0 PITCH CHANGE MECHANISM

The pitch change mechanism for the aeroelastic model is illustrated in Figure 8-1. The system is designed for static pitch adjustment only, i.e., when the model is non-rotating. Two identical locking pins are used to prevent rotation of the face gear relative to the forward hub. All blades are indexed to the common face gear by individual blade segment gears, attached to the butt end of each blade with dowel pins.

Multiple holes are provided in the forward hub half and in the face gear to accept the two locking pins. The holes are varied to provide a vernier pitch adjustment which permits fixed incremental changes in blade angle setting. The holes in both components are arranged in pairs, exactly 180 degrees apart, to permit the use of two identical locking pins. This provides structural redundancy while preserving the overall mass balance of the model at any angular setting.

8.1 Blade Angle Adjustments

Blade pitch angle adjustments are accomplished by unscrewing the spinner (left-hand thread) from the forward half of the hub and extracting both pitch locking pins. Internal machined threads are provided in the accessible end of each pin to facilitate pin removal. With the pins removed, the face gear becomes free to rotate and the pitch of all blades can be changed simultaneously by gripping one or more blades and gently "coaxing" the assembly to the desired setting. Caution is advised, however, in gripping these blades, because they are made of composite materials and the thin edges may be susceptible to damage. It is best to apply turning pressure to the material which is over the spar only, i.e., inner half of the blade, mid-chord region. Refer back to Figure 5-3, for blade construction details.

The vernier adjustment scheme used in the blade pitch change design consists of 24 holes in the face gear and 26 holes in the forward half hub. This vernier combination was chosen to satisfy the space limitations of the forward hub and face gear while accommodating the pin size dictated by centrifugal twisting moments. The requirement that two pitch locking pins be 180 degrees apart dictates that there be an even number of holes in both the hub and face gear. Based on the vernier combination above, and the blade gear to face gear ratio, the normal blade angle settings will be integer multiples of 2.885 degrees. This value was derived from the following equation:

$$360(1/24 - 1/26) \text{ (PDF/PDB)} = 2.885 \text{ degrees}$$

where: PDF - Face gear pitch diameter, 5.8057 cm. (2.2857 in.)
PDB - Blade gear pitch diameter, 2.3221 cm. (0.9142 in.)

Finer blade angle adjustments, can be obtained, if required, by re-indexing the alignment of the face gear to the blade segment gears. However, to do so requires separation of the front and rear hub halves. The smallest increment

possible using this method is 0.577 degree. Permissible blade angle settings within the aeroelastic model's geometric limitations can be expressed by the following equations:

$$a. \text{ BETA ref} = 57.70 + 75 [(P1 - 8I_{fg})/26 + I_{fg}/130] \text{ for BETA} > 57.7^\circ$$

$$b. \text{ BETA ref} = 57.70 + 75 [(P1 - 8I_{fg})/26 + I_{fg}/130] \text{ for BETA} < 57.7^\circ$$

where: BETA ref = Blade angle (degrees) at 28.62 cm (9.300 inch) radial station

I_{fg} = Index number of face gear (0,1,2,3,4)

P1 = Hub hole number for Pin 1

The expected low and high limits of the aeroelastic blade angle settings during normal operation are -6.00 and 90.00 degrees, respectively. Within this range a tabulated result of the above equations is provided in Appendix A. Results are arranged on five separate pages, with each page representing a separate indexing of the face gear relative to the blade gears. The first column on each page lists the static angles available while the next two columns list the corresponding hub hole locations for the locking pins.

One may enter the table with a desired static angle of say 53 degrees. The closest available setting is 53.085 found on the third page of Appendix A, with the face gear indexed at position 2.

Re-indexing the face gear requires removal of the spinner, extraction of both locking pins, and separation of front and rear hub halves. Before separation, the blades should be turned to an approximate blade angle setting of 42 degrees; this assures that the central tooth (marked with a 0) of all blade segment gears is pointing forward. The hub and blade assembly should be placed on a flat surface such that the back of the rear hub half is down and horizontal. Taking care not to disturb the blade angle setting, a both hub halves should be separated. The face gear resides in a tightly toleranced groove on the inside of the front hub half and thus should remain in its groove with the front half of the hub. Index numbers are located near tooth spaces on the outer periphery of the gear in the vicinity of blade shank bore number one. The face gear can now be re-indexed to position 2 by aligning the tooth space numbered (2) on the face gear with the number (0) on the inner chamfered surface of the forward hub half. Both hub halves may then be re-assembled, making sure that all blade angles remain at 42 degrees until the gears are meshed and the bolts tightened. The blades may then be turned to the 53 degree angle settings and the locking pins inserted into holes 14 and 1 of the front hub half.

8.2 Blade Twisting Loads

During normal operation each Prop-Fan blade produces a twisting moment about its pitch change axis. This twisting moment consists of two components. The

first is called the centrifugal twisting moment. This moment is produced by the centrifugal force trying to align the leading and trailing edge mass of non-circular sections with the plane of rotation. An explanation of the loading which causes centrifugal twisting moment is offered in Figure 8-2.

The second part of the total twisting moment is called the aerodynamic twisting moment (ATM). This moment arises because the chordwise location of the center of pressure at each blade section does not coincide with the pitch change axis along the span of the blade. In fact, for swept Prop-Fan blades such as this model, the effective center is forward of the pitch change axis, inboard, and aft near the tip, resulting in ATM's which approach zero. Obviously, if no air loads are applied, such as in a vacuum case, no ATM will be generated.

For the test speed of 8886 rpm, listed in Table 6-1 as the vacuum condition, each aeroelastic model blade generates 40.3 n-m (357 in-lbs) of centrifugal twisting moment and zero aerodynamic twisting moment. It can be shown that the centrifugal twisting moment varies sinusoidally with the blade angle by the following expression:

$$CTM = 357 \times \sin [(2) \times (\text{BETA} = 6.46)] \text{ in-lbs}$$

Graphic representation of the above expression is provided in Figure 8-3. For reference purposes, in the same figure, the blade angle setting for Feather is approximately 84 degrees while Reverse is about -6 degrees. The maximum CTM on this curve is (357 in-lbs) and occurs at 39 degrees. This peak was used for the design of all pitch-change hardware.

8.3 Blade Pitch Adjustment Pins

Because all eight blade gears are engaged to a common face gear (see Figure 8-1), the total twisting moment developed by all eight blades during testing must be reacted by the face gear. To prevent the face gear from turning, two locking pins placed 180 degrees apart are inserted through the forward half hub into the face gear. These pins were designed with the following design philosophy:

1. Use the maximum twisting moment generated by running the Prop-Fan at 8886 rpm in a takeoff/climb condition (see Table 6-1)
2. Use two identical 6.35 mm (0.25 inch) diameter pins 180 degrees apart for dynamic mass balance and structural redundancy.
3. Design for below material yield stresses for the worst loading condition.

Two analytical design approaches were examined. The first assumed that both locking pins shared the total load unequally at the rate of 2/3 on one pin and 1/3 on the second. The second concept assumed that the full load would

be borne by one pin. However, in the latter case, it was assumed that friction between the blade shank and the hub retention would help reduce the total twisting moment reacted by the face gear and held by the pin. A coefficient of friction equal to 0.005 was assumed between titanium and steel.

Bending stresses in the pin and contact stresses in the hub and face gear pin holes were calculated using both approaches described above. Both cases were investigated, because results were very close to one another. The second case with the load on a single pin, reduced by friction, gave slightly higher stresses. Therefore, shear stresses of the pin, hub and face gear were calculated using the second approach. Geometry and loads used in the analysis are shown in Figure 8-4. The results of this analysis are summarized below:

Max. shear stress in pin = $25580 \pm 25580 \text{ n/cm}^2$ ($37100 \pm 37100 \text{ psi}$)

Max. shear stress in hub = $3790 \pm 3790 \text{ n/cm}^2$ ($5500 \pm 5500 \text{ psi}$)

Max. shear stress in face gear = $8340 \pm 8340 \text{ n/cm}^2$ ($12100 \pm 12100 \text{ psi}$)

These three points are plotted in the Goodman design allowable diagram in Figure 8-5. All three cases demonstrate adequate shear stress margins.

Locking pin bending and contact stresses were investigated using a Hamilton Standard developed computer program. This pin-hole program allows either an interference or a clearance fit with combined lateral and bending loads. Determining the optimal engagement lengths and diametral clearances of the pin within the hub and face gear was an iterative process. Due to space limitations and pin removability considerations, it was desirable to provide a short engagement of the pin in the face gear and a loose fit of the pin in the hub hole. Several engagement lengths and clearance fits were explored. The lateral load reacted by the pin is a constant, but the slope and moment within the pin are functions of the geometry. A series of separate analyses were conducted at each end of the pin using the same lateral load and various assumed moments. This is illustrated in Figure 8-6. Compatibility for a particular geometry was established at the bending moment level where the calculated pin slopes, O_H and O_G matched one another at the hub/gear interface.

Based on the above analytical technique, both design approaches mentioned previously were analyzed, including: (1) two pins sharing the total lateral load with a distribution of 2/3 on one and 1/3 on the other, and (2) one pin alone carries a load which has been reduced by the contact friction between blade shank and hub. Pitch locking pin bending stresses are plotted in Figure 8-7; maximum contact stresses in the hub and face gear pin holes for the governing design approaches are plotted in Figure 8-8.

8.4 Face and Blade Gears Stresses

There are a total of eight (8) blade gears meshing with one face gear in the hub/spinner assembly. The blade gears are centered on the blade pitch change

axes whereas the face gear is centered on the hub axis of rotation. Each blade has one gear attached to its shank by three press-fit pins. The primary function of the blade and face gear components is to provide a means of setting the pitch of all blades simultaneously and to prevent them from turning under twisting moments generated during testing.

As mentioned earlier, once the desired pitch is achieved, the face gear is locked in position by two locking pins. These pins are inserted through holes on the front face of the forward half of the hub into matching holes on the face gear. The advantage of utilizing a face gear engaged to all eight (8) blade gears is that this scheme guarantees uniform blade angles among all eight (8) blades. Blade angle changes can also be calibrated based on one single blade angle setting.

Gear geometries and other design data for the blade and face gears are listed in the table below. Stress calculation show that considerable design margins exist for both gears. The gear stress results are plotted on a Goodman design diagram in Figure 8-9.

<u>Item</u>		<u>Blade Gear</u>	<u>Face Gear</u>
NT	Number of teeth	5 of 16	40
Pd	Pitch diameter, cm (in.)	2.3221 (0.9142)	5.8057 (2.2857)
Dp	Diametral pitch, cm (in.)	40.64 (16.00)	40.64 (16.00)
O	Pressure angle (degree)	27 30'	27 30'
F	Face width, mm (in.)	6.350 (0.250)	6.350 (0.250)
T	Applied torque, n-m (in-lbs.)	40.3 (357)	100.9 (893)
W	Tooth load, newtons (lbs.)	34,710 (781)	34,710 (781)
X	Lewis X factor, mm (in.)	1.27 (.584)	1.27 (.584)
Sb	Steady bending stress, n/cm ² (psi)	64300 (93721)	53850 (78100)
R	Fillet radius, mm (in.)	0.023 (0.023)	0.023 (0.023)
Kt	Stress Concentration factor (N/D)	1.50	1.80
LCF	Low cycle fatigue str., n/cm ² (psi)	32300+48460 (46860+70291)	26920+48460 (39050+70291)

Stress formulae:

$$\begin{aligned}
 W &= 2 \times T/Pd \\
 Sb &= 1.5 \times W/(F \times X) \\
 LCF &= Sb/2 + Kt \times (Sb/2)
 \end{aligned}$$

9.0 CONCLUSIONS

As has been stated, the main objectives of the 2 ft. diameter model were to simulate the aeroelastic behavior of the SR-7L blade during model testing on the Jetstar aircraft, and to be able to withstand testing in the NASA/Lewis 8 ft. by 6 ft. wind tunnel. It is appropriate here to evaluate whether or not these goals have been achieved.

During a lengthy discussion on the similarity requirements for aeroelastic models (Section 4.1), it was found that several scaling parameters had to be matched. Most of these parameters were satisfied by the nature of the test program; that is, the model would be tested at the same atmospheric conditions, and with the same tip speed and forward velocity as the SR-7L. Also, the external shape of the model blade was scaled identically from the SR-7L blade. But in order to satisfy the remaining scaling parameters, the construction of the model would have to be identical to the SR-7L. Because of manufacturing limitations, this was found to be impossible. It was therefore assumed that if the mass and stiffness distributions of the model blade were matched with those of the SR-7L blade, all the requirements for an aeroelastic scale model could be met.

Although some fine-tuning was required, analyses of a model constructed under this assumption showed good correlation with the SR-7L. As described in Section 6.2.4, frequencies agreed within 10% of the SR-7L and mode shapes were very similar.

Flutter analysis of the aeroelastic model blade indicates that it accurately simulates the stability of the SR-7L at the 10,668 meter (35,000 ft.) and design cruise condition for the Jetstar (NASA aircraft) installation, and adequately simulates the low speed, low altitude takeoff/climb condition for the same installation. This implies that satisfactory simulation should exist over the entire operating spectrum on the aircraft.

Testing limitations at high Mach numbers may exist, however, in the 2.44 meter (8 ft.) by 1.83 meter (6 ft.) NASA Lewis wind tunnel because predictions indicate the model blade is only marginally stable at high speeds. This stability reduction is due to increased air density, higher rotational speeds, and consequently greater blade deflections for wind tunnel operation. This may limit aerodynamic performance measurements, but could serve as an important tool for calibration of the aeroelastic stability analysis code.

The stress results in Section 6.2.3 were encouraging. Although only steady stress analyses were performed, the remaining cyclic stress capacities appear to be adequate for the operating conditions examined. However, blade cyclic stresses should be monitored carefully to ensure that they do not exceed predetermined allowable levels. Even though the SR-7L may be subjected to many operating environments, the model blade operating conditions should be limited to those described in this report. Additional analyses should be considered for conditions significantly different than those analyzed.

Even with these limitations the scale model should be a useful tool in providing informative data as to the aeroelastic behavior of the SR-7L.

APPENDIX A

FACE GEAR INDEXED AT POSITION NO. 0

STATIC BLADE ANGLE SETTING* (DEGREES)	FIRST PIN IN HUB HOLE NO.	SECOND PIN IN HUB HOLE NO.
-5.762	4	17
-2.877	5	18
0.008	6	19
2.892	7	20
5.777	8	21
8.662	9	22
11.546	10	23
14.431	11	24
17.315	12	25
20.200	13	0
23.085	14	1
25.969	15	2
28.854	16	3
31.738	17	4
34.623	18	5
37.508	19	6
40.392	20	7
43.277	21	8
46.162	22	9
49.046	23	10
51.931	24	11
54.815	25	12
57.700**	0	13
60.585	1	14
63.469	2	15
66.354	3	16
69.238	4	17
72.123	5	18
75.008	6	19
77.892	7	20
80.777	8	21
83.662	9	22
86.546	10	23
89.431	11	24

* AT 23.62 CM (9.30 INCH) PLANAR (MFG) REF. STATION

** SETTING FOR DESIGN CRUISE CONDITION

NOTE: TABLES ARE BASED ON DISCUSSION IN SECTION 8.1

APPENDIX A (CONTINUED)

FACE GEAR INDEXED AT POSITION NO. 1

STATIC BLADE ANGLE SETTING* (DEGREES)	FIRST PIN IN HUB HOLE NO.	SECOND PIN IN HUB HOLE NO.
-5.185	12	25
-2.300	13	0
0.585	14	1
3.469	15	2
6.354	16	3
9.238	17	4
12.123	18	5
15.008	19	6
17.892	20	7
20.777	21	8
23.662	22	9
26.546	23	10
29.431	24	11
32.315	25	12
35.200	0	13
38.085	1	14
40.969	2	15
43.854	3	16
46.738	4	17
49.623	5	18
52.508	6	19
55.392	7	20
58.277**	8	21
61.162	9	22
64.046	10	23
66.931	11	24
69.815	12	25
72.700	13	0
75.585	14	1
78.469	15	2
81.354	16	3
84.238	17	4
87.123	18	5
90.008	19	6

* AT 23.62 CM (9.30 INCH) PLANAR (MFG) REF. STATION

** SETTING FOR DESIGN CRUISE CONDITION (REF. PG. A-1)
PLUS 1(0.577) DEGREES.

NOTES: TABLES ARE BASED ON DISCUSSION IN SECTION 8.1
INDEXING FACE GEAR REQUIRES DISASSEMBLY OF HUB.

APPENDIX A (CONTINUED)

FACE GEAR INDEXED AT POSITION NO. 2

STATIC BLADE ANGLE SETTING* (DEGREES)	FIRST PIN IN HUB HOLE NO.	SECOND PIN IN HUB HOLE NO.
-4.608	20	7
-1.723	21	8
1.162	22	9
4.046	23	10
6.931	24	11
9.815	25	12
12.700	0	13
15.585	1	14
18.469	2	15
21.354	3	16
24.238	4	17
27.123	5	18
30.008	6	19
32.892	7	20
35.777	8	21
38.662	9	22
41.546	10	23
44.431	11	24
47.315	12	25
50.200	13	0
53.085	14	1
55.969	15	2
58.854**	16	3
61.738	17	4
64.623	18	5
67.508	19	6
70.392	20	7
73.277	21	8
76.162	22	9
79.046	23	10
81.931	24	11
84.815	25	12
87.700	0	13
90.585	1	14

* AT 23.62 CM (9.30 INCH) PLANAR (MFG) REF. STATION

** SETTING FOR DESIGN CRUISE CONDITION (REF. PG. A-1)
PLUS 2(0.577) DEGREES.

NOTES: TABLES ARE BASED ON DISCUSSION IN SECTION 8.1
INDEXING FACE GEAR REQUIRES DISASSEMBLY OF HUB.

APPENDIX A (CONTINUED)

FACE GEAR INDEXED AT POSITION NO. 3

STATIC BLADE ANGLE SETTING* (DEGREES)	FIRST PIN IN HUB HOLE NO.	SECOND PIN IN HUB HOLE NO.
-4.031	2	15
-1.146	3	16
1.738	4	17
4.623	5	18
7.508	6	19
10.392	7	20
13.277	8	21
16.162	9	22
19.046	10	23
21.931	11	24
24.815	12	25
27.700	13	0
30.585	14	1
33.469	15	2
36.354	16	3
39.238	17	4
42.123	18	5
45.008	19	6
47.892	20	7
50.777	21	8
53.662	22	9
56.546	23	10
59.431**	24	11
62.315	25	12
65.200	0	13
68.085	1	14
70.969	2	15
73.854	3	16
76.738	4	17
79.623	5	18
82.508	6	19
85.392	7	20
88.277	8	21
91.162	9	22

* AT 23.62 CM (9.30 INCH) PLANAR (MFG) REF. STATION

** SETTING FOR DESIGN CRUISE CONDITION (REF. PG. A-1)
PLUS 3(0.577) DEGREES.

NOTES: TABLES ARE BASED ON DISCUSSION IN SECTION 8.1
INDEXING FACE GEAR REQUIRES DISASSEMBLY OF HUB

APPENDIX A (CONTINUED)

FACE GEAR INDEXED AT POSITION NO. 4

STATIC BLADE ANGLE SETTING* (DEGREES)	FIRST PIN IN HUB HOLE NO.	SECOND PIN IN HUB HOLE NO.
-3.454	10	23
-0.569	11	24
2.315	12	25
5.200	13	0
8.085	14	1
10.969	15	2
13.854	16	3
16.738	17	4
19.623	18	5
22.508	19	6
25.392	20	7
28.277	21	8
31.162	22	9
34.046	23	10
36.931	24	11
39.815	25	12
42.700	0	13
45.585	1	14
48.469	2	15
51.354	3	16
54.238	4	17
57.123	5	18
60.008**	6	19
62.892	7	20
65.777	8	21
68.662	9	22
71.546	10	23
74.431	11	24
77.315	12	25
80.200	13	0
83.085	14	1
85.969	15	2
88.854	16	3
91.739	17	4

* AT 23.62 CM (9.30 INCH) PLANAR (MFG) REF. STATION

** SETTING FOR DESIGN CRUISE CONDITION (REF. PG. A-1)
PLUS 4(0.577) DEGREES

NOTES: TABLES ARE BASED ON DISCUSSION IN SECTION 8.1
INDEXING FACE GEAR REQUIRES DISASSEMBLY OF HUB.

APPENDIX B
LIST OF FIGURES

- 4-1. Model Blade Coordinate System
- 4-2. 2.74 Meter (9 Ft. Dia.) SR-7L - Frequencies and Mode Shapes
- 4-3. Scaled Down SR-7L - Frequencies and Mode Shapes
- 4-4. Simulation of Retention Bending Stiffness
- 4-5. Scaled-Down SR-7L With 1.588 cm. (.625 in) Dia. Titanium Shank -
Clamped Retention - Frequencies and Mode Shapes
- 4-6. First Finite Element Model of New-Construction Blade -
Frequencies and Mode Shapes
- 4-7. Final SR-7L Blade - Frequencies and Mode Shapes
- 4-8. Finite Element Scale Model of DDR SR-7L Blade - Incorrect Graphite
Orientation - Frequencies and Mode Shapes
- 5-1. Planform Comparison
- 5-2. Ply Layup Cross-Sections
- 5-3. Untwisted Planform, Composite Design
- 6-1. Finite Element Model Section Detail
- 6-2. Finite Element Modeling
- 6-3. Model Shank Retention
- 6-4. Blade Boundary Conditions
- 6-5. Comparison of Campbell Diagram and "modified Campbell Diagram"
- 6-6. Deflection Contour Plots - 35000 Ft. Altitude - Cruise Condition
- 6-7. Deflection Contour Plot - 8 x 6 Wind Tunnel Condition (8622 RPM)
- 6-8. Blade Tip Deflections
- 6-9. Directions of Applied Blade Loads and Moments
- 6-10. Spar Surface Radial Stress - 35000 Ft. Altitude - Cruise Condition
- 6-11. Spar Surface Radial Stress- Wind Tunnel Condition (8622 RPM)
- 6-12. Spar Surface Radial Stress - Takeoff Climb Condition
- 6-13. Goodman Diagram - Spar Tensile Stress - Shank Area
- 6-14. Goodman Diagram - Spar Tensile Stress - Airfoil Area
- 6-15. Shell Surface Radial Strain - 35000 Ft. Altitude - Cruise Condition
- 6-16. Shell Surface Radial Strain - Wind Tunnel - Cruise Condition
- 6-17. Shell Surface Radial Strain - Takeoff Climb Condition
- 6-18. Goodman Diagram - Shell Tensile Stress - Fiberglass Cloth
- 6-19. Goodman Diagram - Shell Tensile Stress - Graphite
- 6-20. Foam Surface Effective Stress - 10668 meter (35000 Ft.) Altitude
Cruise Condition
- 6-21. Foam Surface Effective Stress - Wind Tunnel - Cruise Condition
- 6-22. Foam Surface Effective Stress - Takeoff Climb Condition
- 6-23. Goodman Diagram - Foam Tensile Stress
- 6-24. Modified Campbell Diagram
- 6-25. Campbell Diagram - Aeroelastic Model
- 6-26. Vibration Mode Shapes - 35000 Ft. Altitude - Cruise Condition -
1st Mode
- 6-27. Vibration Mode Shapes - 35000 Ft. Altitude - Cruise Condition -
2nd Mode
- 6-28. Vibration Mode Shapes - 35000 Ft. Altitude - Cruise Condition -
3rd Mode

- 6-29. Vibration Mode Shapes - 35000 Ft. Altitude - Cruise Condition - 4th Mode
- 6-30. Vibration Mode Shapes - 35000 Ft. Altitude - Cruise Condition - 5th Mode
- 6-31. Vibration Mode Shapes - 8 X 6 Wind Tunnel Cruise Condition
- 6-32. SR-7A Aeroelastic Model Stability - Design Cruise Condition
- 6-33. SR-7A Aeroelastic Model Stability Comparison
- 6-34. SR-7A Aeroelastic Model Stability - Takeoff/Climb Condition
- 6-35. SR-7A Aeroelastic Model Stability - Wind Tunnel Condition
- 6-36. SR-7A Aeroelastic Model Stability - Wind Tunnel Condition - Modified Analysis
- 7-1. Blade Retention and Hub Detail Sketch
- 7-2. Blade Retention Loads
- 7-3. Blade Retention Stresses
- 7-4. Goodman Diagram - Contact Stress Allowable
- 7-5. Forward Hub 2-D Model
- 7-6. Forward Hub Deflected Shape
- 7-7. Hub Lip Stresses
- 7-8. SR-7L Bolt Loads
- 7-9. SR-7L Bolt Stress
- 8-1. Pitch Change Detail Sketch
- 8-2. Origin of Centrifugal Twisting Moment
- 8-3. SR-7L Blade Centrifugal Twisting Moment
- 8-4. Pitch Adjustment Pin - Shear Stresses
- 8-5. Shear Stress Goodman Diagram
- 8-6. Pitch Adjustment Pin - Bending and Contact Stresses
- 8-7. Pitch Lock Pin Bending Stress - Goodman Diagram
- 8-8. Hertz Contact Stress Allowable
- 8-9. Goodman Diagram - Gear Stresses

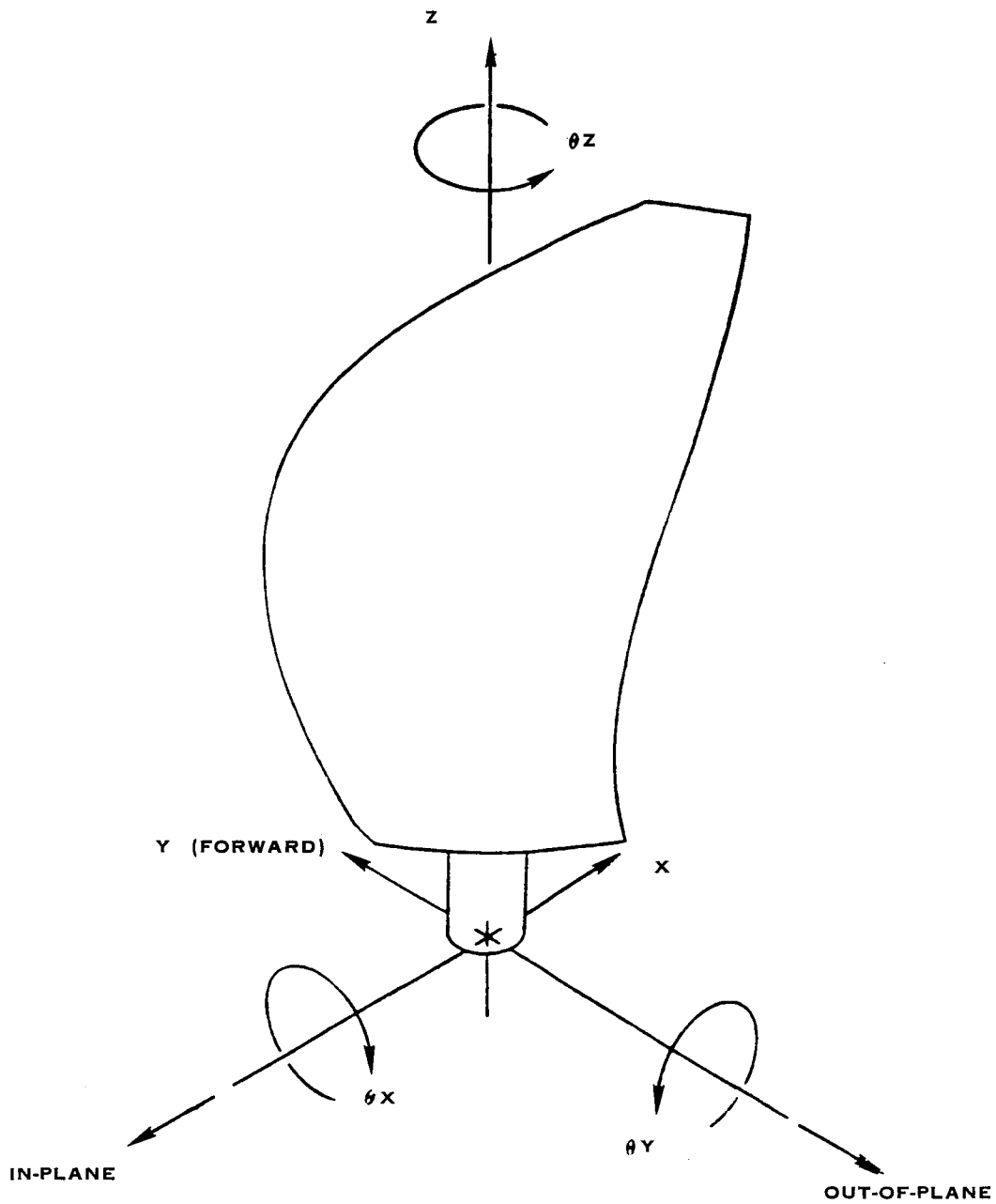
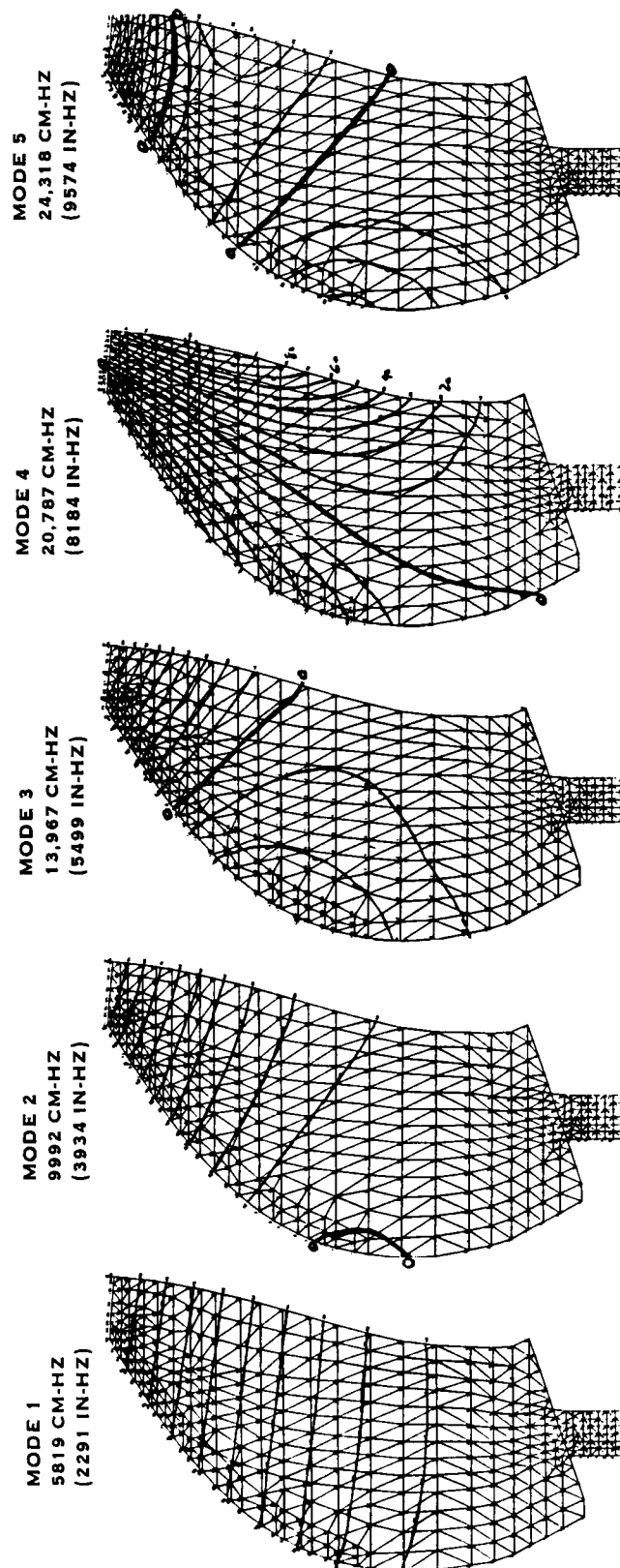
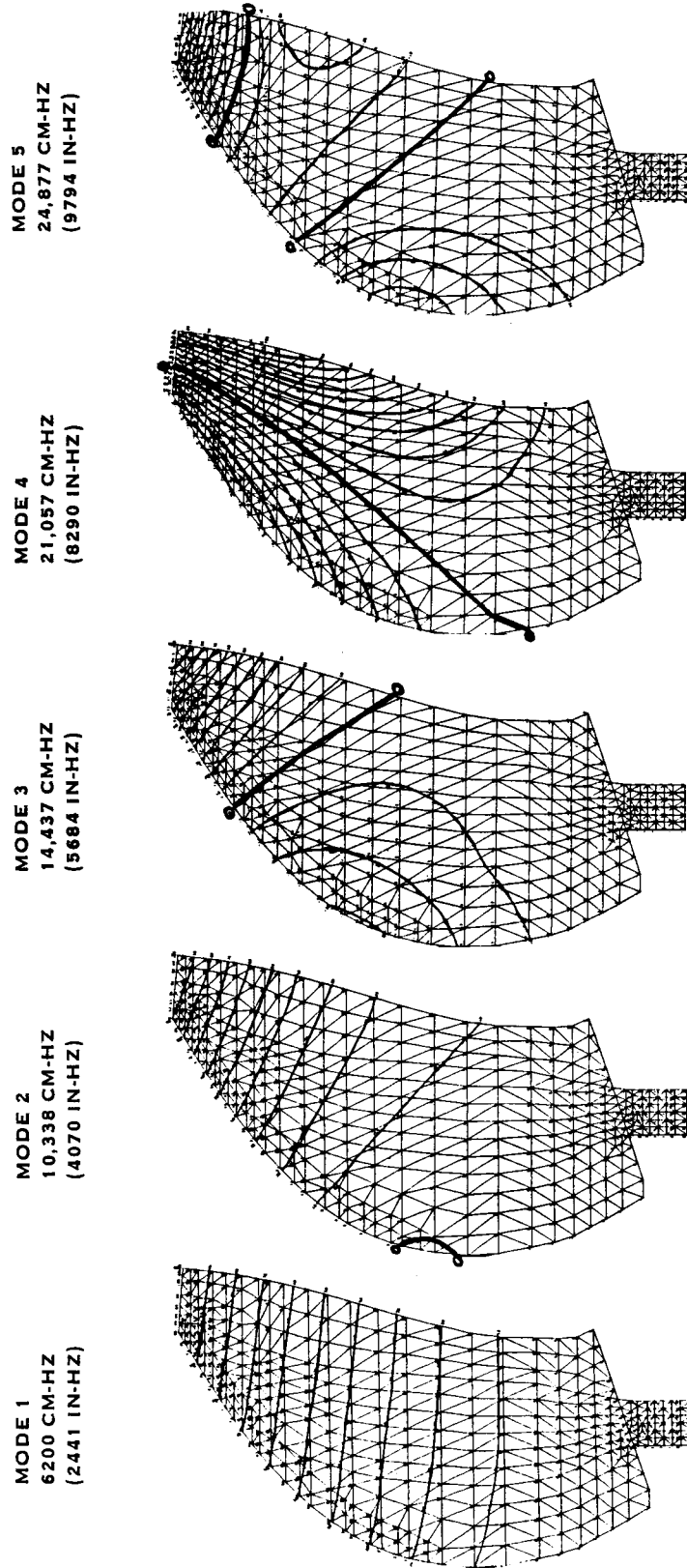


FIGURE 4-1. MODEL BLADE COORDINATE SYSTEM



NOTE: FREQUENCIES ARE MULTIPLIED BY TIP RADIUS

FIGURE 4-2. 2.74 METER (9 FT.) DIA. SR-7L FREQUENCIES AND MODE SHAPES



NOTE: FREQUENCIES ARE MULTIPLIED BY TIP RADIUS

FIGURE 4-3. SCALED-DOWN SR-7L FREQUENCIES AND MODE SHAPES

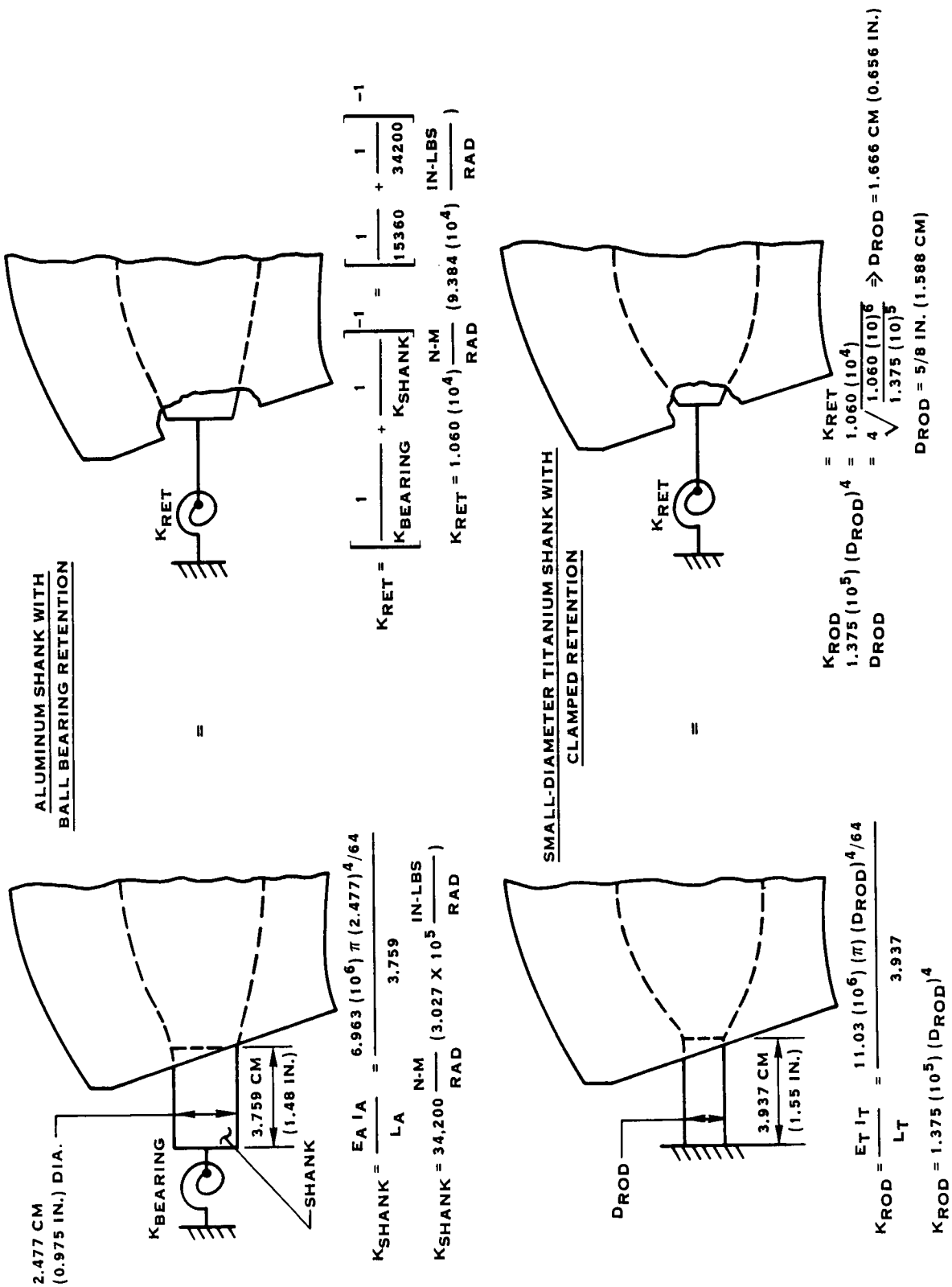
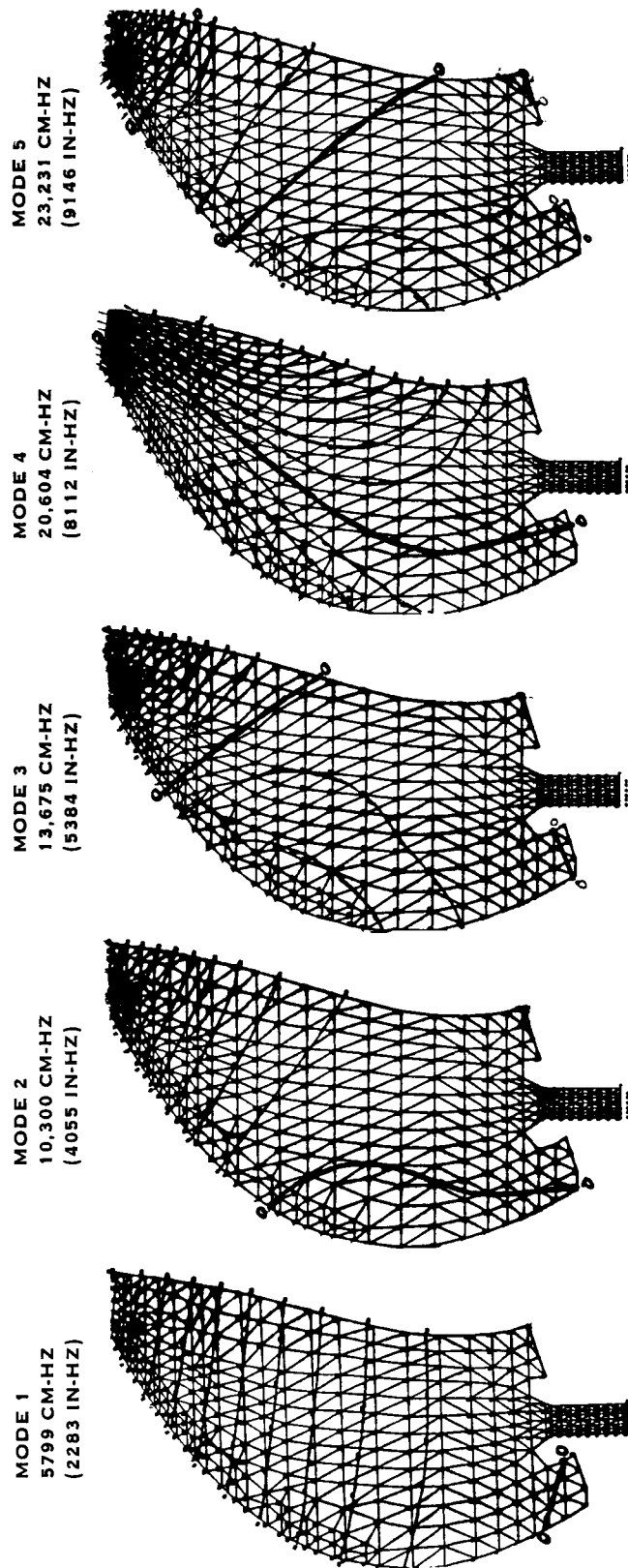
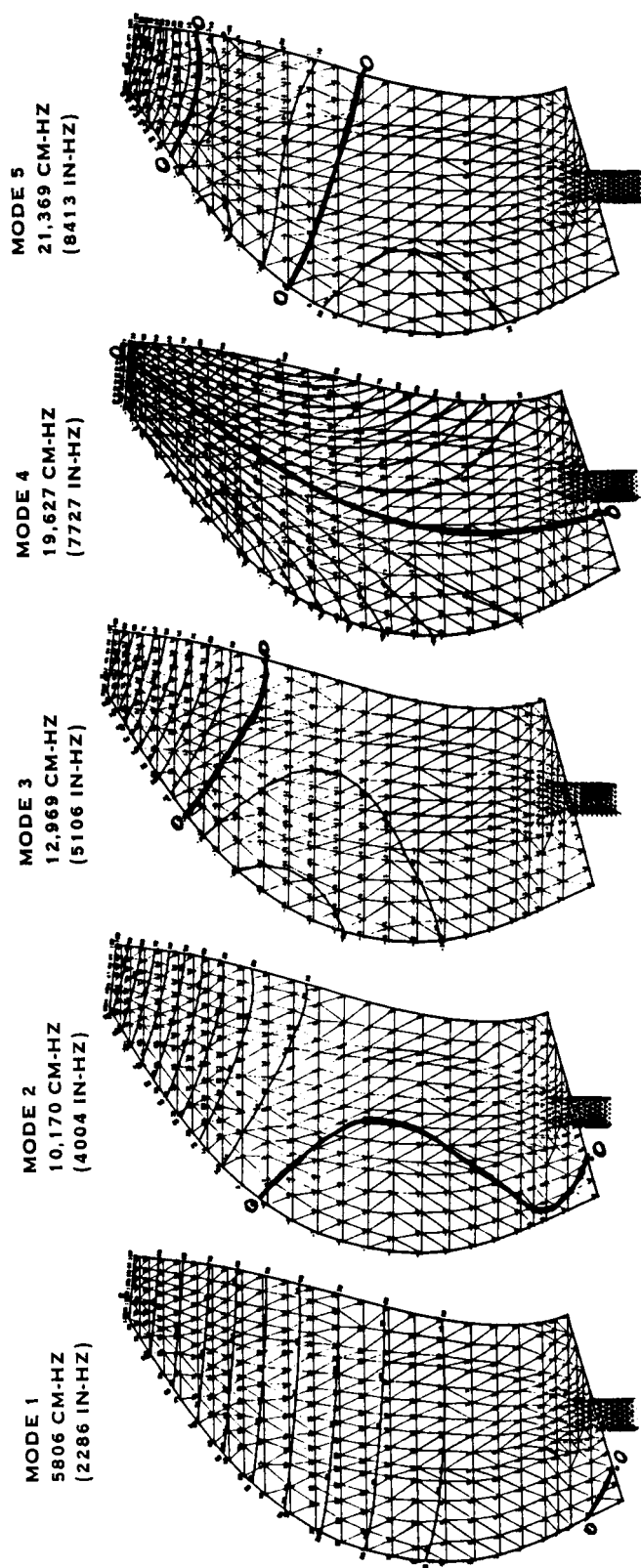


FIGURE 4-4. SIMULATION OF RETENTION BENDING STIFFNESS



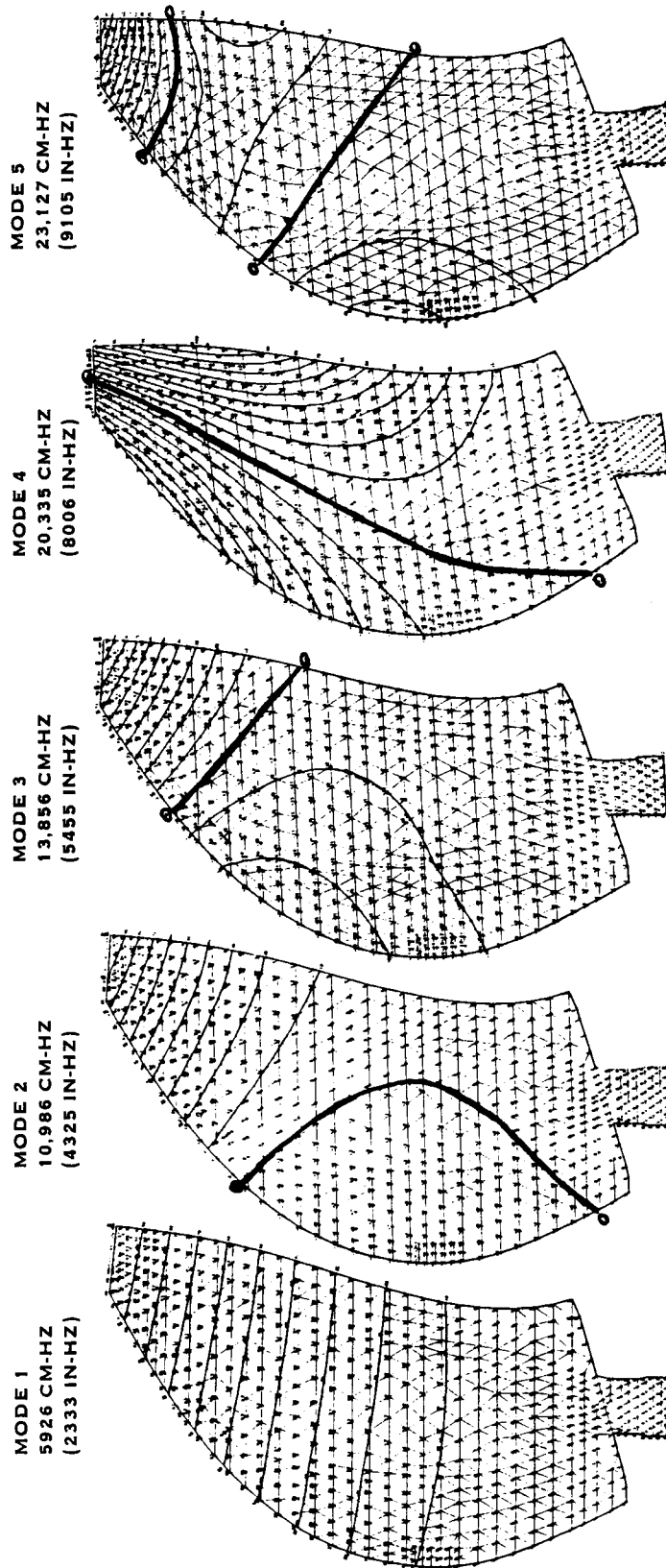
NOTE: FREQUENCIES ARE MULTIPLIED BY TIP RADIUS

FIGURE 4-5. SCALED-DOWN SR-7L WITH 1.588 CM (0.625 IN) DIA.
TITANIUM SHANK - CLAMPED RETENTION
FREQUENCIES AND MODE SHAPES



NOTE: FREQUENCIES ARE MULTIPLIED BY TIP RADIUS

FIGURE 4-6. FIRST FINITE ELEMENT MODEL OF NEW-CONSTRUCTION BLADE
FREQUENCIES AND MODE SHAPES



NOTE: FREQUENCIES ARE MULTIPLIED BY TIP RADIUS

FIGURE 4-7. FINAL SR-7L - FREQUENCIES AND MODE SHAPES

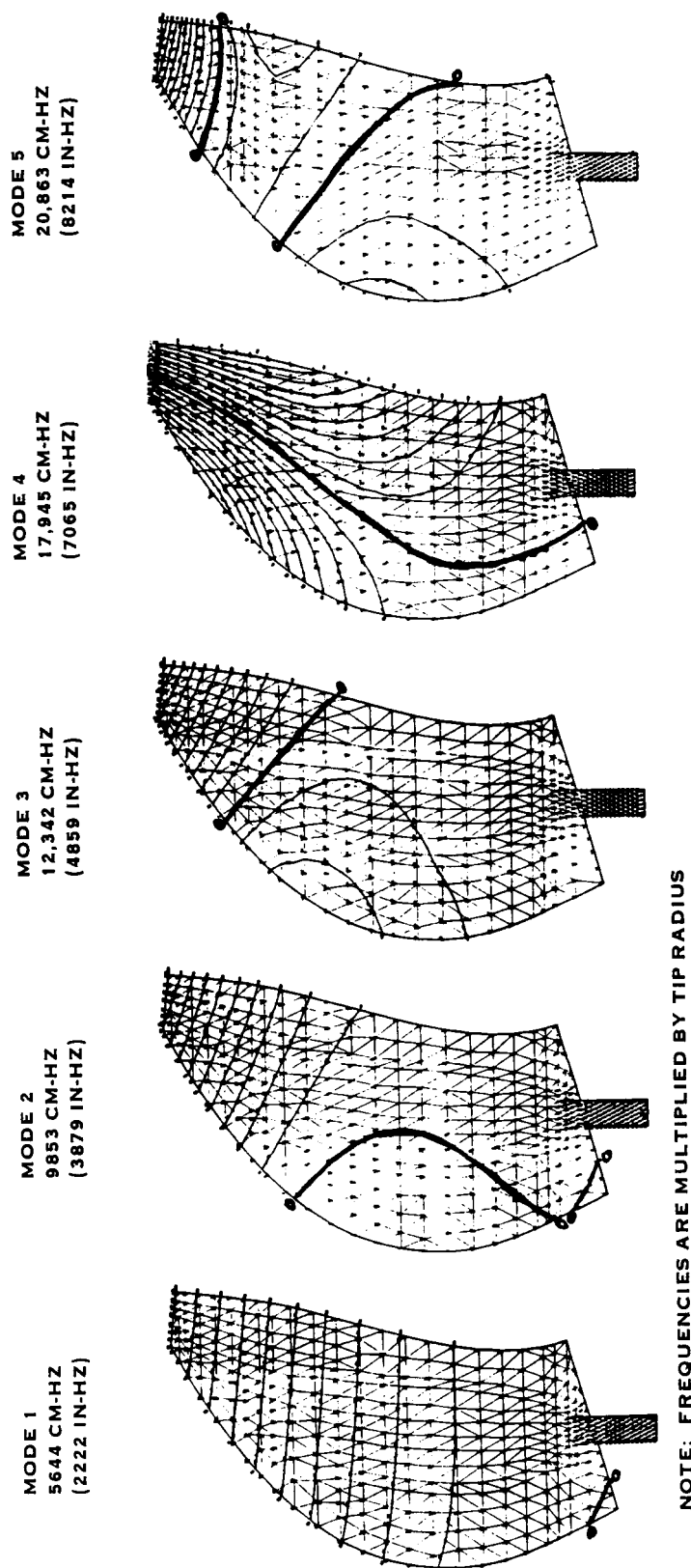


FIGURE 4-8. FINITE ELEMENT SCALE MODEL OF DDR SR-7L BLADE
INCORRECT GRAPHITE ORIENTATION
FREQUENCIES AND MODE SHAPES

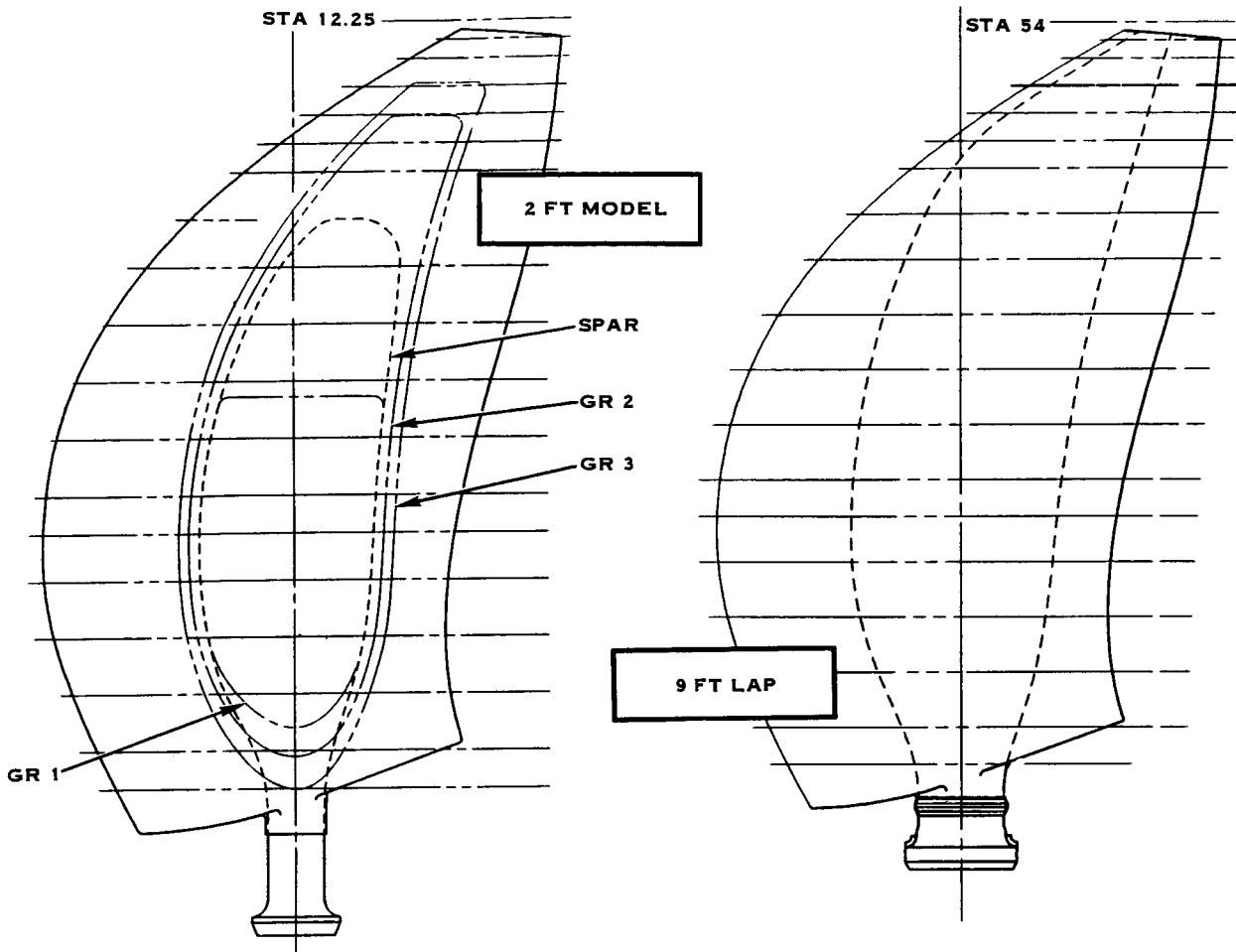


FIGURE 5-1. PLANFORM COMPARISON

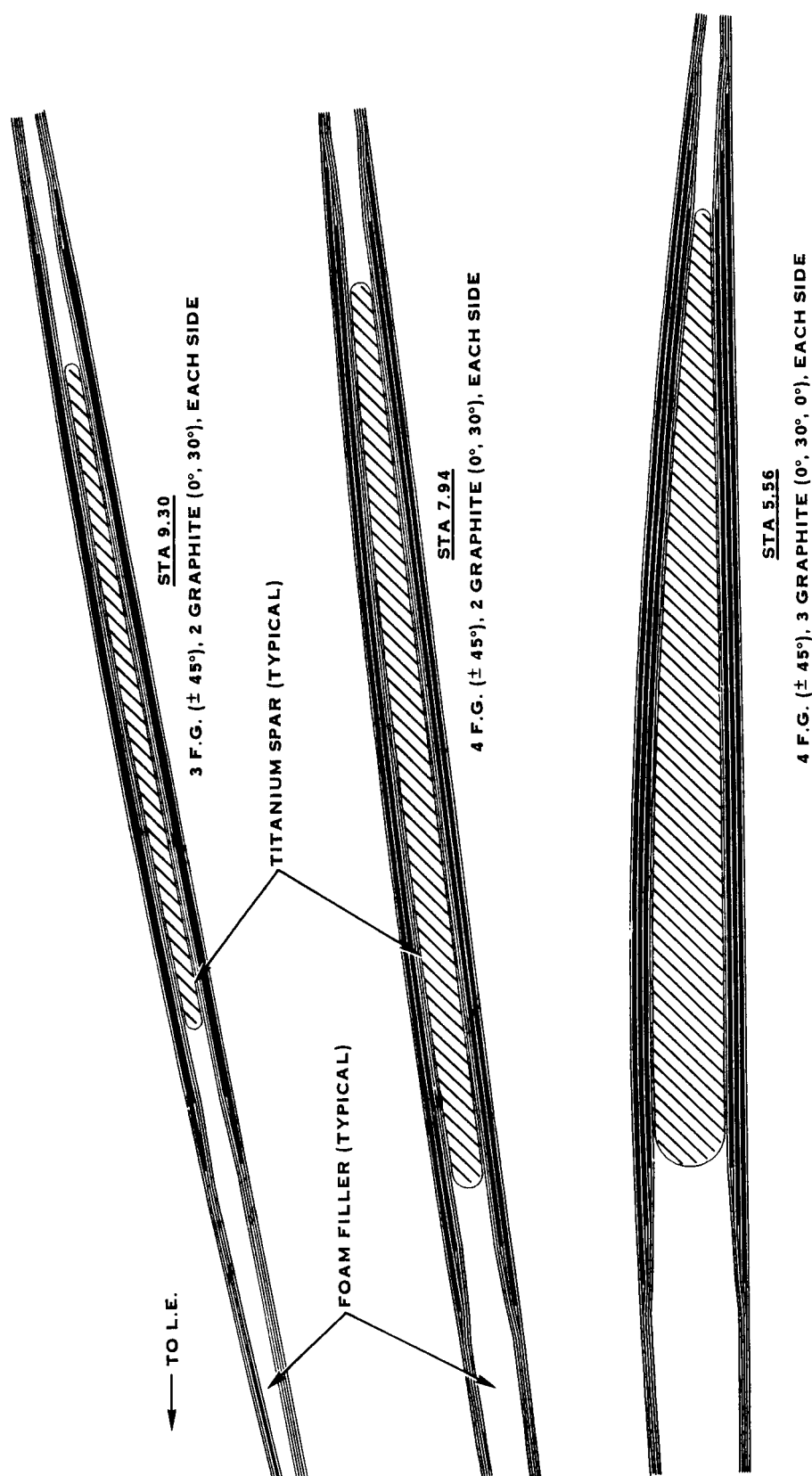


FIGURE 5-2. PLY LAYUP CROSS-SECTIONS

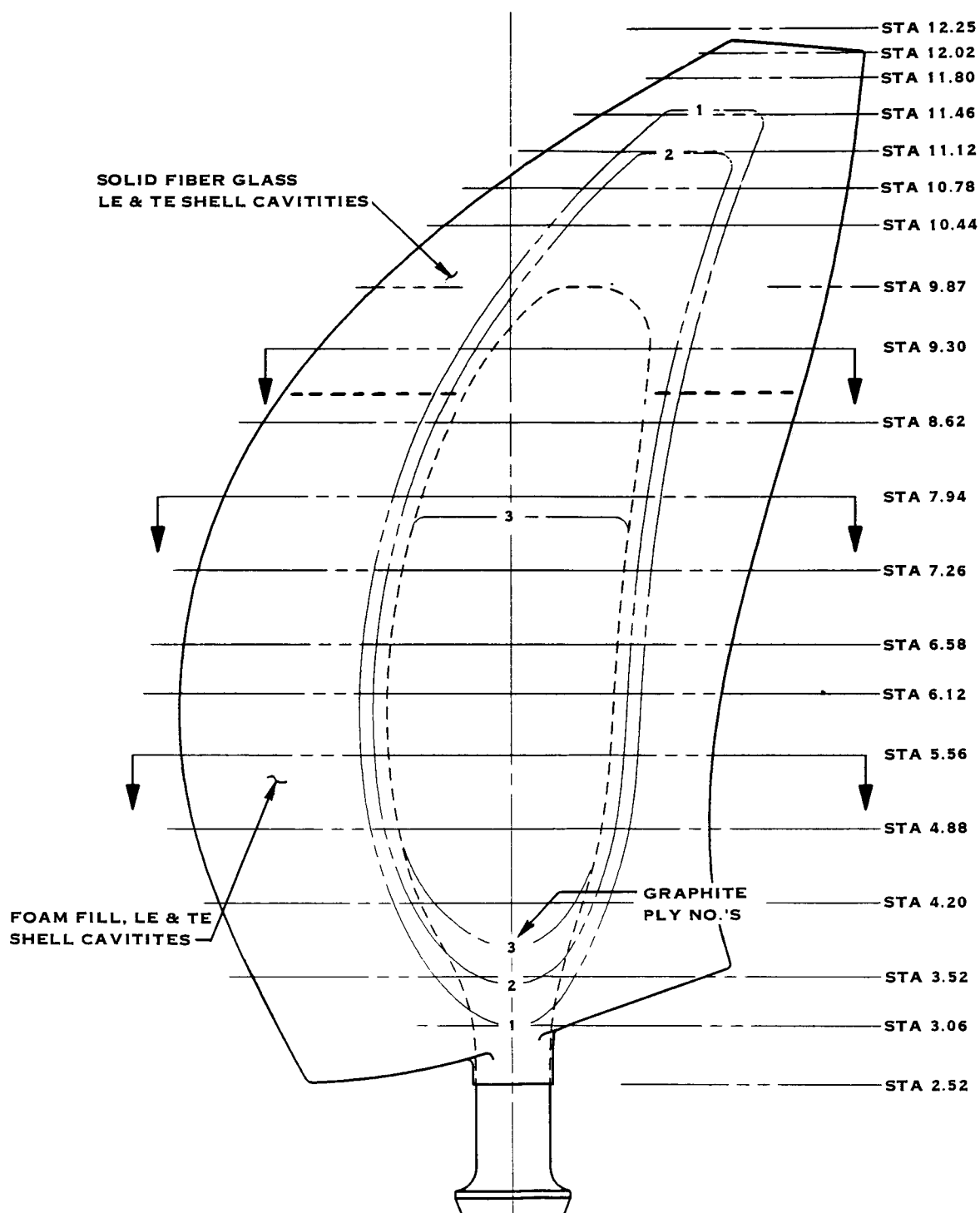
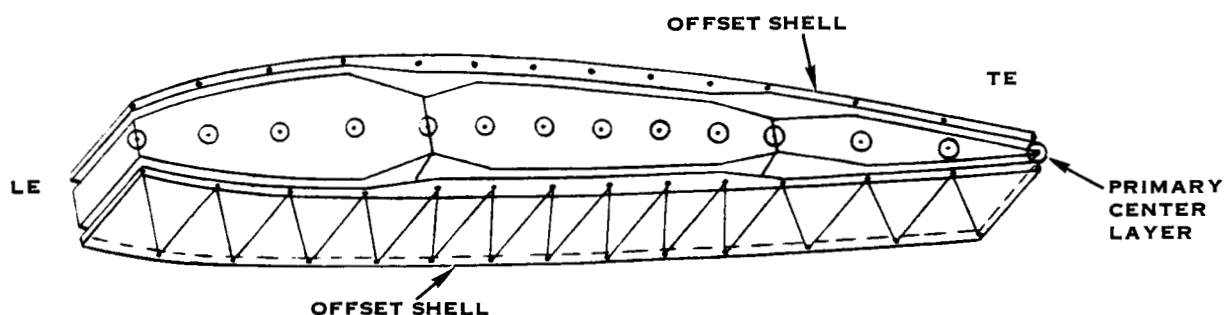


FIGURE 5-3. UNTWISTED PLANFORM, COMPOSITE DESIGN



- CENTER LAYER: LE & TE ARE FOAM, MIDDLE IS TI SPAR
- OFFSET SHELLS RIGIDLY ATTACHED TO CENTER LAYER GRID POINTS

FIGURE 6-1. FINITE ELEMENT MODEL SECTION DETAIL

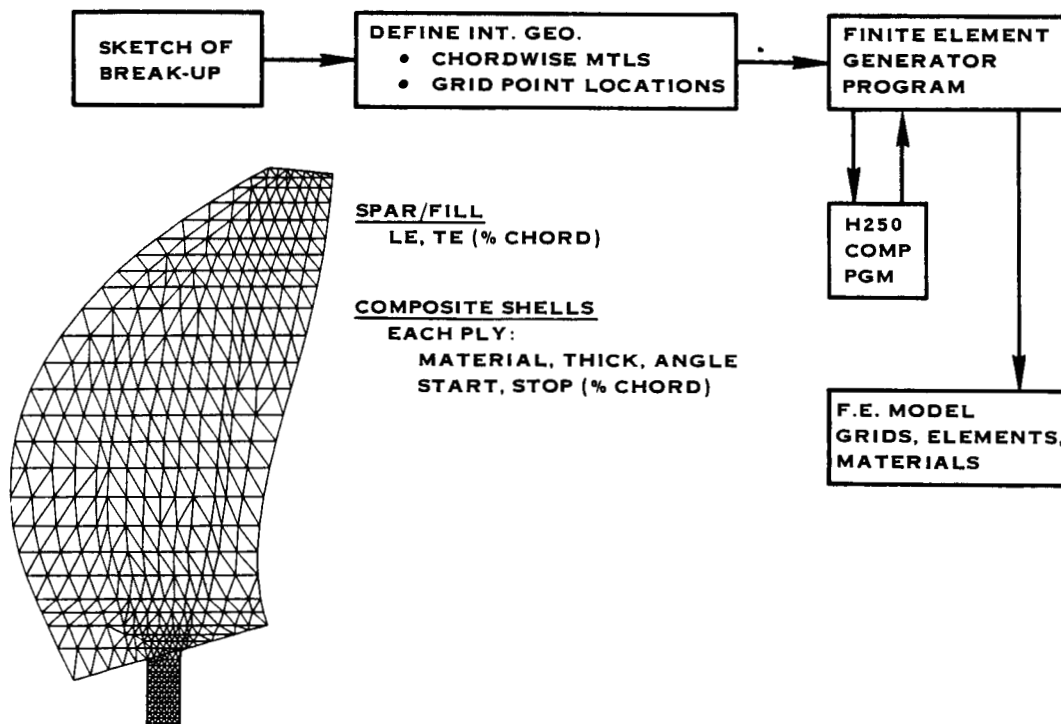


FIGURE 6-2. FINITE ELEMENT MODELING

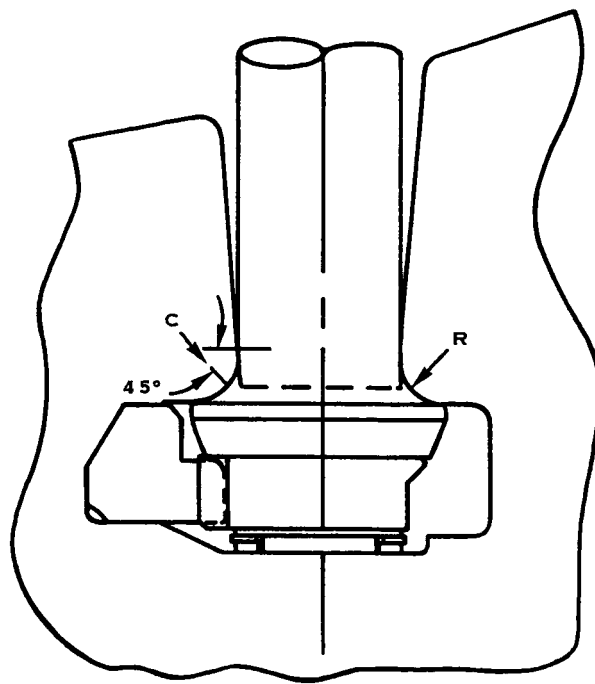


FIGURE 6-3. MODEL SHANK RETENTION

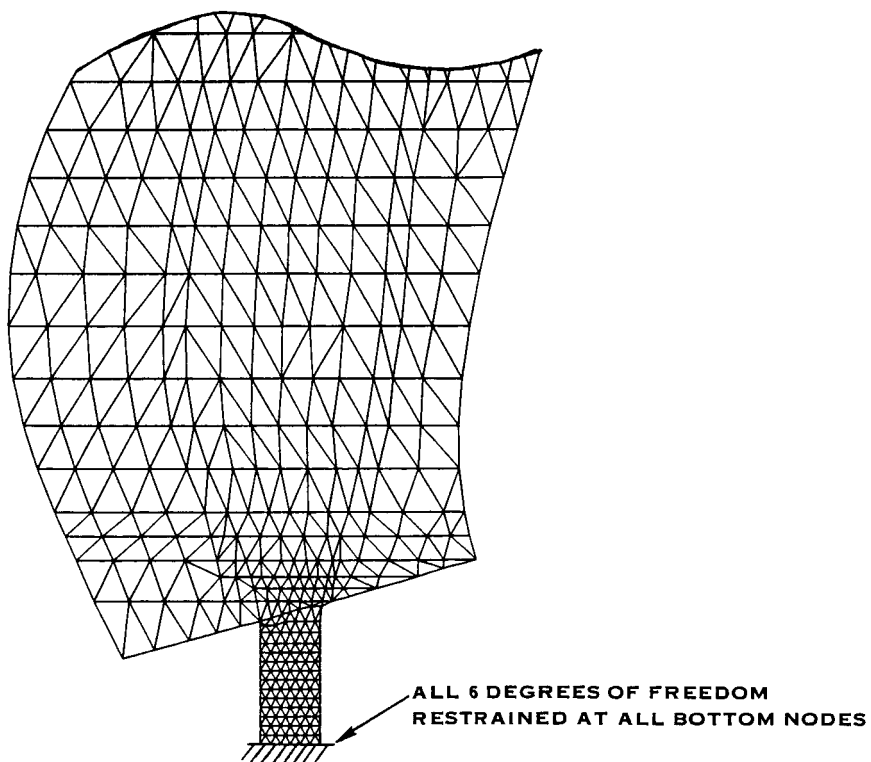


FIGURE 6-4. BLADE BOUNDARY CONDITIONS

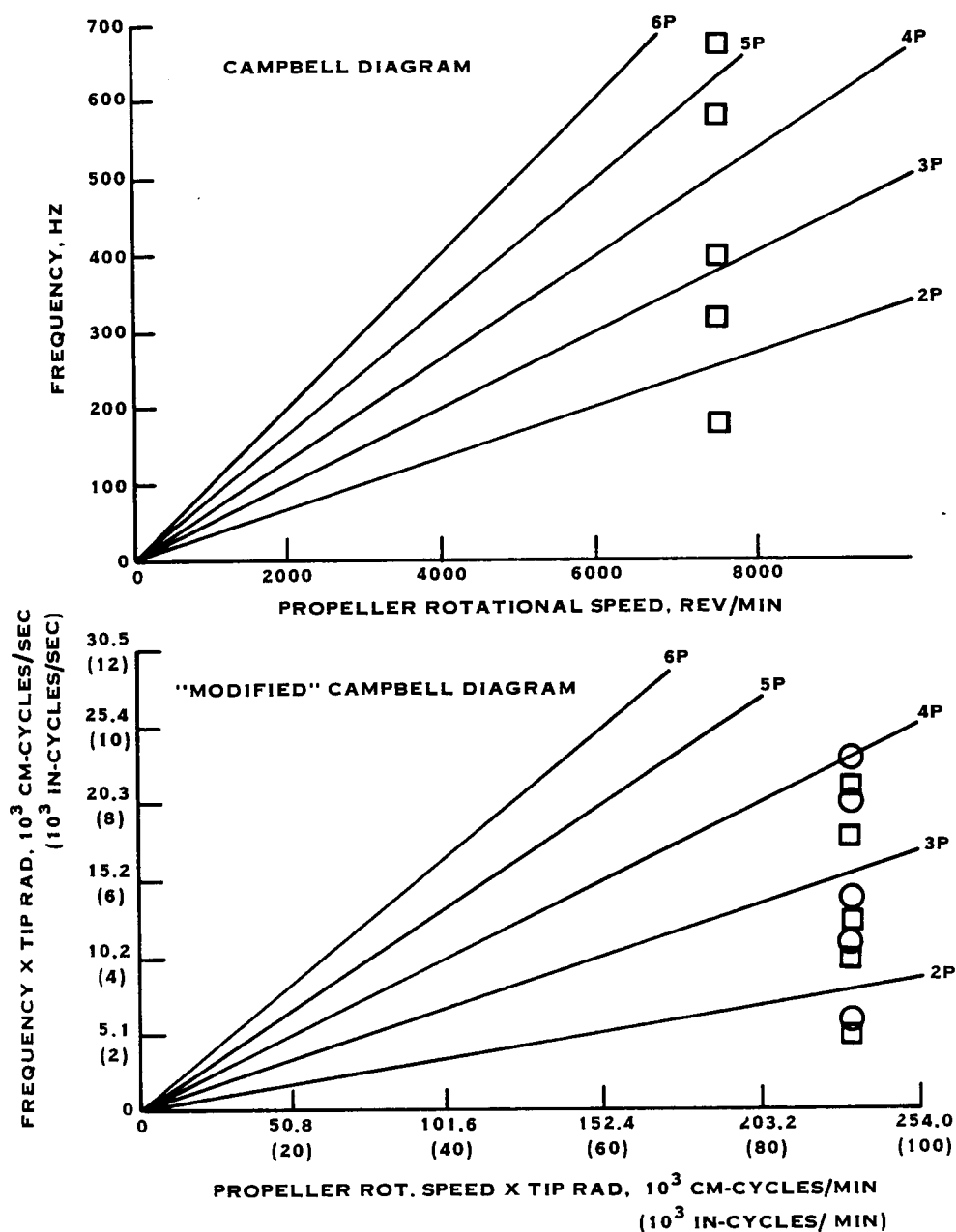


FIGURE 6-5. COMPARISON OF CAMPBELL DIAGRAM AND "MODIFIED" CAMPBELL DIAGRAM

ORIGINAL PAGE IS
OF POOR QUALITY

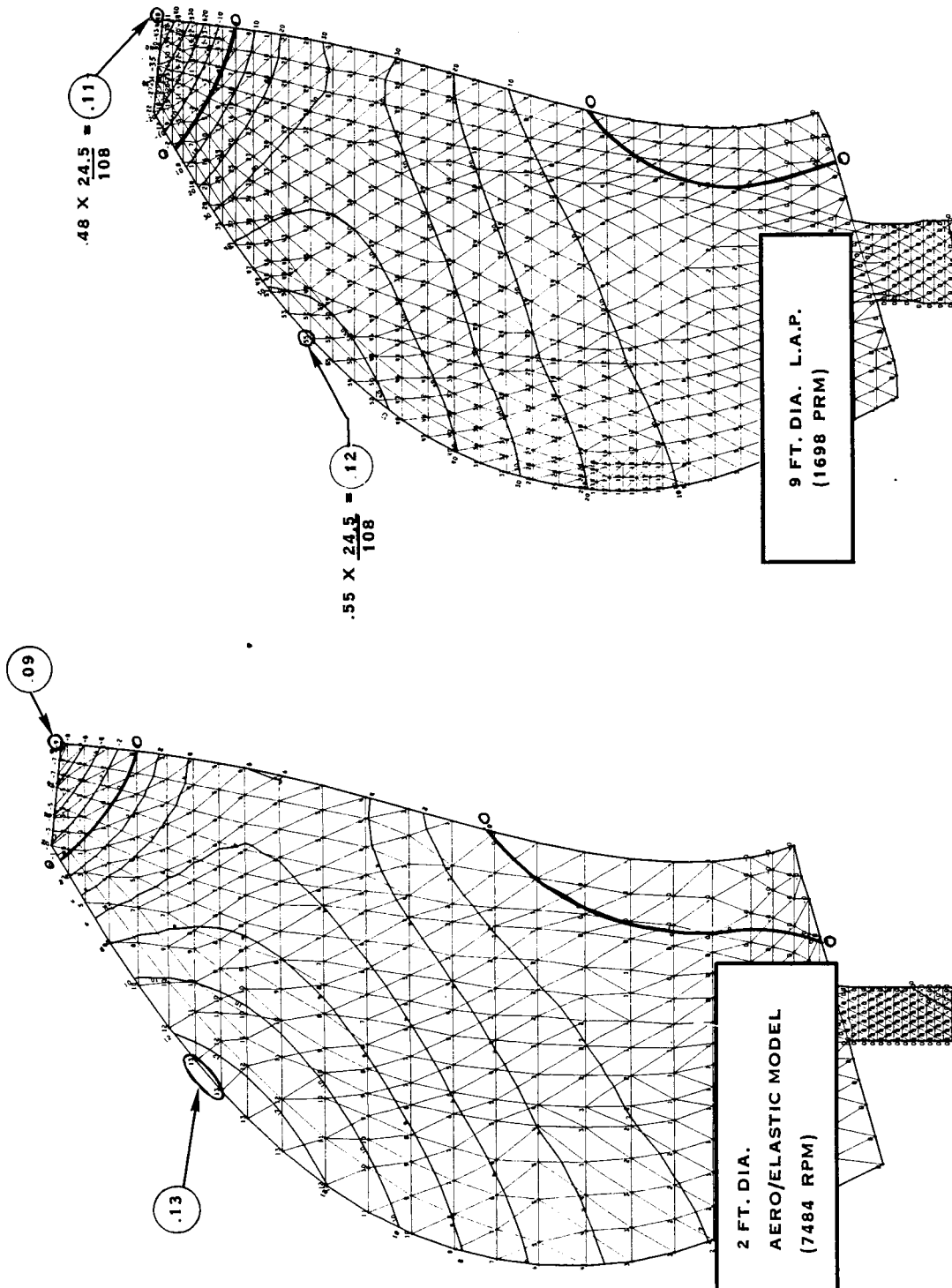


FIGURE 6-6. DEFLECTION CONTOUR PLOTS
35000 FT. ALTITUDE
CRUISE CONDITION (1 = .01 IN)

ORIGINAL PAGE IS
OF POOR QUALITY

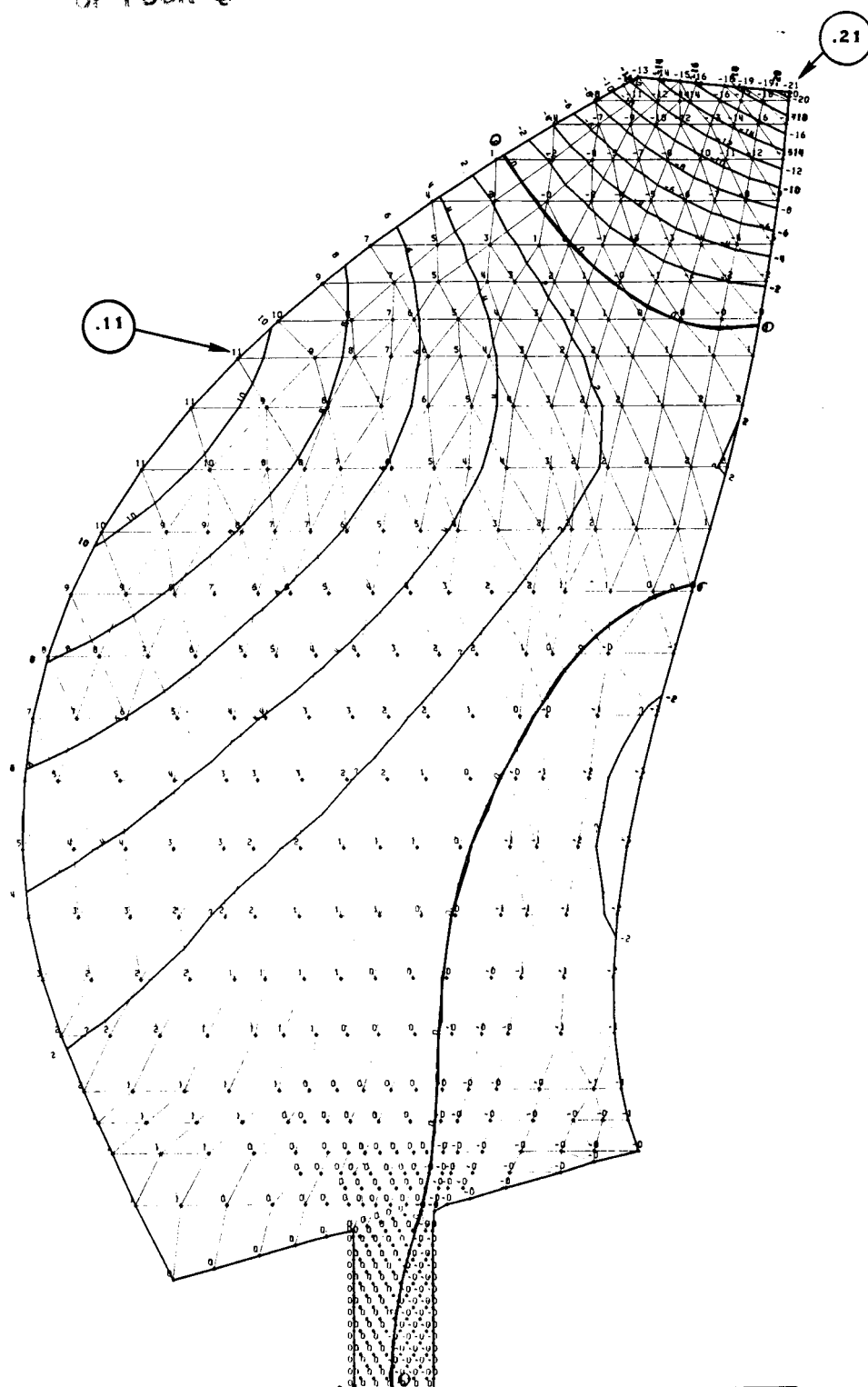


FIGURE 6-7. DEFLECTION CONTOUR PLOT
8x6 WIND TUNNEL CONDITION
8622 RPM (1=.01 IN)

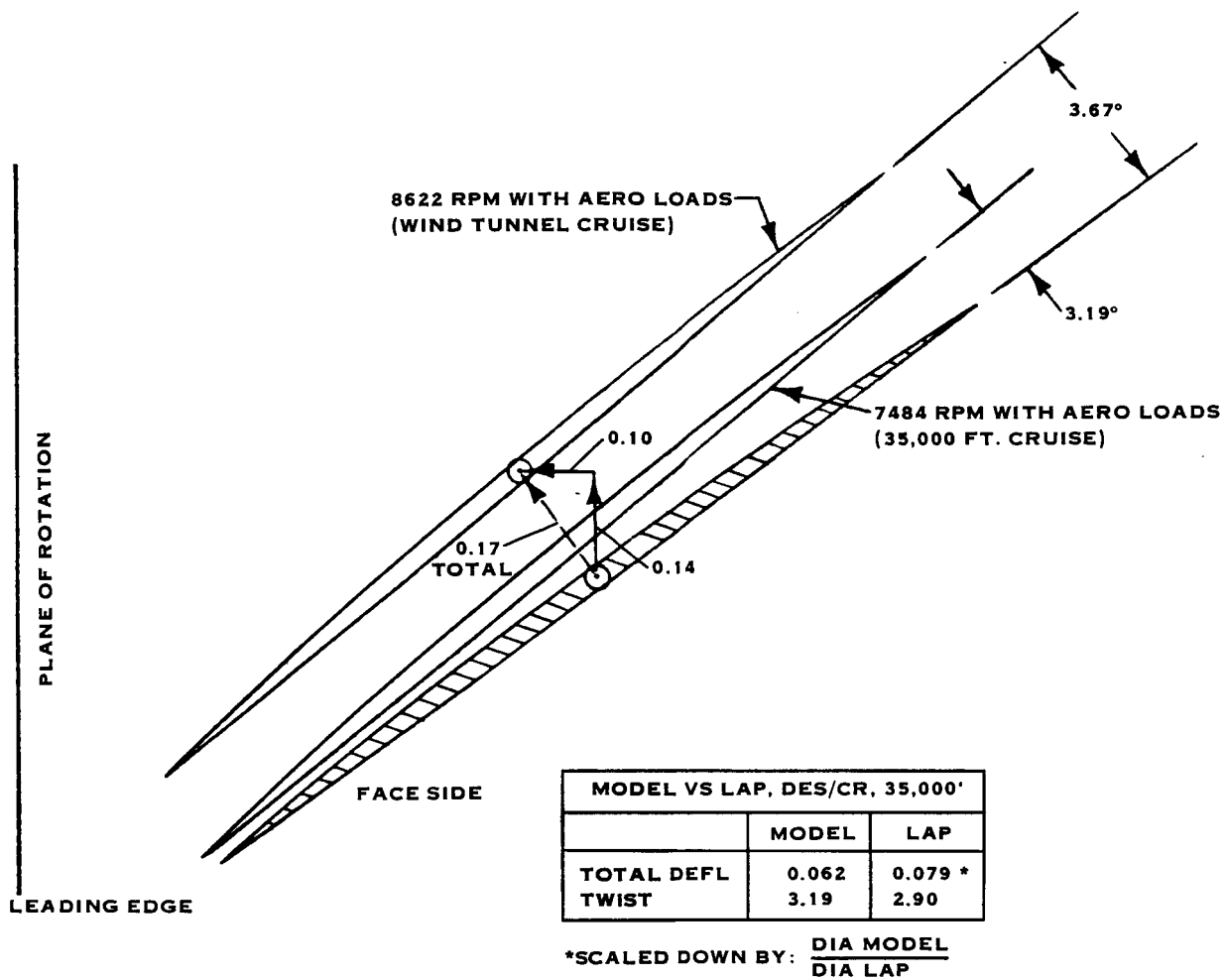


FIGURE 6-8. BLADE TIP DEFLECTIONS

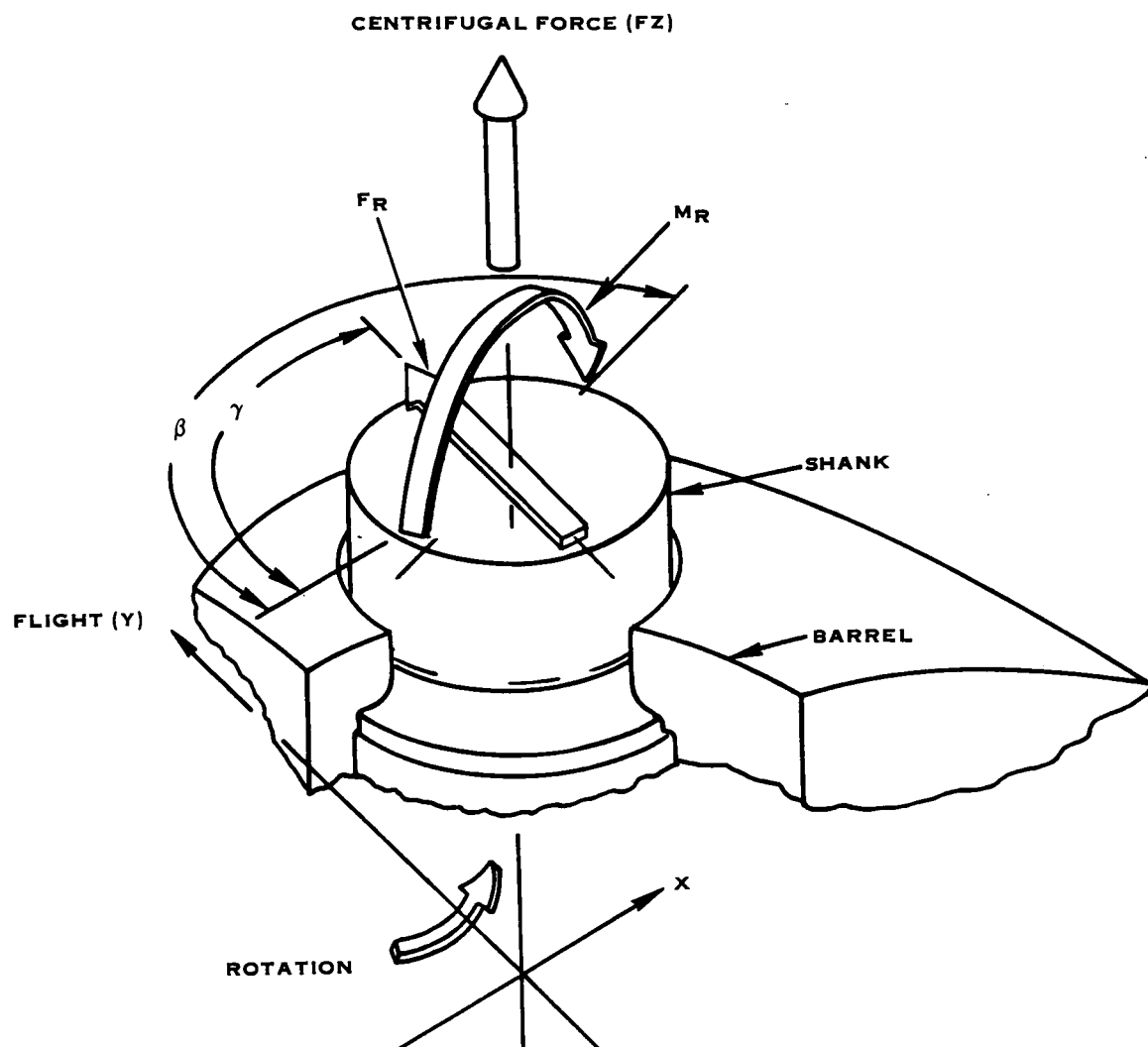


FIGURE 6-9. DIRECTIONS OF APPLIED BLADE LOADS AND MOMENTS

ORIGINAL PAGE IS
OF POOR QUALITY

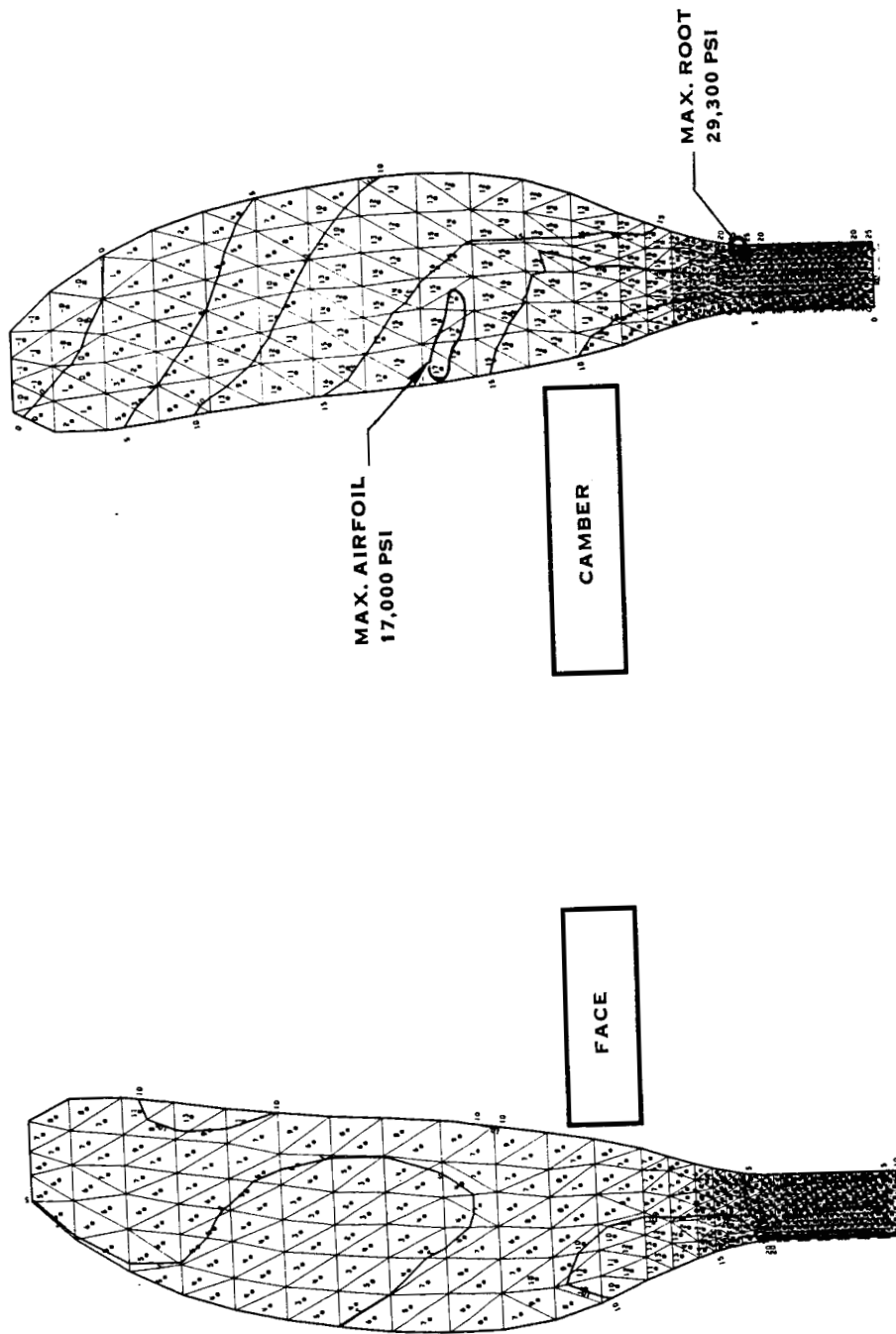


FIGURE 6-10. SPAR SURFACE RADIAL STRESS
35000 FT. ALTITUDE
CRUISE CONDITION (1 = 1000 PSI)

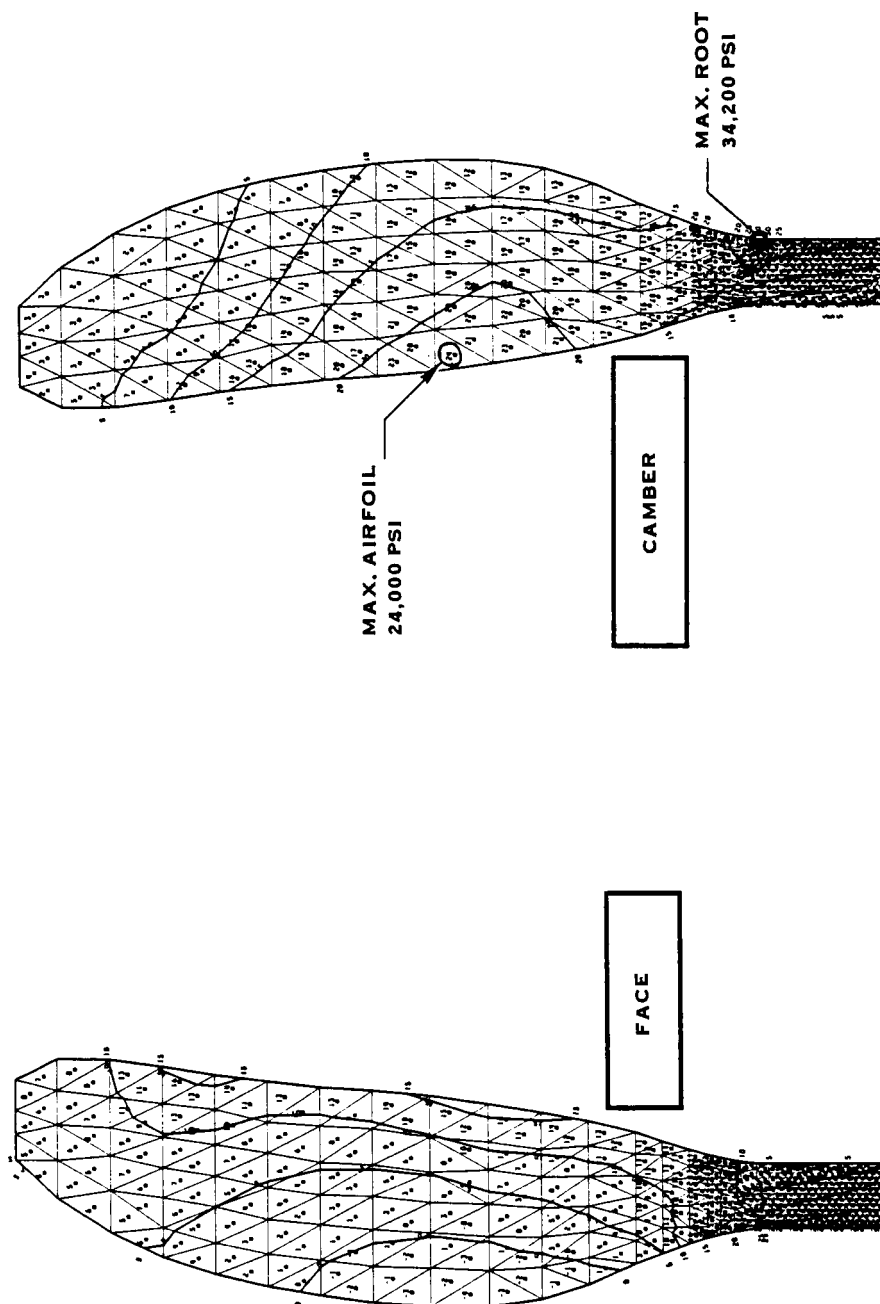


FIGURE 6-11. SPAR SURFACE RADIAL STRESS
WIND TUNNEL CONDITION
8622 RPM (1 = 1000 PSI)

ORIGINAL PAGE IS
OF POOR QUALITY

ORIGINAL PAGE IS
OF POOR QUALITY

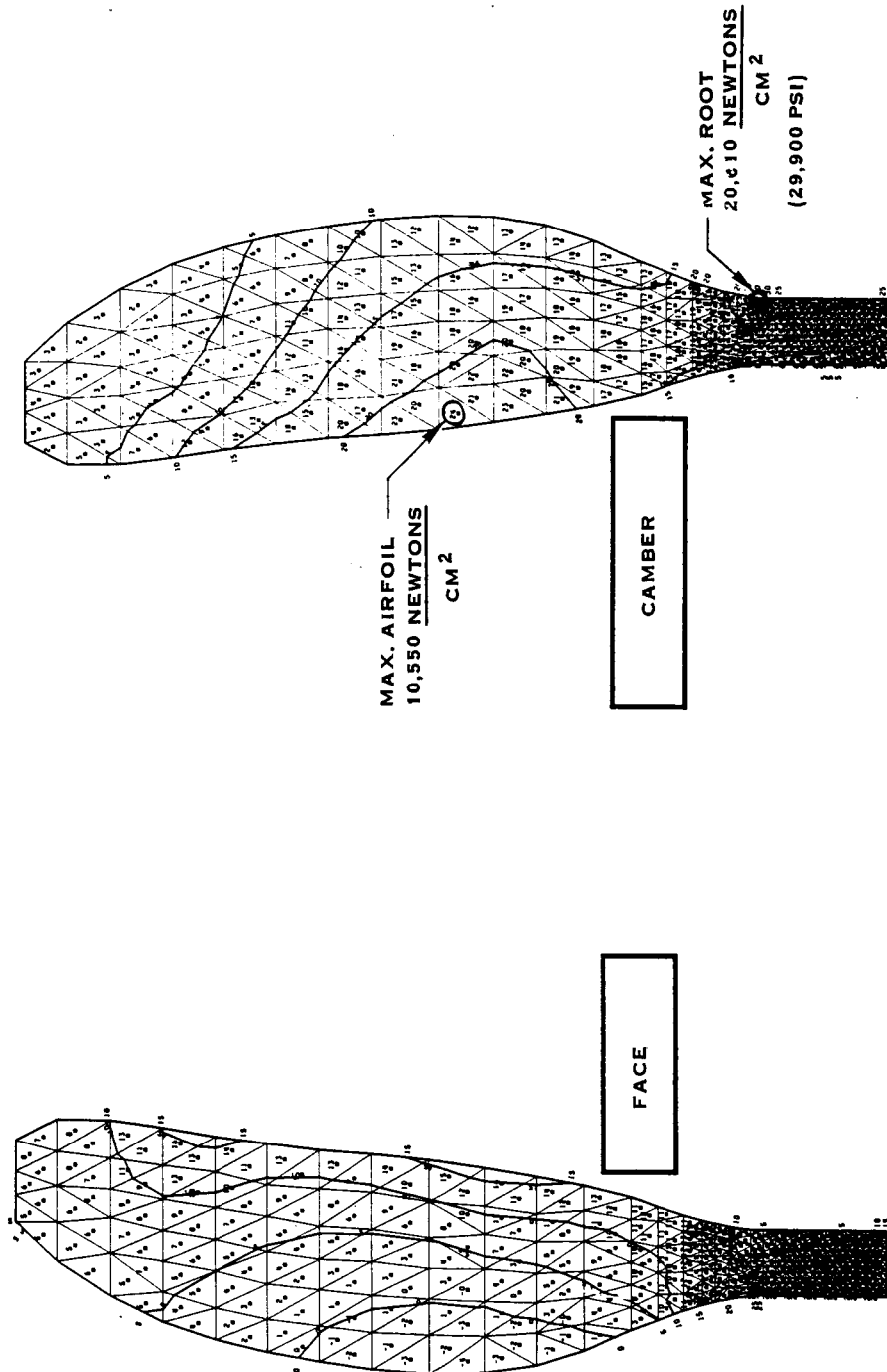


FIGURE 6-12: SPAR SURFACE RADIAL STRESS
TAKEOFF CLIMB CONDITION
(1 = 1000 PSI)

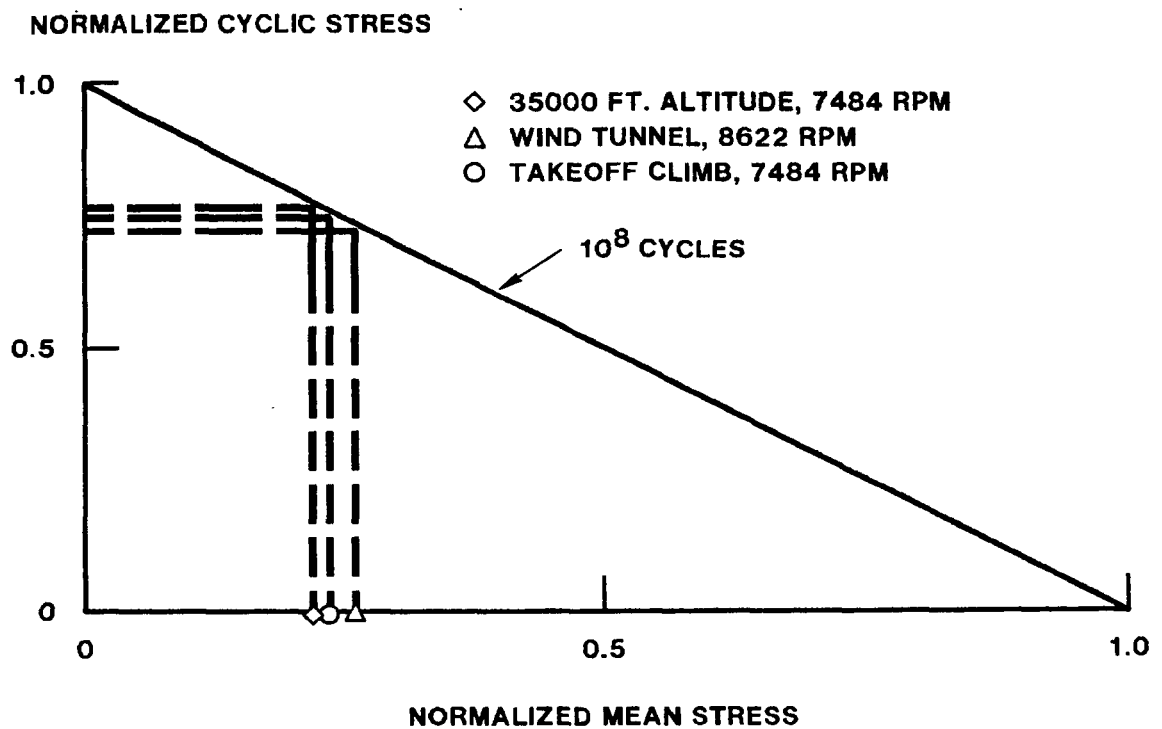


FIGURE 6-13. GOODMAN DIAGRAM SPAR TENSILE STRESS - SHANK AREA
TITANIUM (6A1-4V) GLASS BEAD PEENED

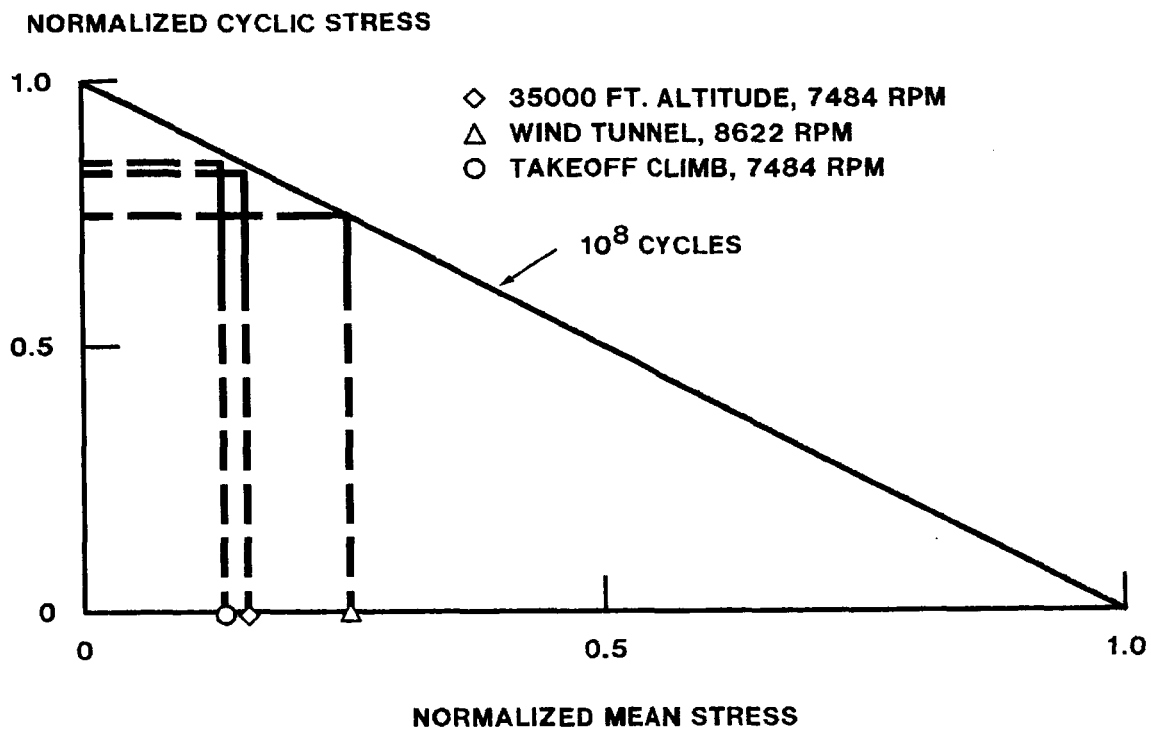


FIGURE 6-14. GOODMAN DIAGRAM SPAR TENSILE STRESS -
AIRFOIL AREA TITANIUM (6A1-4V) UNPEENED

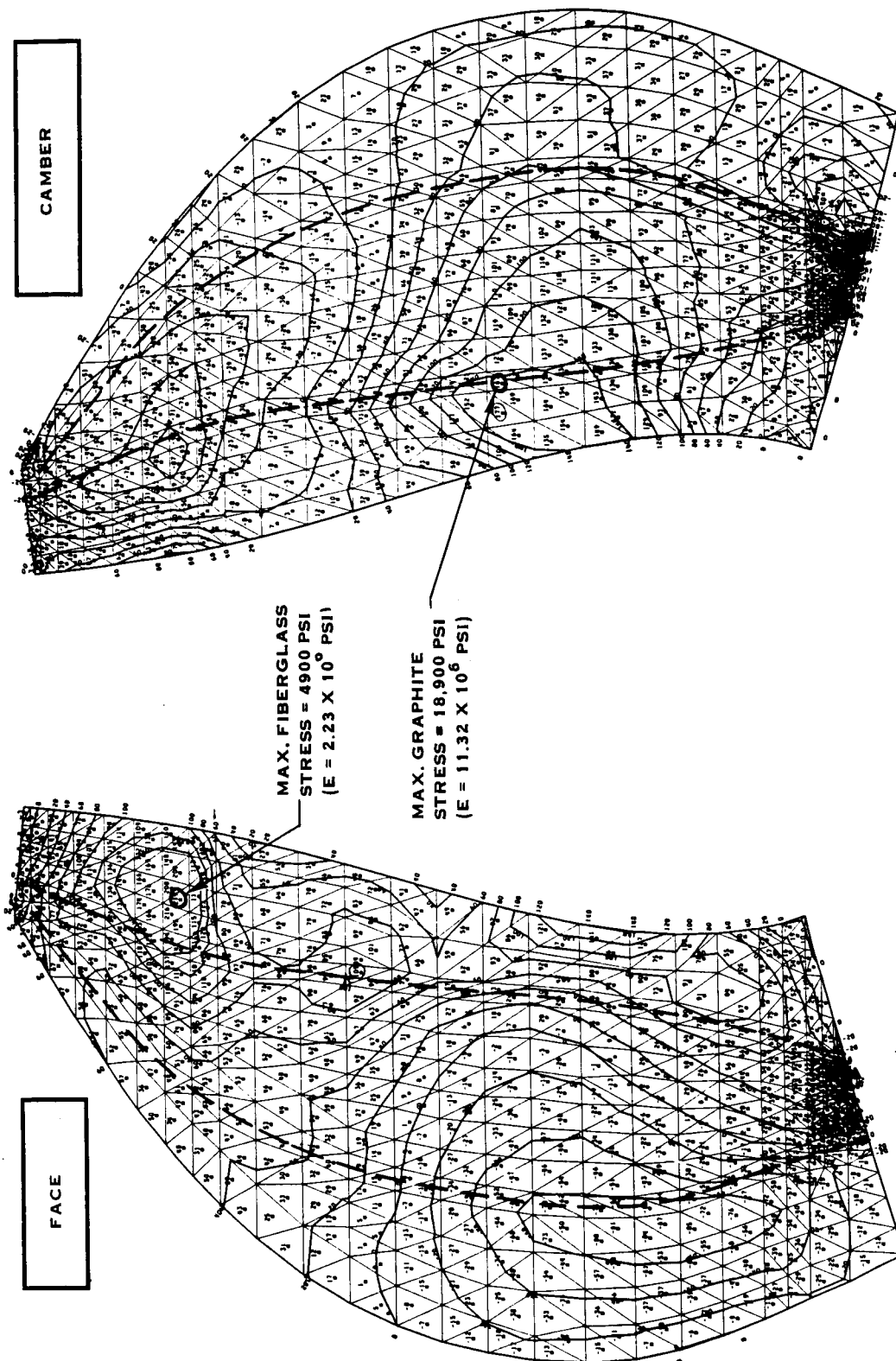


FIGURE 6-15. SHELL SURFACE RADIAL STRAIN
35000 FT. ALTITUDE
CRUISE CONDITION (100 = .001 IN/IN)

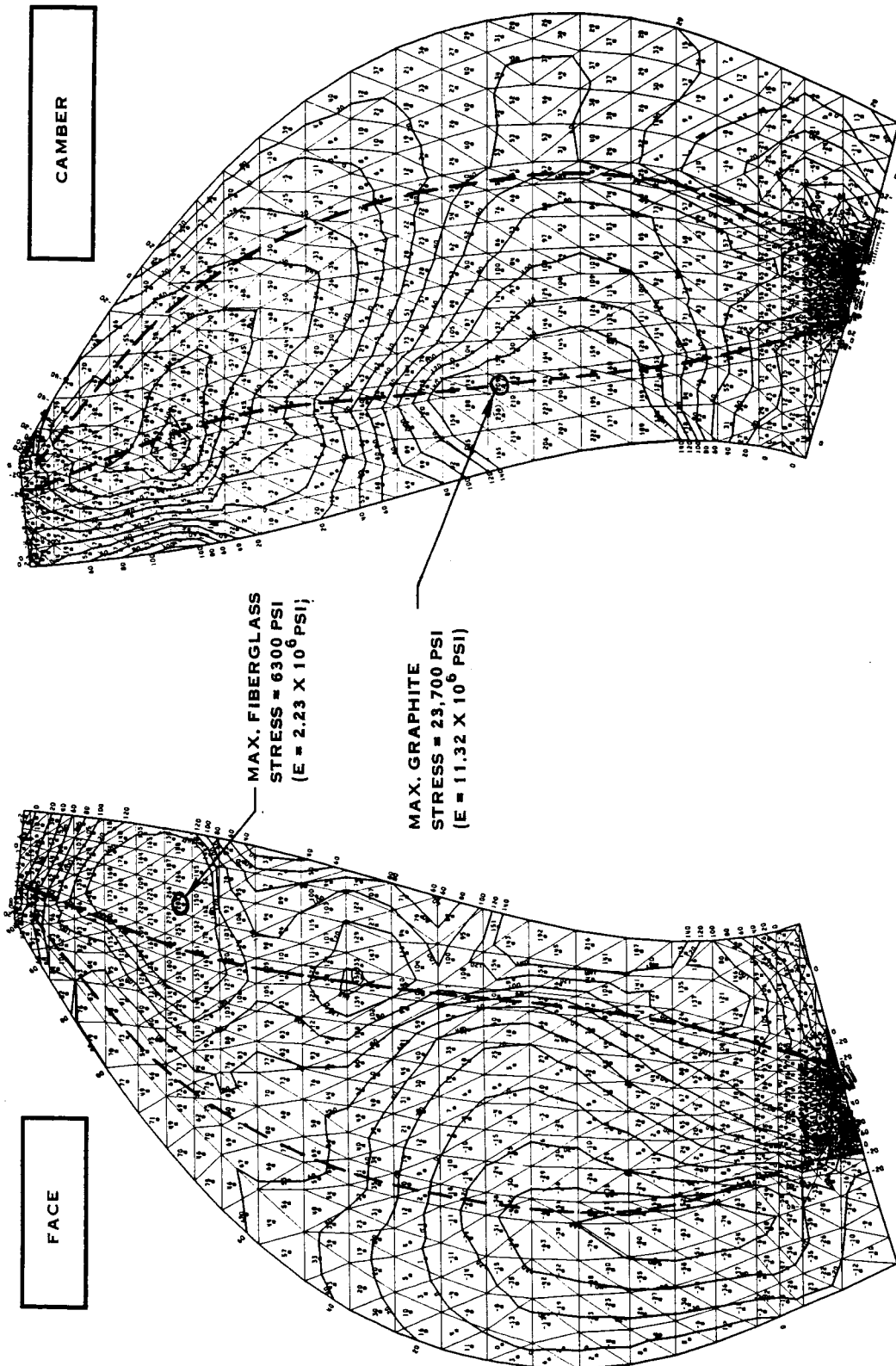


FIGURE 6-16. SHELL SURFACE RADIAL STRAIN
WIND TUNNEL -- CRUISE CONDITION
(100 = .001 IN/IN)

ORIGINAL PAGE IS
OF POOR QUALITY

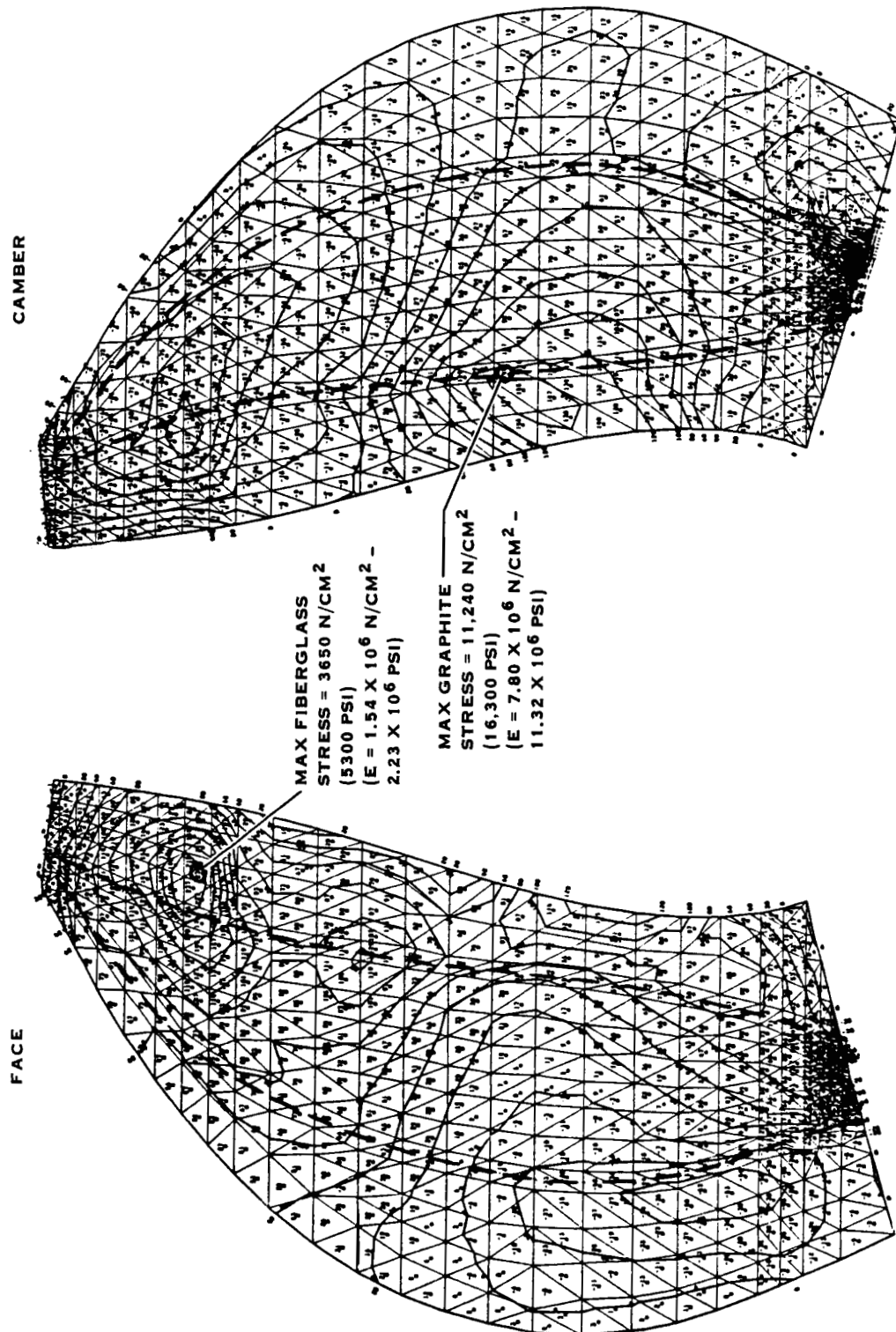


FIGURE 6-17. SHELL SURFACE RADIAL STRAIN - TAKEOFF CLIMB CONDITION
(100 = 0.001 IN/IN)

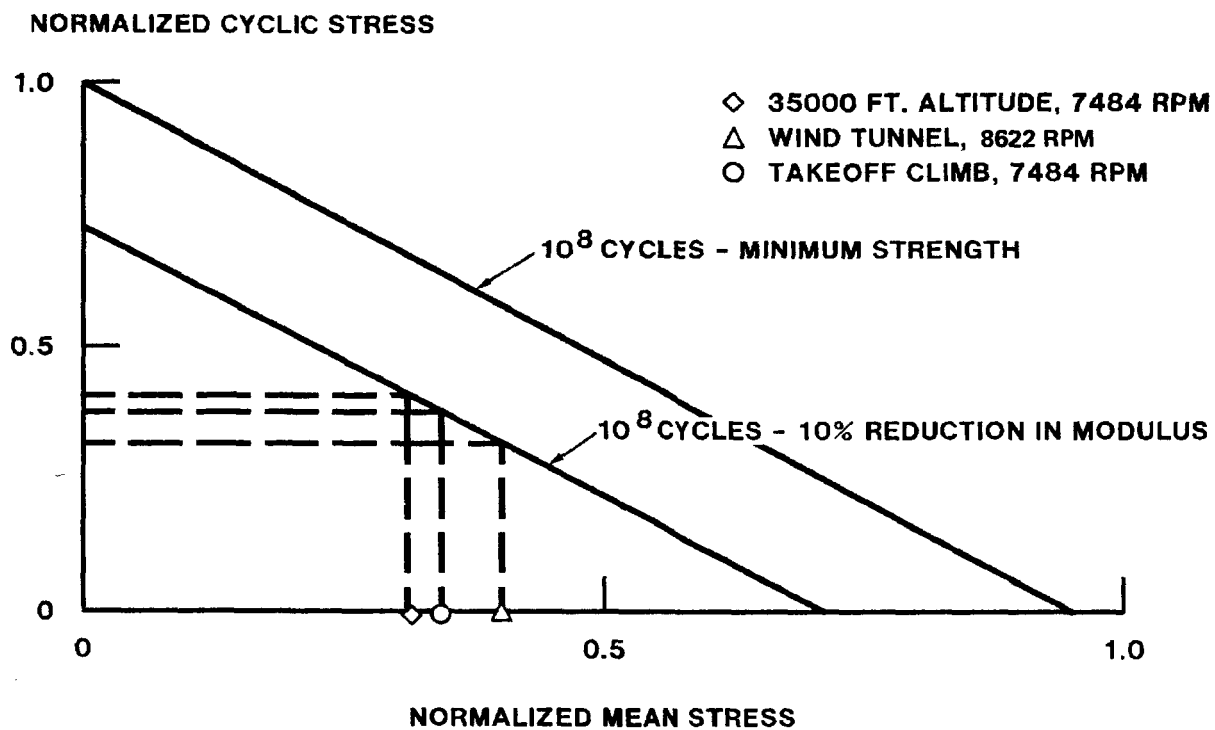


FIGURE 6-18. GOODMAN DIAGRAM SHELL TENSILE STRESS
FIBERGLASS CLOTH -25°, + 65°

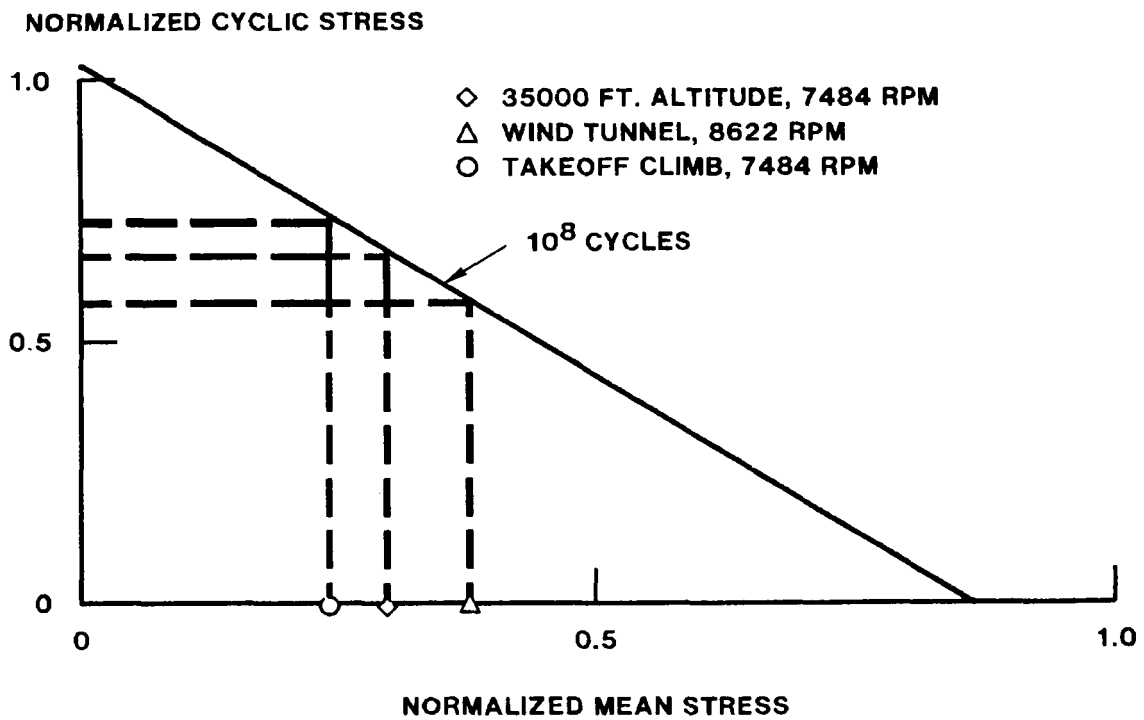


FIGURE 6-19. GOODMAN DIAGRAM SHELL TENSILE STRESS GRAPHITE 0°, 30°

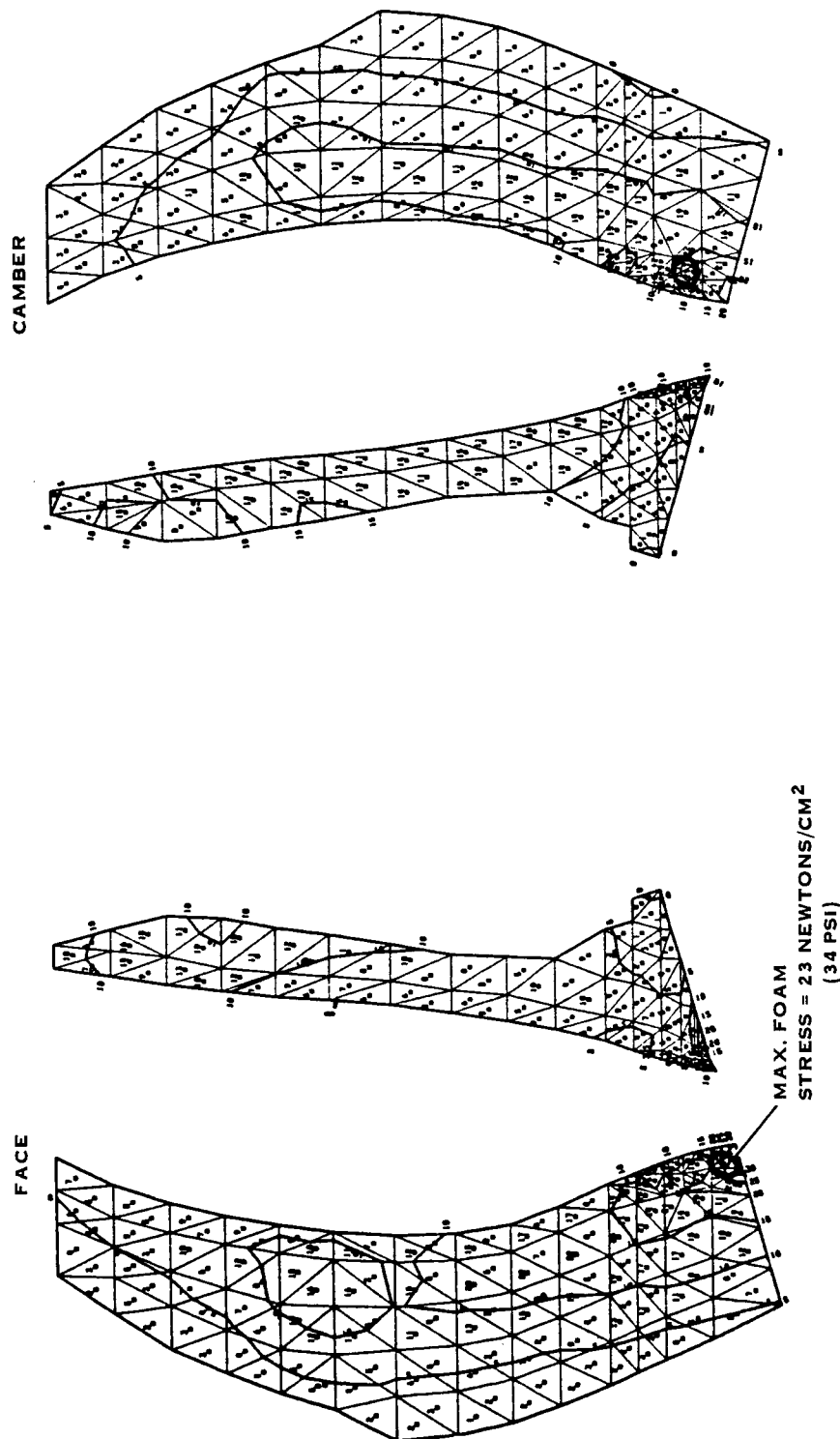


FIGURE 6-20. FOAM SURFACE EFFECTIVE STRESS
10,668 M (35,000 FT) ALTITUDE - CRUISE CONDITION (1 = 1 PSI)

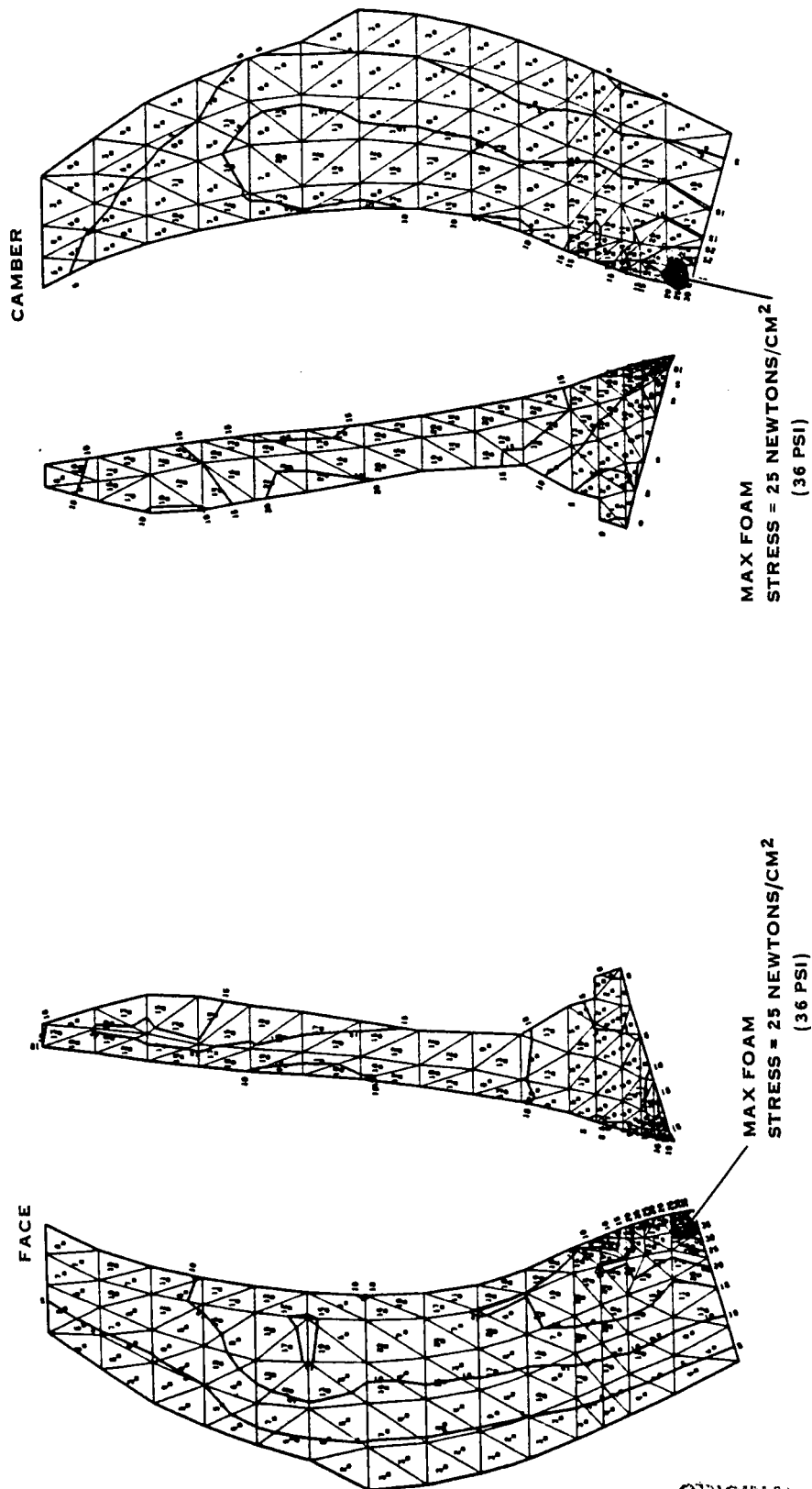


FIGURE 6-21. FOAM SURFACE EFFECTIVE STRESS
WIND TUNNEL - CRUISE CONDITION (1 = 1 PSI)

ORIGINAL PAGE IS
OF POOR QUALITY

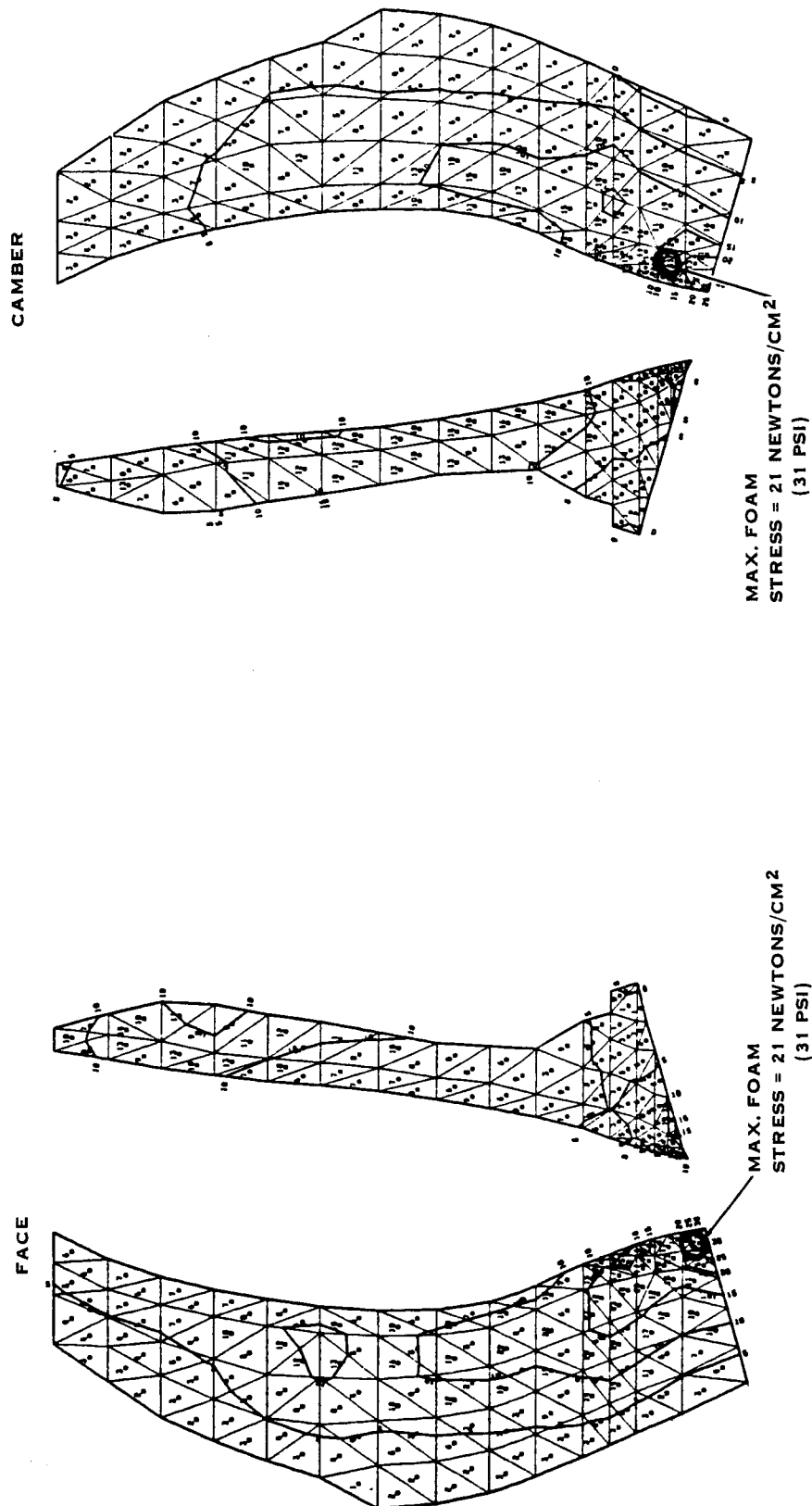


FIGURE 6-22. FOAM SURFACE EFFECTIVE STRESS
TAKEOFF CLIMB CONDITION (1= 1 PSI)

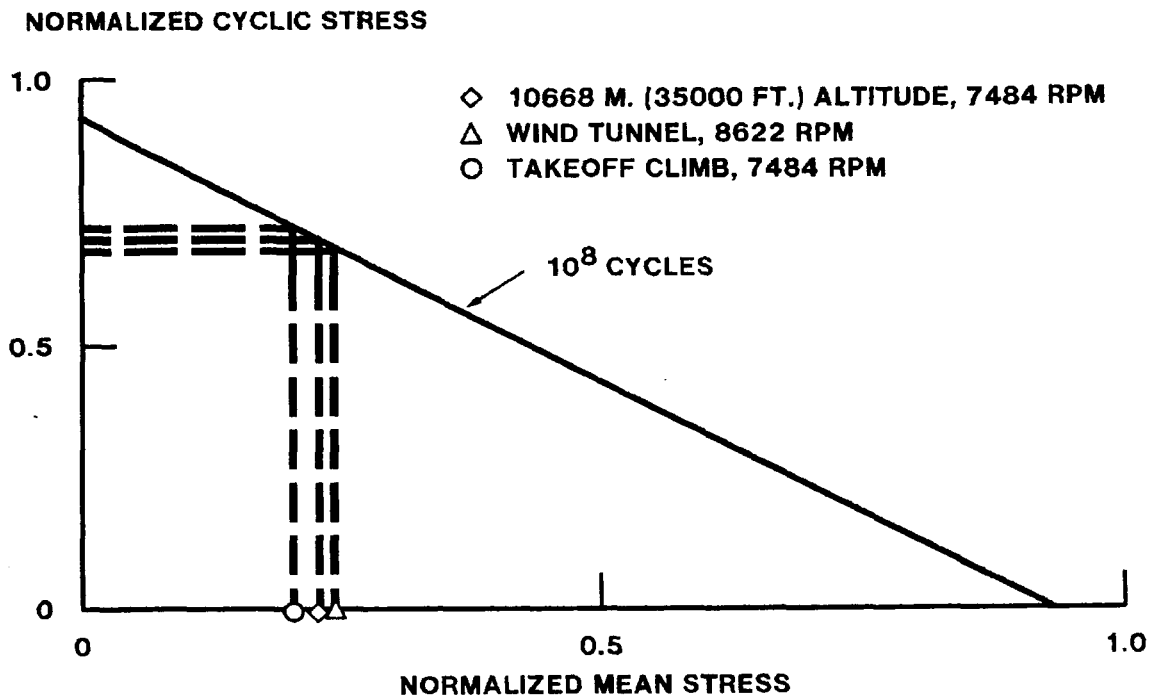


FIGURE 6-23. GOODMAN DIAGRAM FOAM TENSILE STRESS
0.128 GMS/CM³ (8 LBS/FT³) FOAM

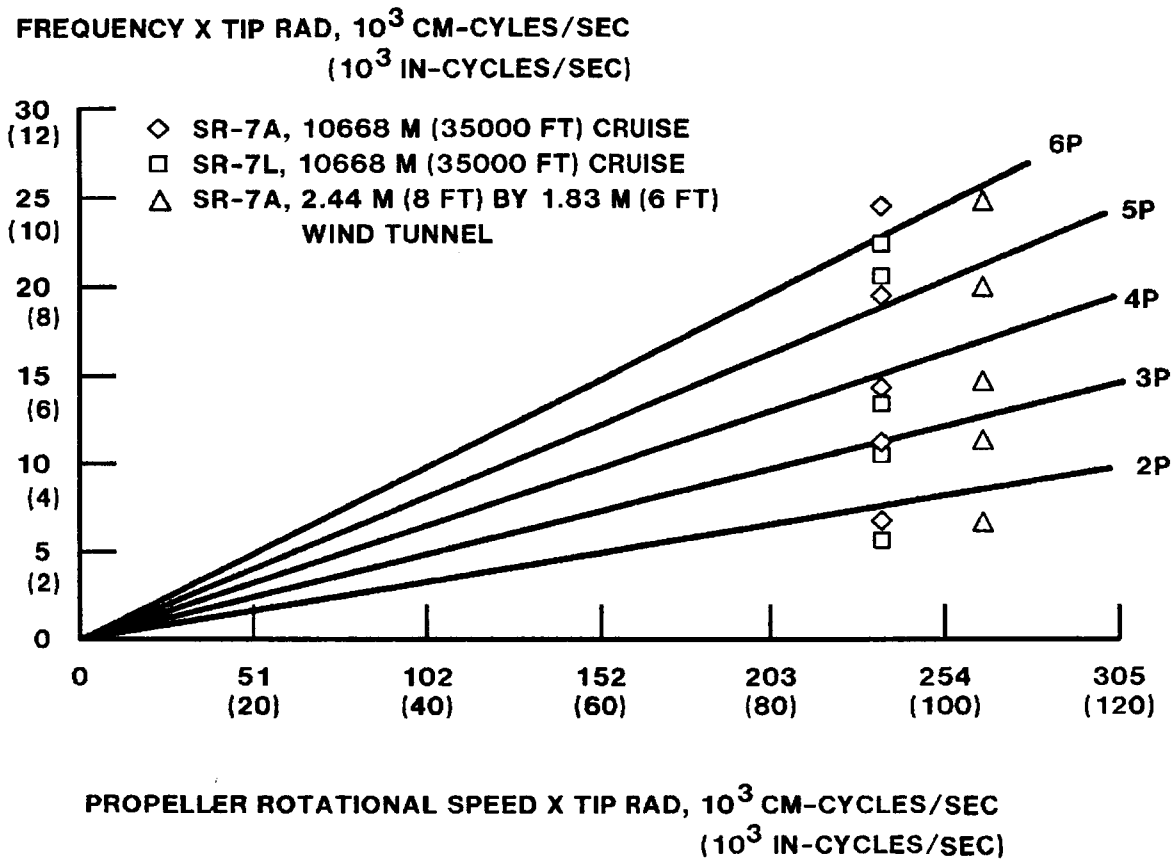


FIGURE 6-24. MODIFIED CAMPBELL DIAGRAM

FREQUENCY, HZ

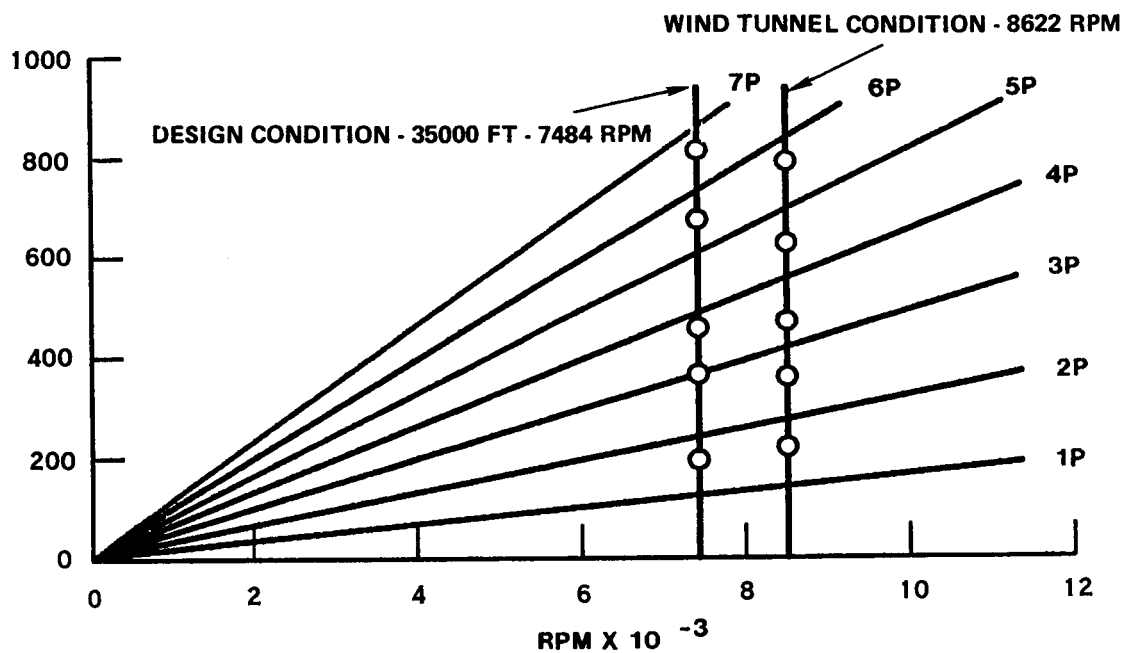


FIGURE 6-25. CAMPBELL DIAGRAM AEROELASTIC MODEL
 $\beta_{3/4} = 57.57^\circ$

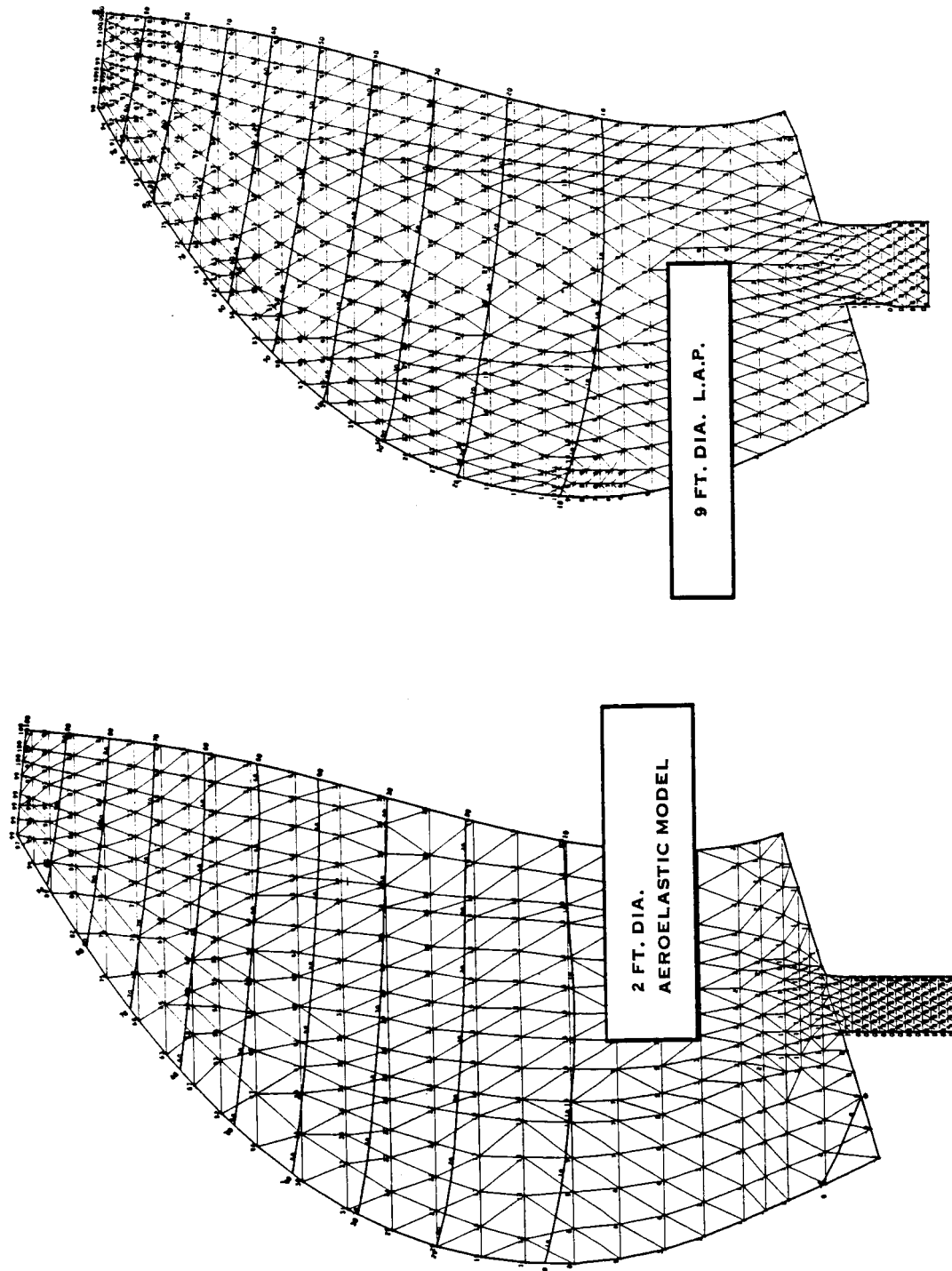


FIGURE 6-26. VIBRATION MODE SHAPES
35000 FT. ALTITUDE
CRUISE CONDITION - 1ST MODE

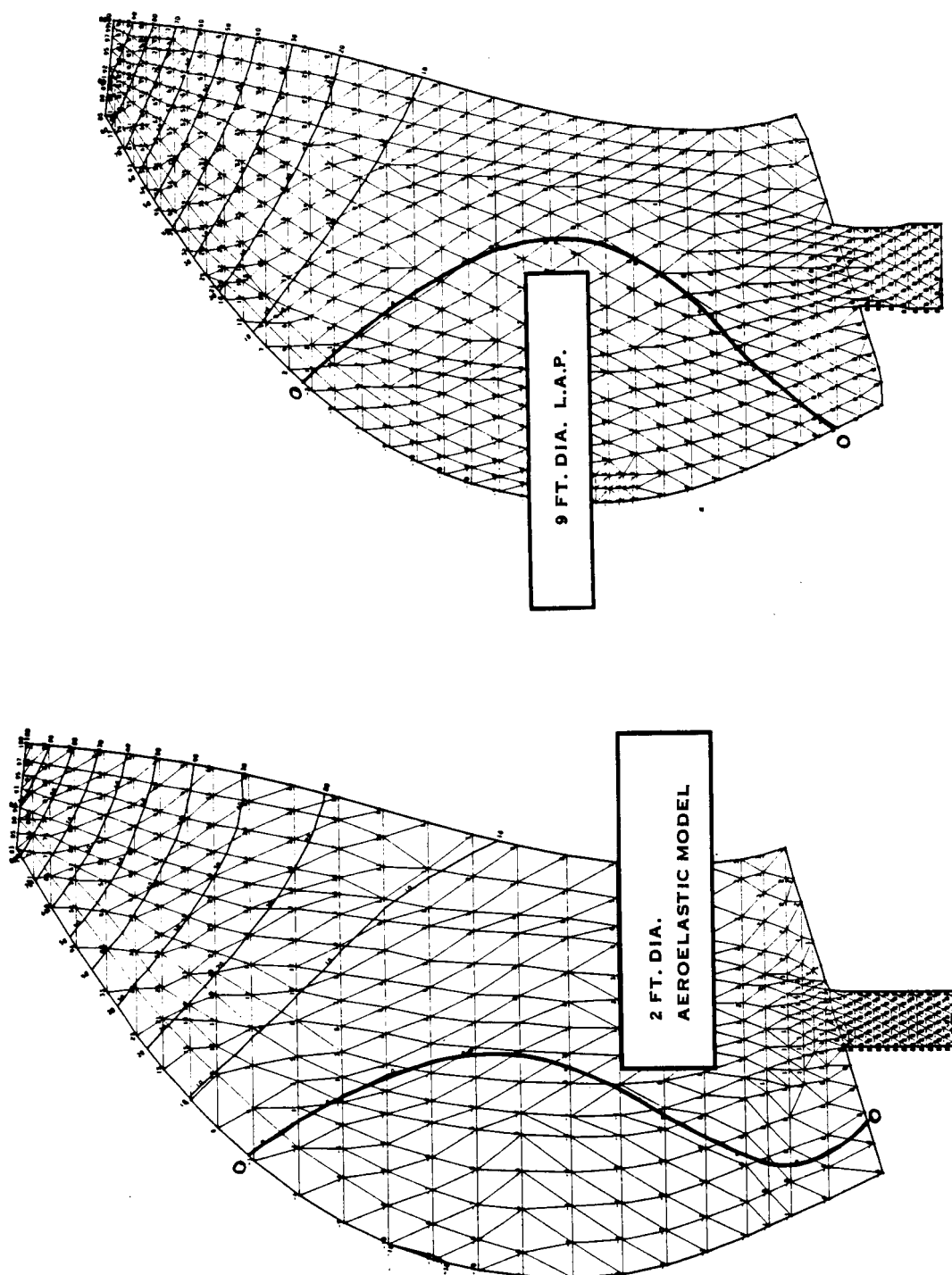


FIGURE 6-27. VIBRATION MODE SHAPES
35000 FT. ALTITUDE
CRUISE CONDITION - 2ND MODE

ORIGINAL PAGE IS
OF POOR QUALITY

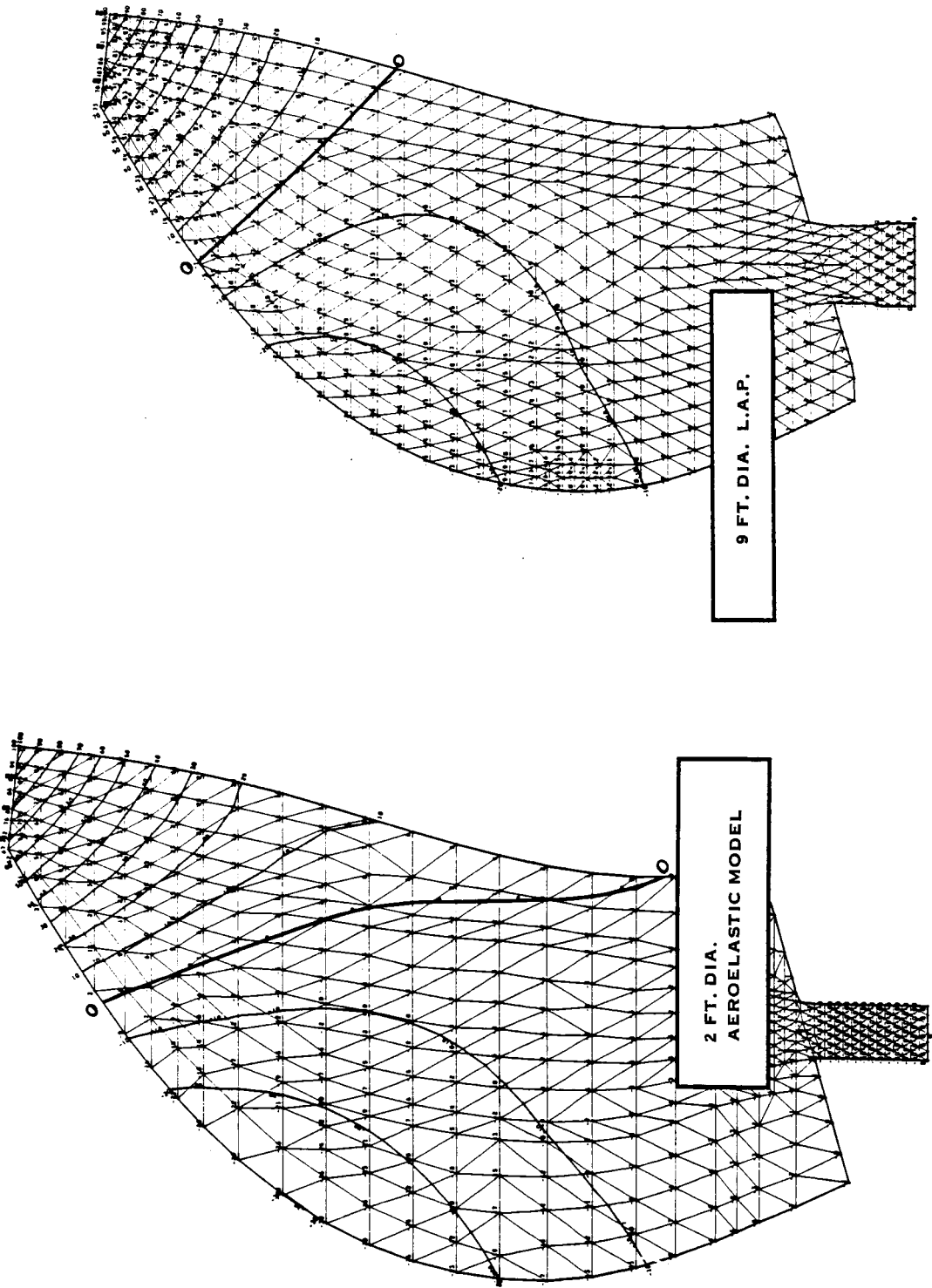


FIGURE 6-28. VIBRATION MODE SHAPES
35000 FT. ALTITUDE
CRUISE CONDITION - 3RD MODE

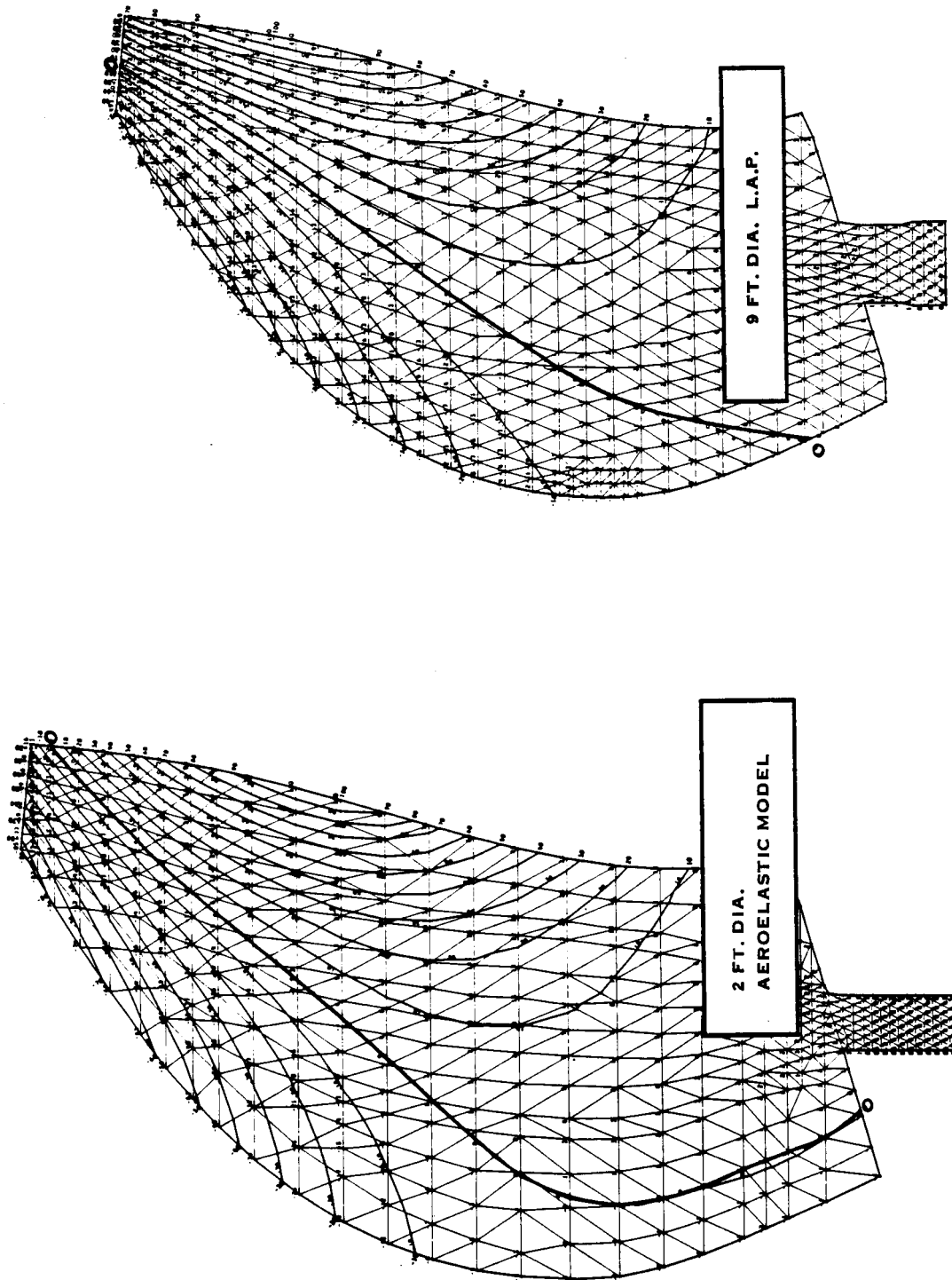


FIGURE 6-29. VIBRATION MODE SHAPES
35000 FT. ALTITUDE
CRUISE CONDITION - 4TH MODE

ORIGINAL PAGE IS
OF POOR QUALITY

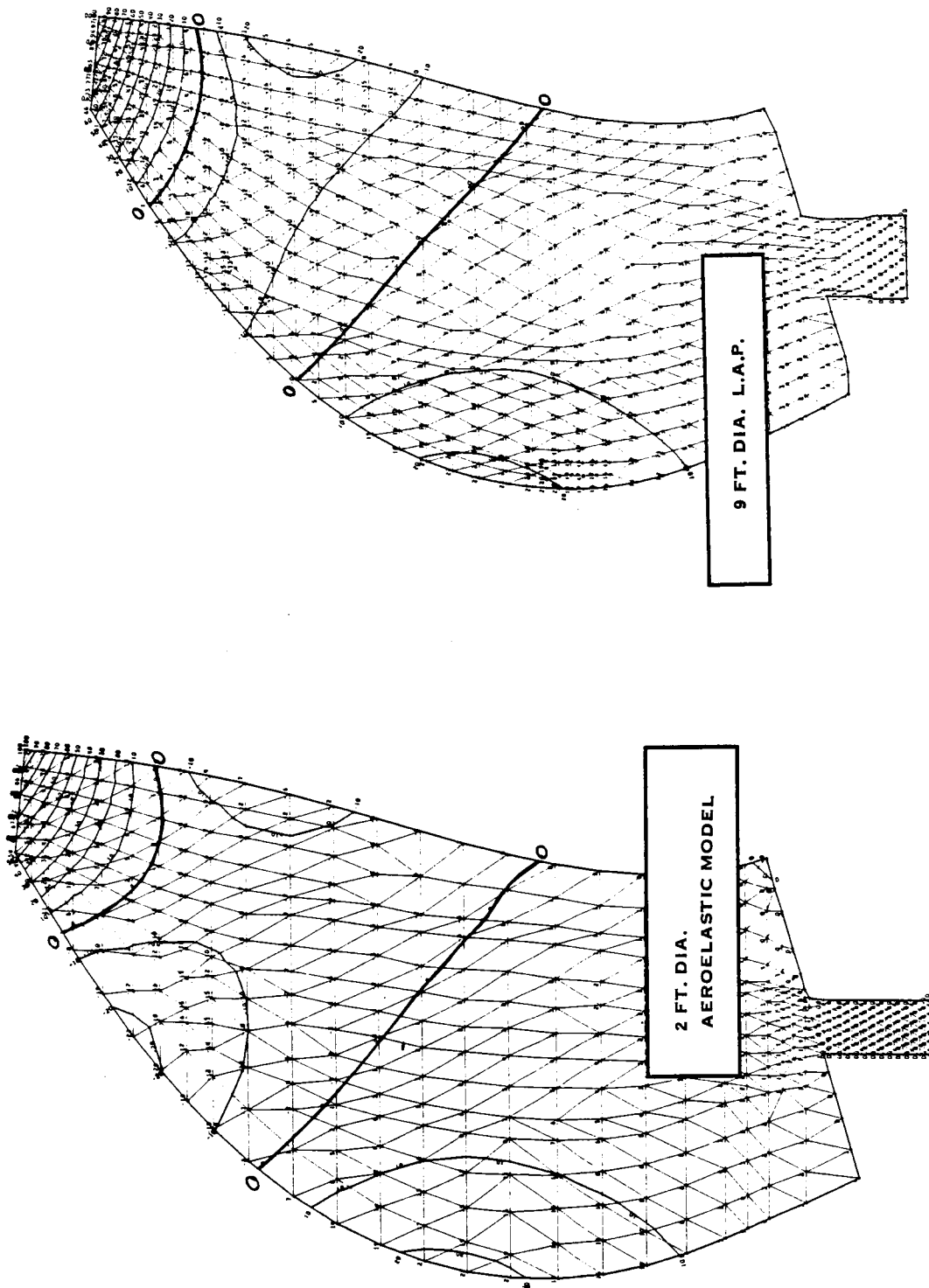


FIGURE 6-30. VIBRATION MODE SHAPES
35000 FT. ALTITUDE
CRUISE CONDITION - 5TH MODE

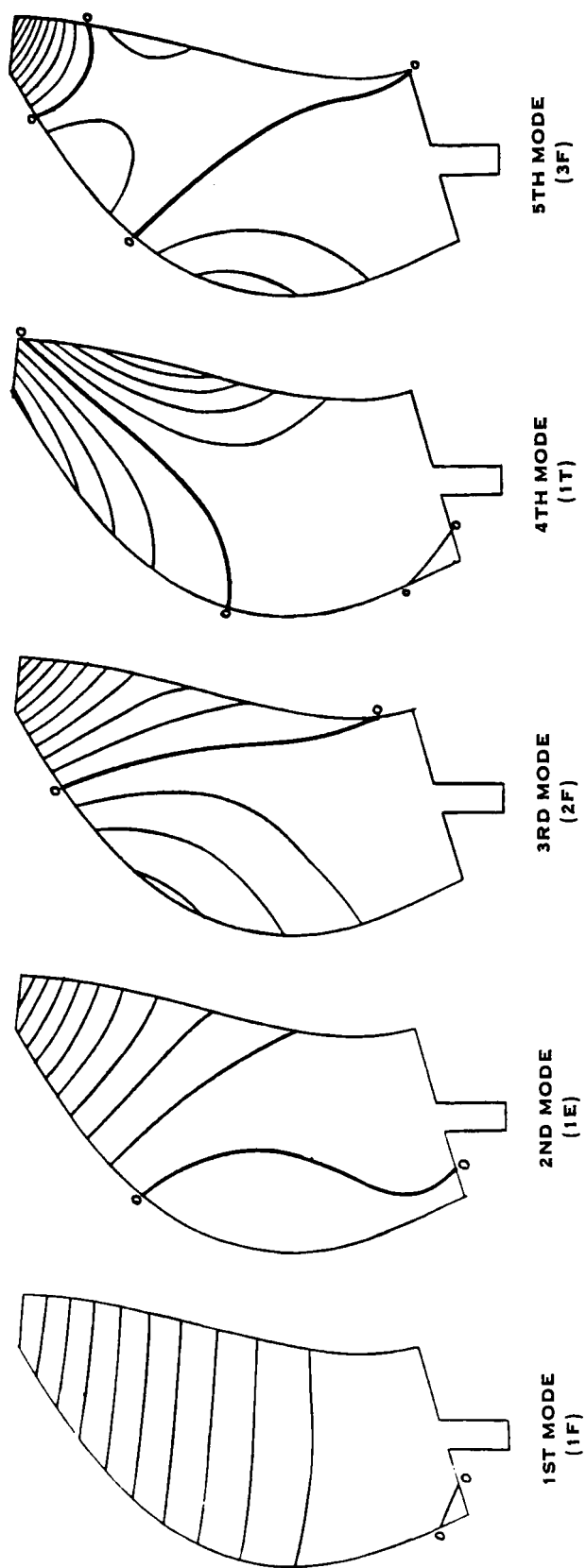


FIGURE 6-31. VIBRATION MODE SHAPES 8 X 6 WIND TUNNEL - CRUISE CONDITION

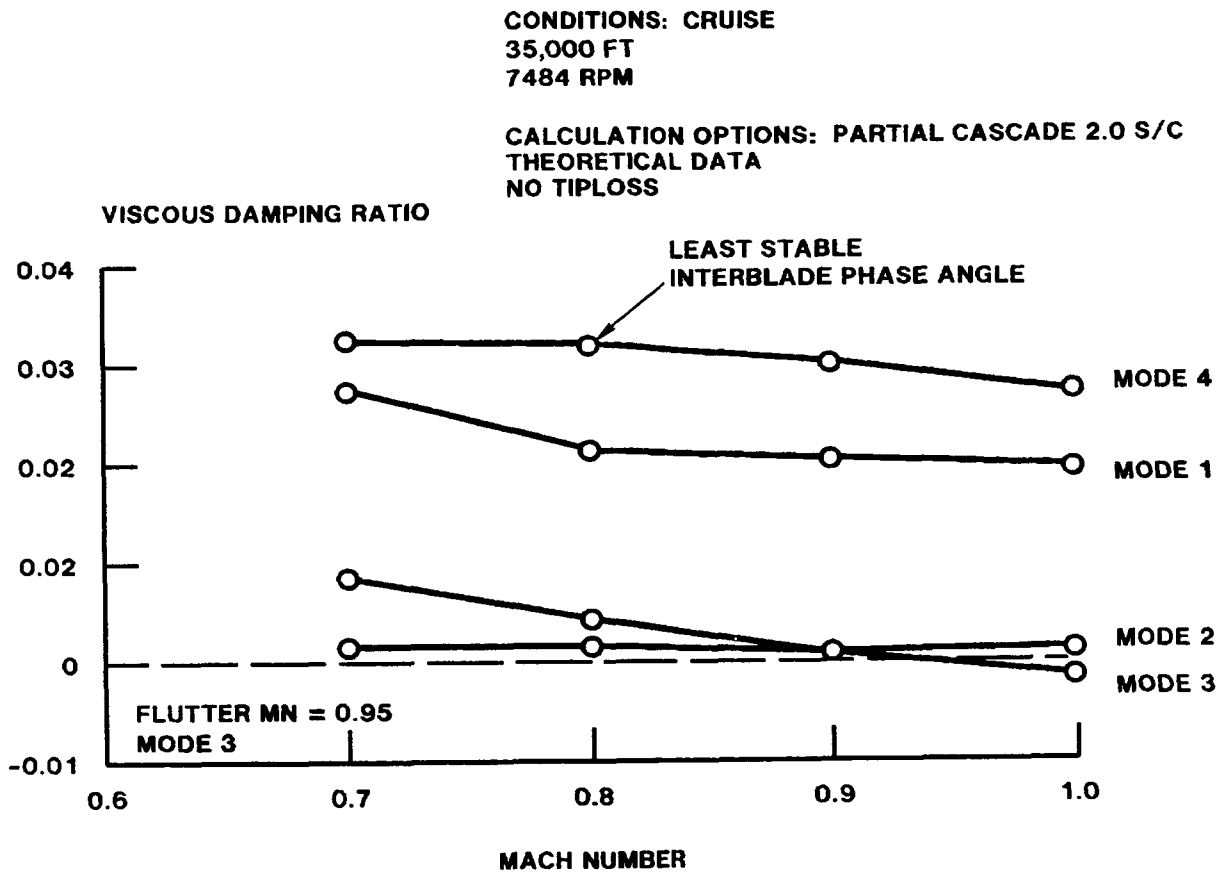


FIGURE 6-32. SR-7A AEROELASTIC MODEL STABILITY DESIGN CRUISE CONDITION

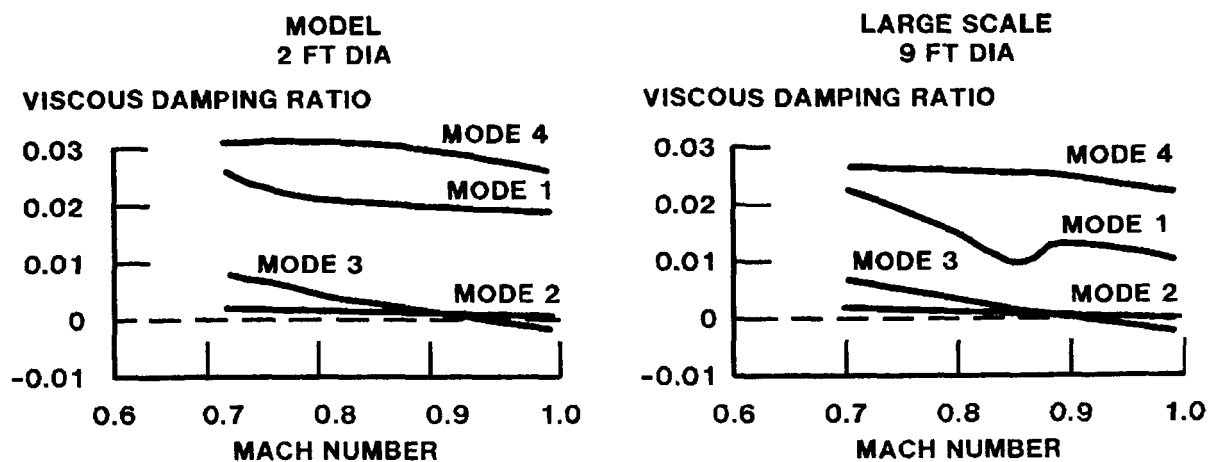


FIGURE 6-33. SR-7A AEROELASTIC MODEL STABILITY COMPARISON

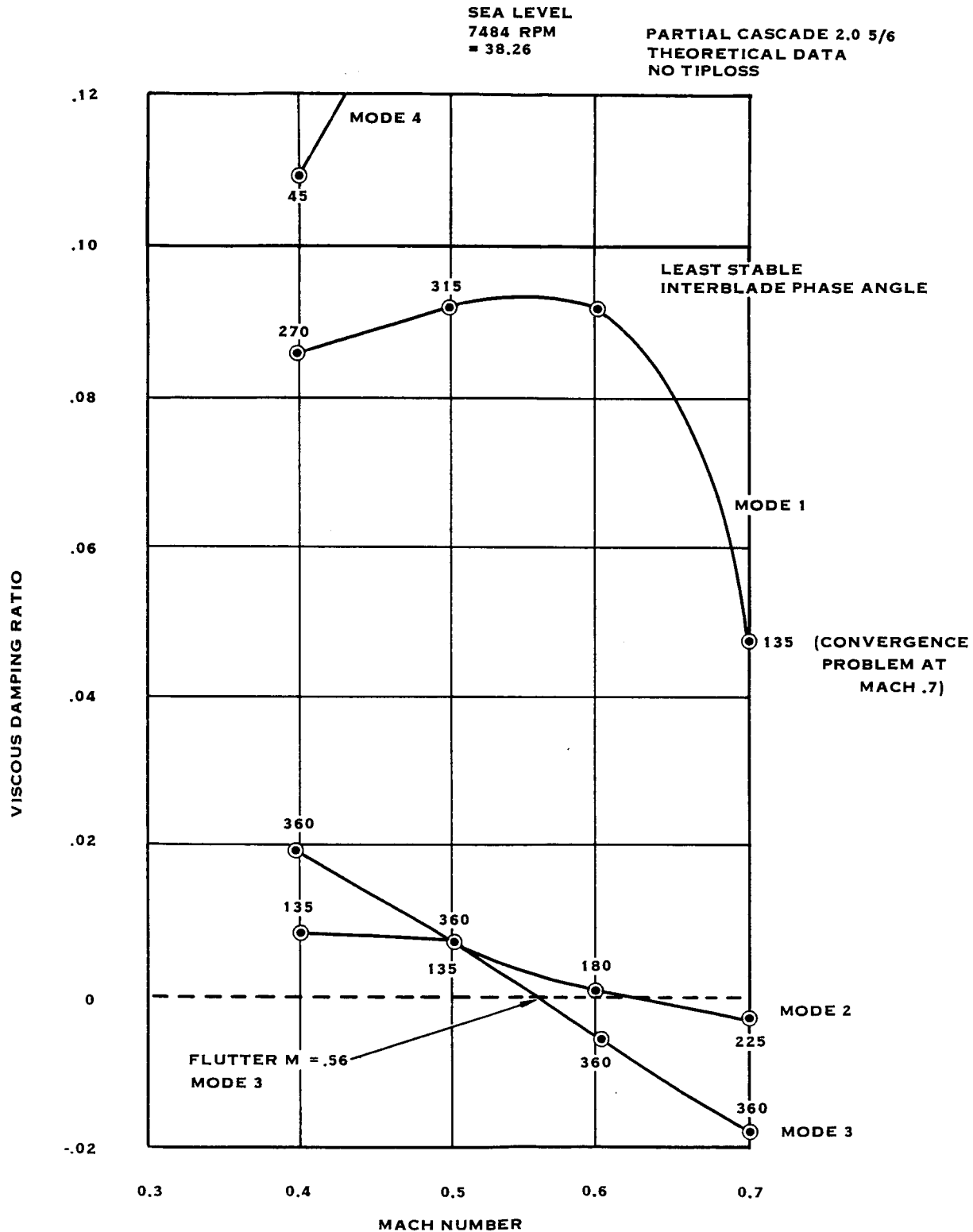


FIGURE 6-34. SR-7A AEROELASTIC MODEL STABILITY TAKE-OFF CLIMB CONDITION

NASA LEWIS 8 X 6 WIND TUNNEL SIMULATION

7520 FT ALTITUDE
8622 RPM

PARTIAL CASCADE 2.0 5/6
NO TIPLOSS
THEORETICAL DATA
(L.A.P. PROCEDURE)

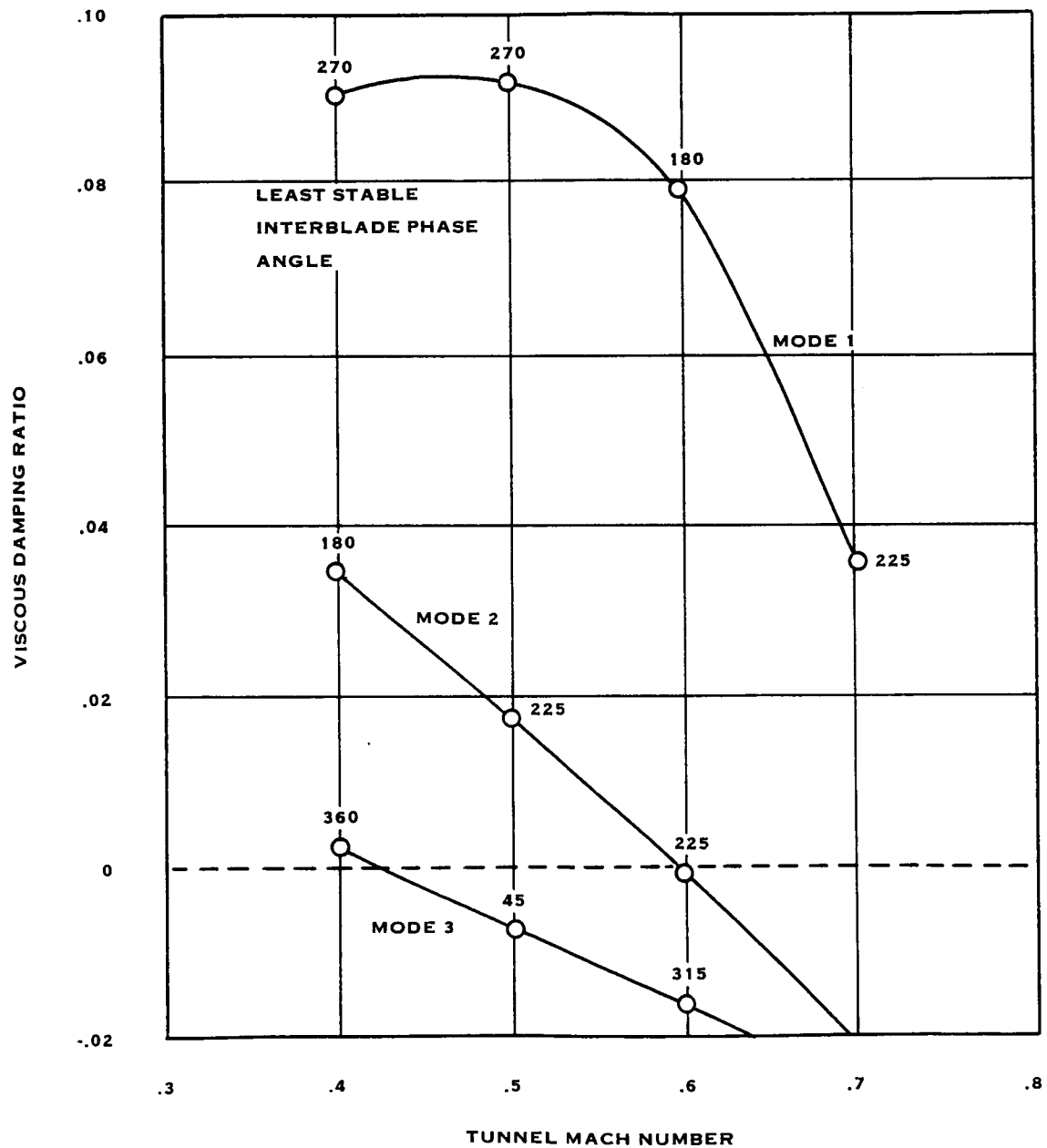


FIGURE 6-35. SR-7A AEROELASTIC MODEL STABILITY-WIND TUNNEL CONDITION

NASA LEWIS 8 X 6 WIND TUNNEL SIMULATION

7520 FT ALTITUDE
8622 RPM

PARTIAL CASCADE 2.0 5/6
TIP LOSS R/R = .9
EMPIRICAL DATA
(MODIFIED ANALYSIS)

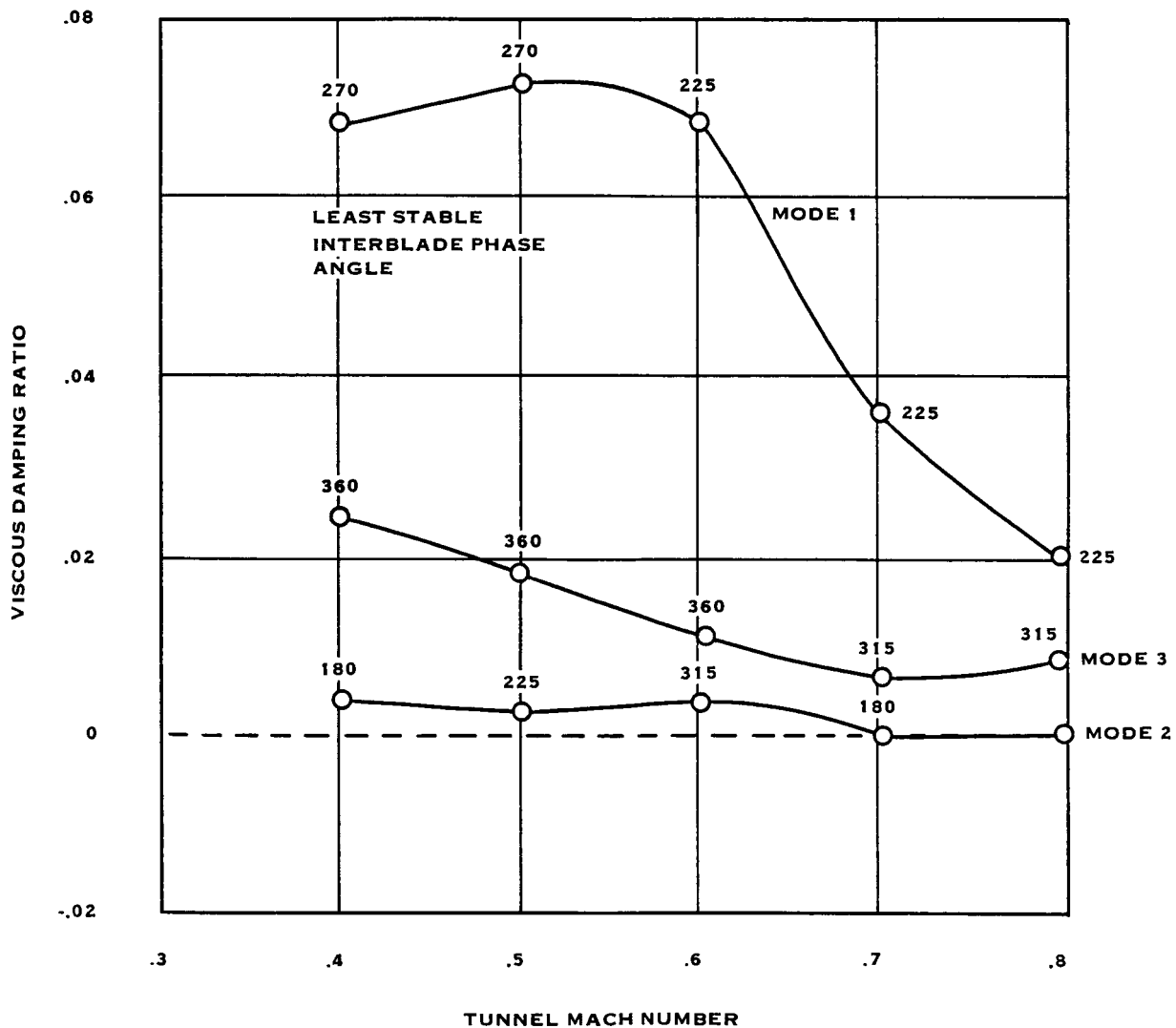


FIGURE 6-36. SR-7A AEROELASTIC MODEL STABILITY
WIND TUNNEL CONDITION MODIFIED ANALYSIS

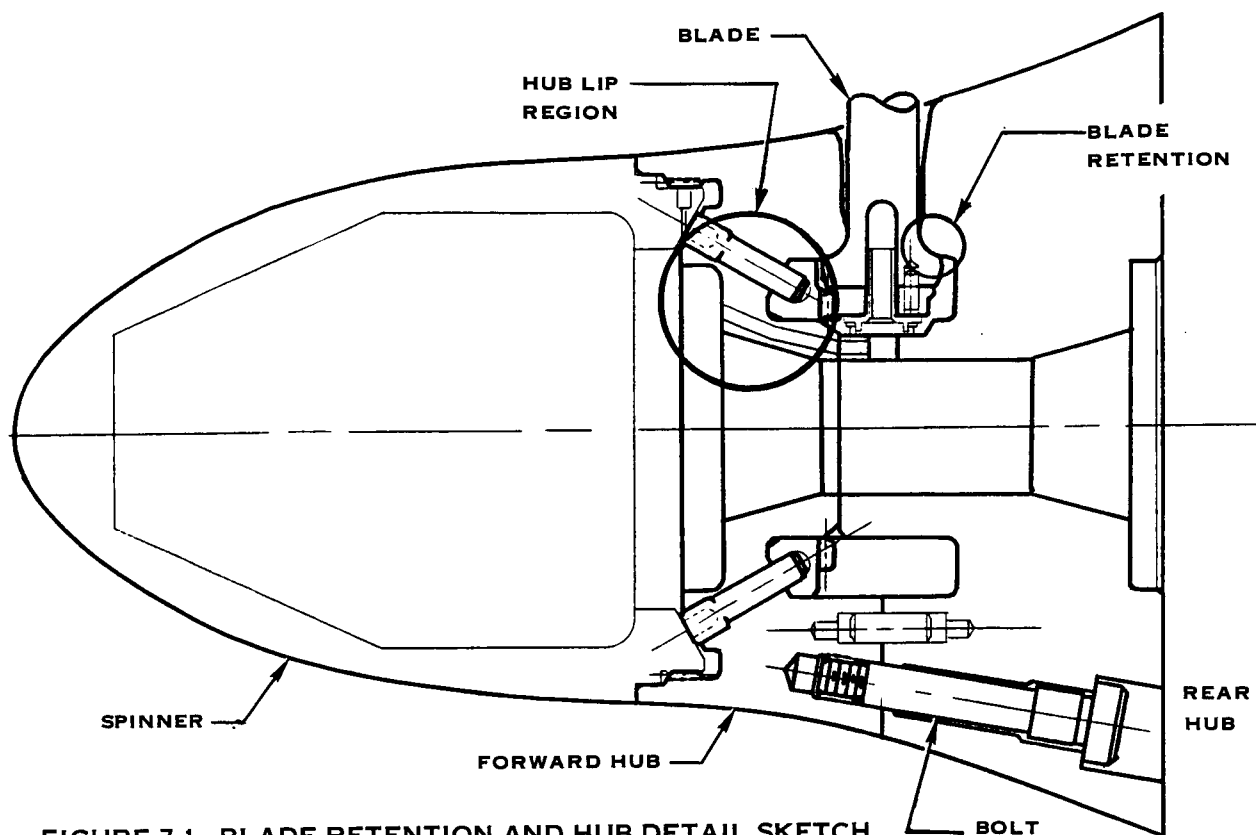


FIGURE 7-1. BLADE RETENTION AND HUB DETAIL SKETCH

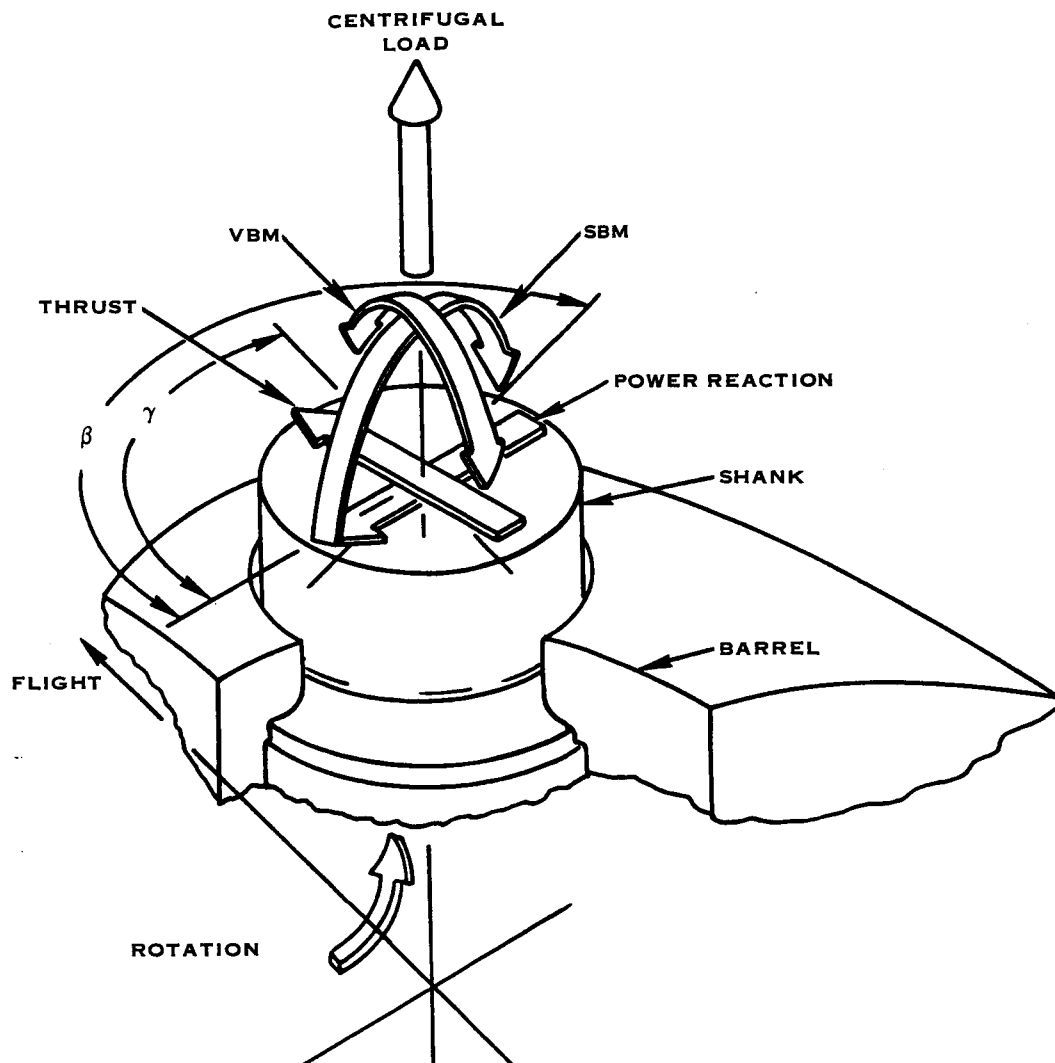
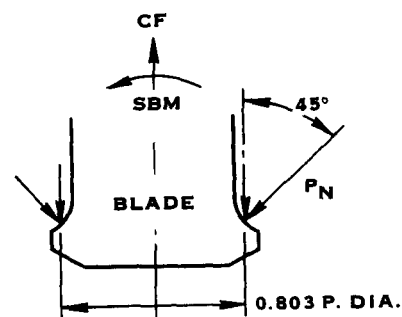
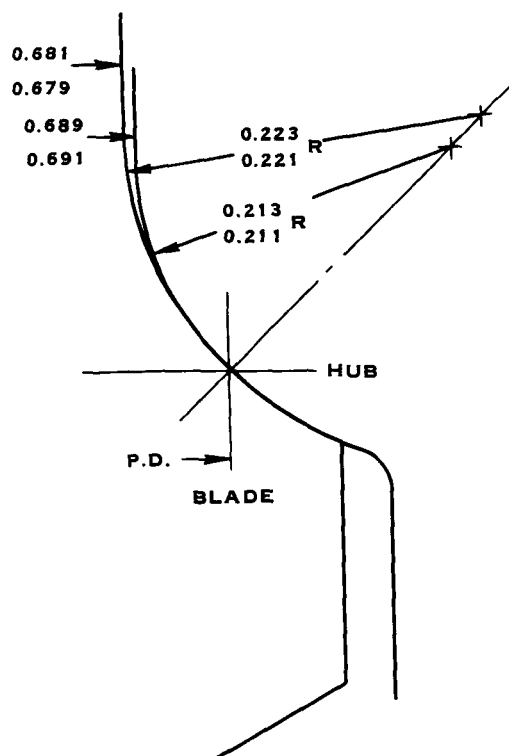


FIGURE 7-2. BLADE RETENTION LOADS



$$CF = 5486 \text{ LB} \quad SBM = 910 \text{ IN-LBS}$$

$$P_N = CF / \cos 45^\circ + 4 \cdot SBM / (PD \cdot \cos 45^\circ)$$

$$P_N = 14,169 \text{ LBS}$$

$$\text{LOAD/LINEAR IN.} = P_N / (\pi \cdot PD) = 5617 \text{ LB/IN.}$$

USING LB/IN. AND RETENTION DIMENSIONS SHOWN,
THE CONTACT STRESS COMPUTER PROGRAM
RESULT IS 45,800 PSI MAX.

AS LOW CYCLE FATIGUE, $22,900 \pm 22,900$ PSI

FIGURE 7-3. BLADE RETENTION STRESSES

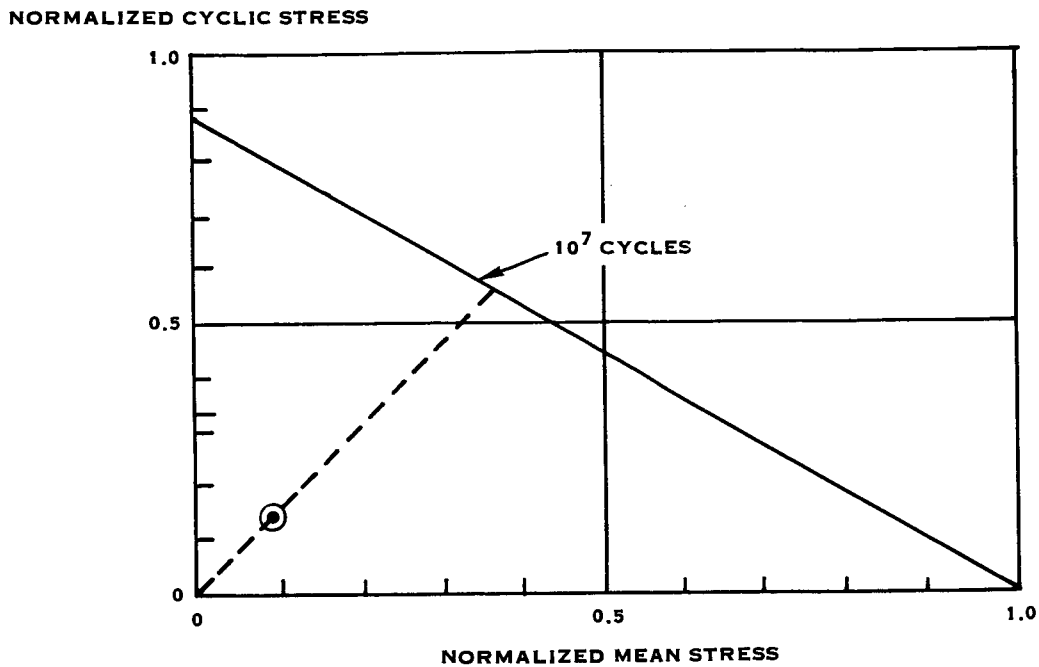


**FIGURE 7-4. GOODMAN DIAGRAM CONTACT STRESS ALLOWABLE
6AL-4V TITANIUM 35 RC BLADE RETENTION**

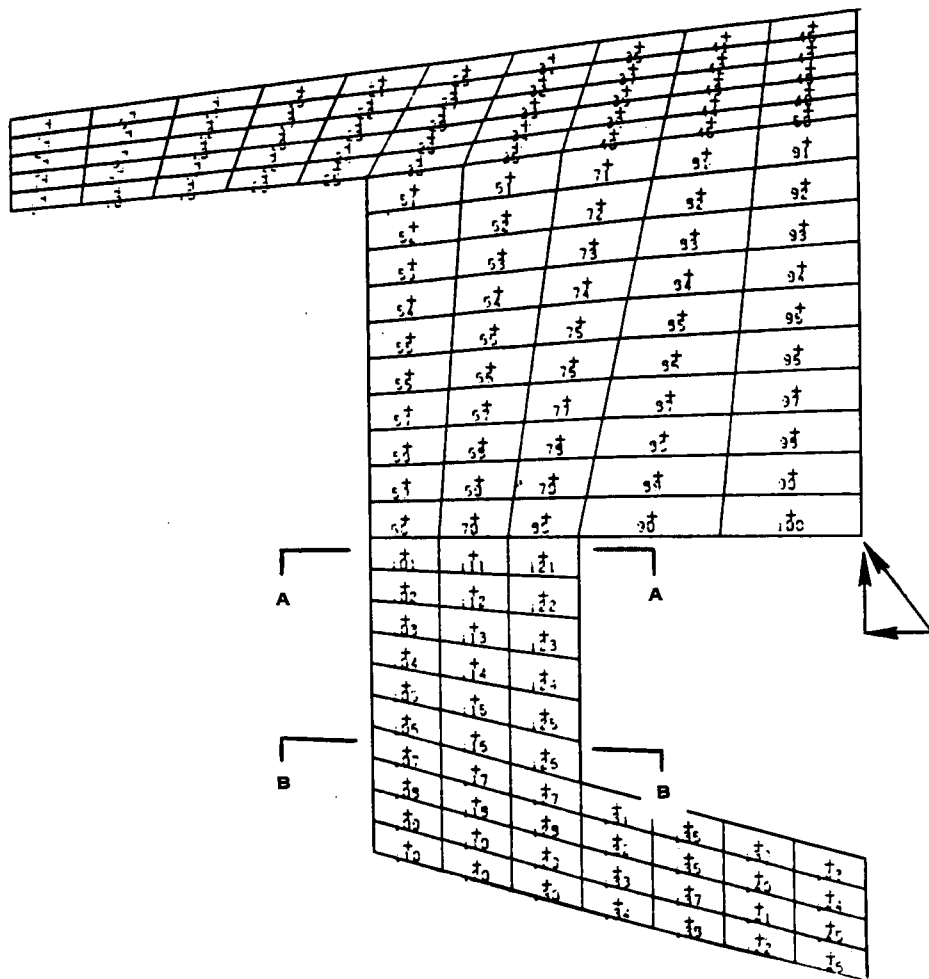


FIGURE 7-5. FORWARD HUB 2-D MODEL

ORIGINAL PAGE IS
OF POOR QUALITY

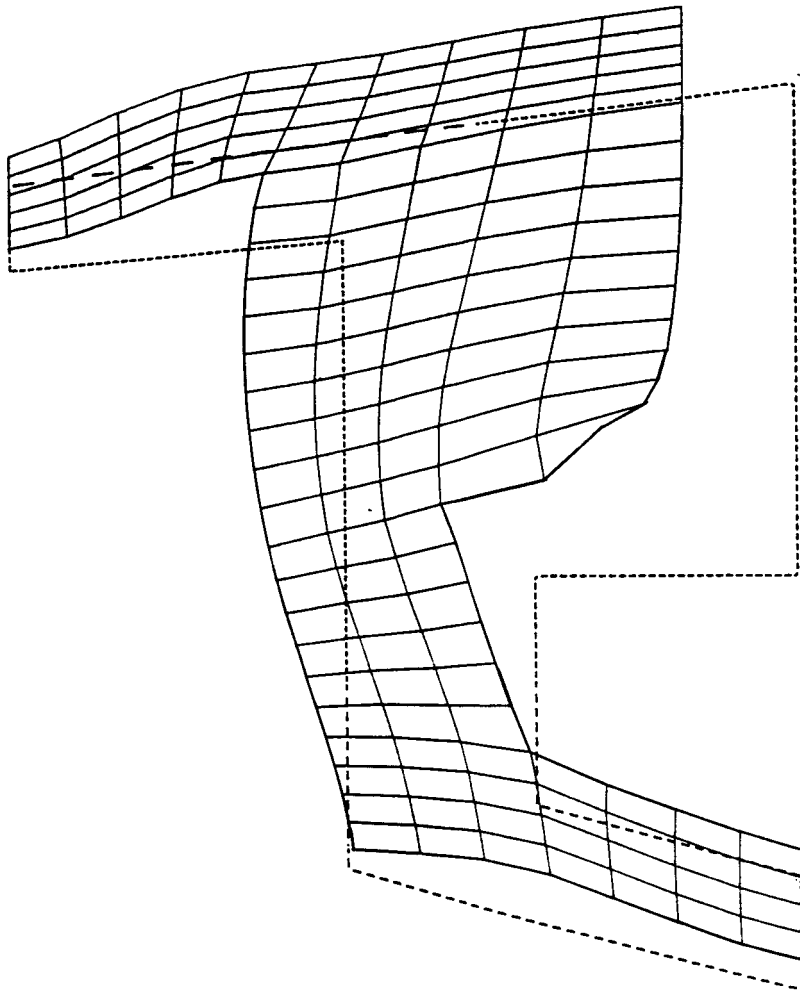


FIGURE 7-6. FORWARD HUB DEFLECTED SHAPE

NORMALIZED CYCLIC STRESS

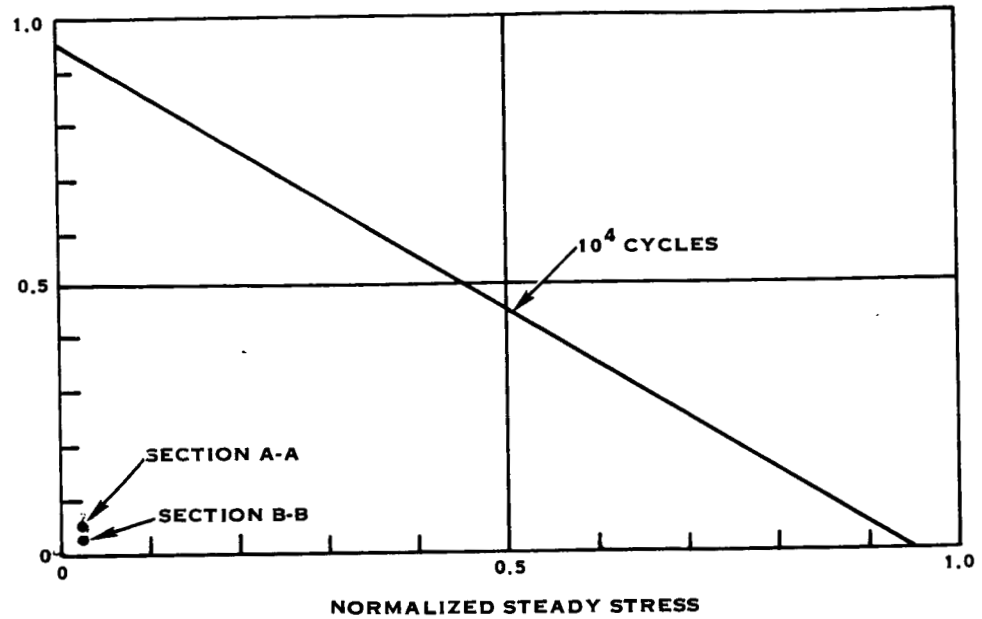


FIGURE 7-7. HUB LIP STRESSES (AMS 6415 40-44 RC)

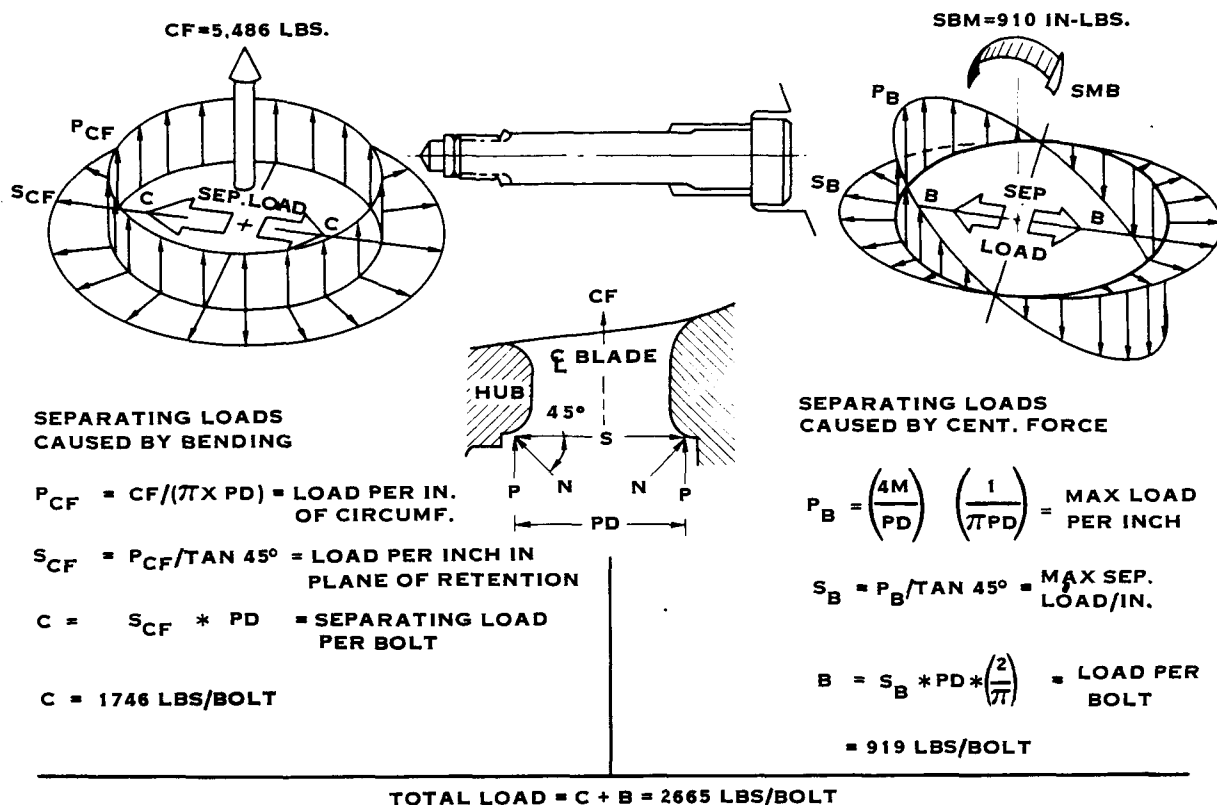
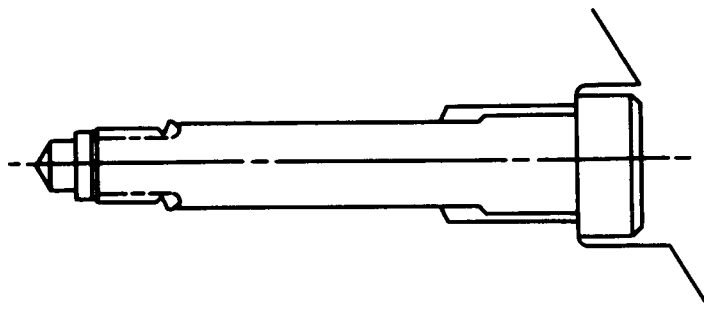


FIGURE 7-8. SR7 BOLT LOADS

**BOLT STRESS**

$$LT = C + B$$

$$LT = 1746 + 919 = 2665 \text{ LBS}$$

0.375-24 THREAD

STRESS AREA - 0.0665 IN²

$$S = LT/A = 40,100 \text{ PSI}$$

YIELD MS

$$MS = (140,000/40,100) - 1$$

$$MS = 249\%$$

REQUIRED PRELOAD TORQUE

$$T = f \cdot D \cdot L$$

 f = COMBINED FRICTION = 0.147

$$T = 0.147 \cdot 0.375 \cdot 2665$$

$$T = 147 \text{ IN-LB (MINIMUM)}$$

FIGURE 7-9. SR7 BOLT STRESS

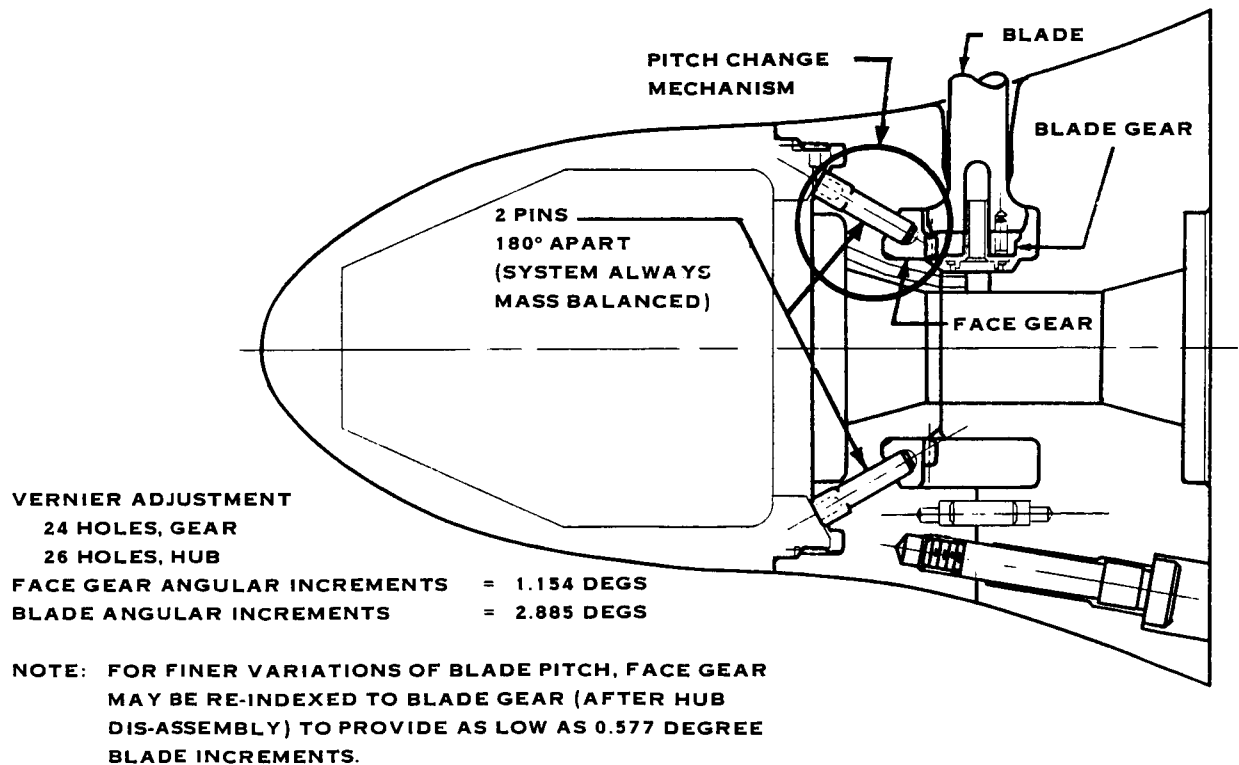


FIGURE 8-1. PITCH CHANGE DETAIL SKETCH

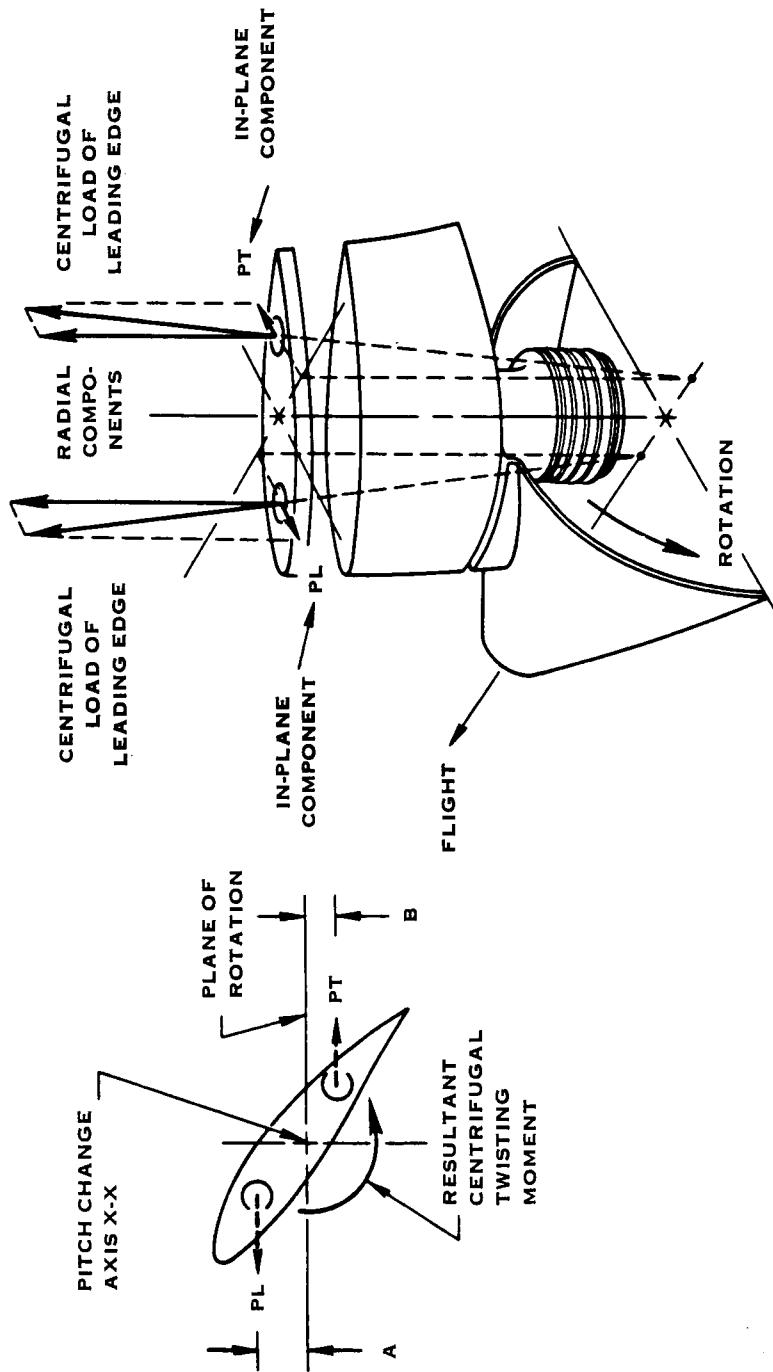


FIGURE 8-2. ORIGIN OF CENTRIFUGAL TWISTING MOMENT

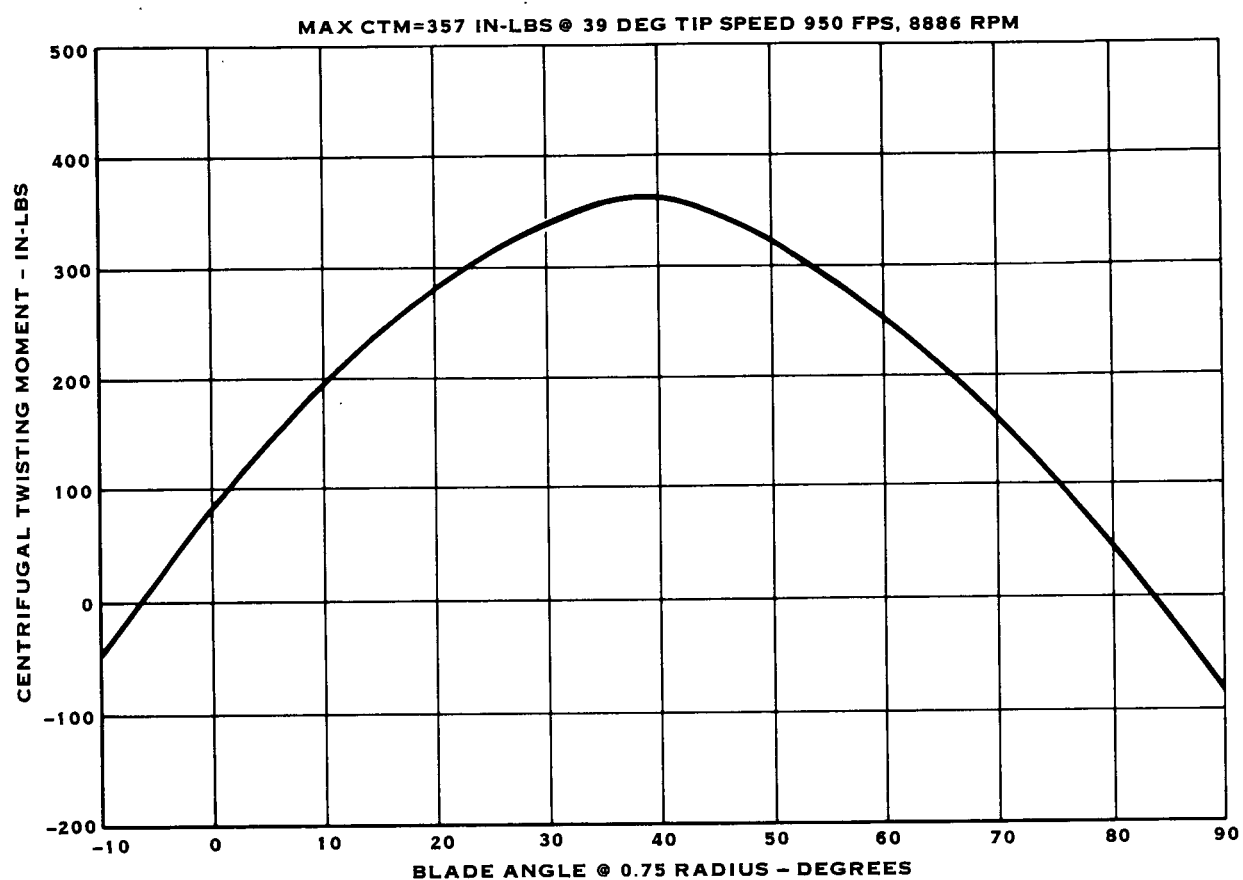
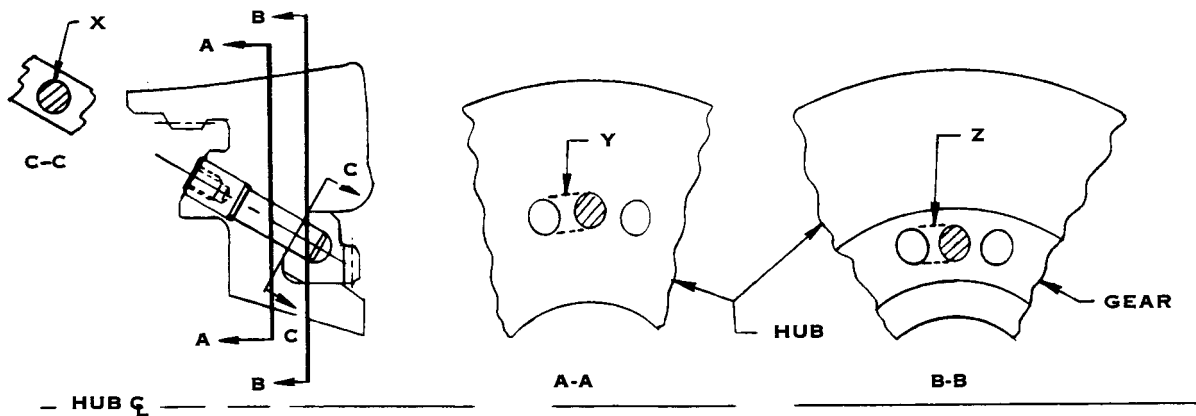


FIGURE 8-3. SR7 BLADE CENTRIFUGAL TWISTING MOMENT

**DESIGN PHILOSOPHY**

- USE MAXIMUM TEST LOADS
(TOTAL TWIST MOMENT @ 950 FPS)
- USE 2 IDENTICAL PINS, 180° APART
- DESIGN FOR BELOW YIELD STRESS:
 - 1) FOR LOAD ON ONE PIN,
COEF OF FRICTION = 0.05
 - 2) LOAD SHARED, 2/3 ON ONE PIN
ASSUME NO FRICTION

X	- SHEAR AREA PIN - 0.049 IN ²
Y	- SHEAR AREA HUB - 0.334 IN ²
Z	- SHEAR AREA GEAR - 0.150 IN ²
N	- NUMBER OF BLADES
PDF	- PITCH DIA. FACE GEAR
PDS	- PITCH DIA. BLADE GEAR
PDI	- DIA. OF GEAR SHEAR SURFACE
TTM	- BLADE TWISTING MOMENT
LUG LOAD	= $N \cdot TTM \cdot PDF \cdot (PDS/2 \cdot PDI)$
(1 PIN)	= $8 \cdot 248 \cdot 2.50 / (0.5 \cdot 2.72)$
LUG LOAD	= 3647 LB.

FIGURE 8-4. PITCH ADJUSTMENT PIN - SHEAR STRESSES

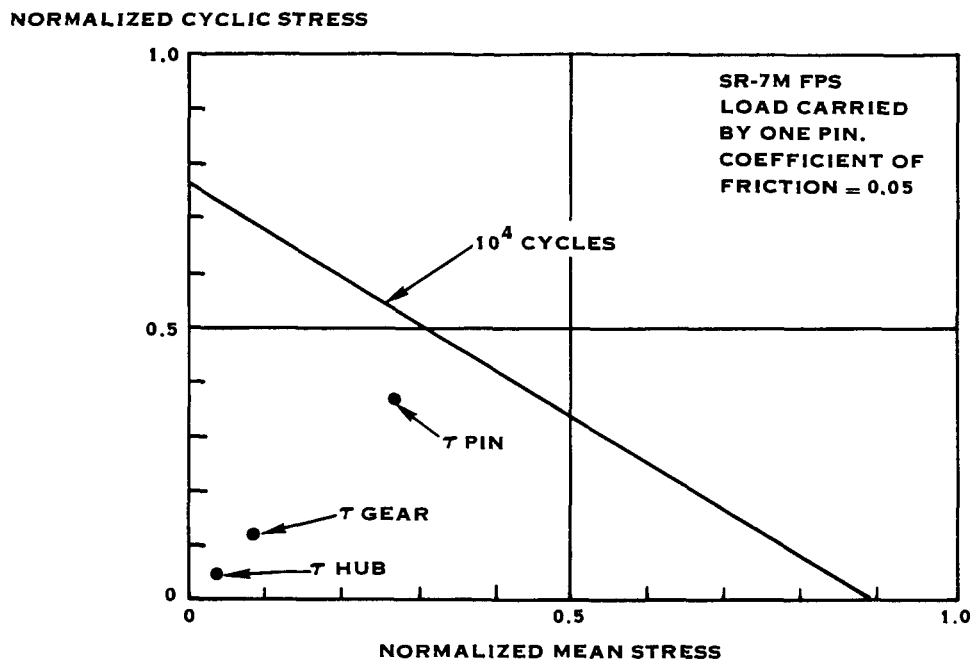
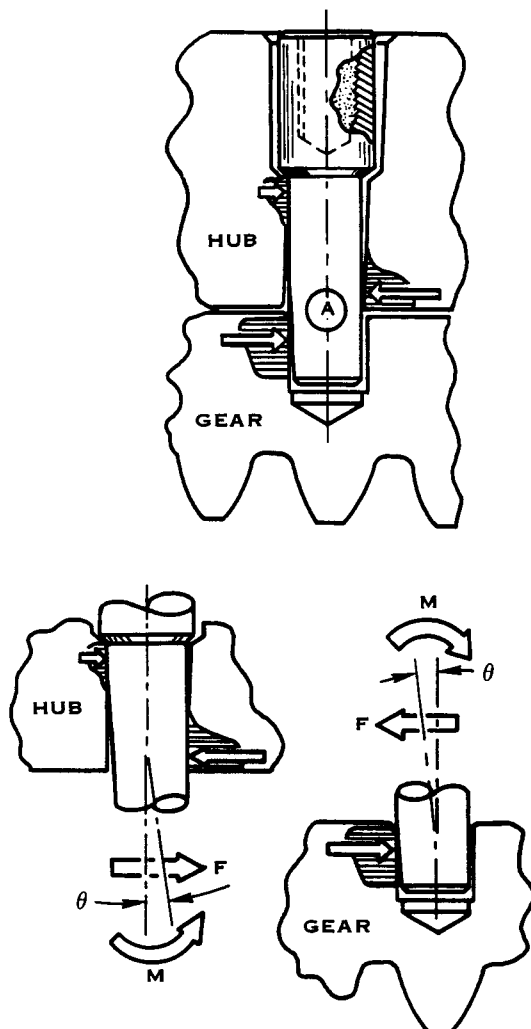


FIGURE 8-5. SHEAR STRESS GOODMAN DIAGRAM (AMS 6415 40-44 RC)



STRESS CALCULATIONS

- RAN HS COMPUTER PROGRAM TO ANALYZE PIN IN HOLE PROBLEM
- ITERATED GEOMETRY (PIN/HOLE CLRS & ENGAGEMENT LENGTH)
- DID COMPATIBILITY STUDY FOR EACH GEOMETRY COMBINATION TO MATCH SLOPE AND MOMENT AT POINT A
- REVIEWED PIN BENDING AND PIN/HOLE CONTACT STRESSES AND ITERATED UNTIL ACCEPTABLE DESIGN FOUND

FIGURE 8-6. PITCH ADJUSTMENT PIN BENDING & CONTACT STRESSES

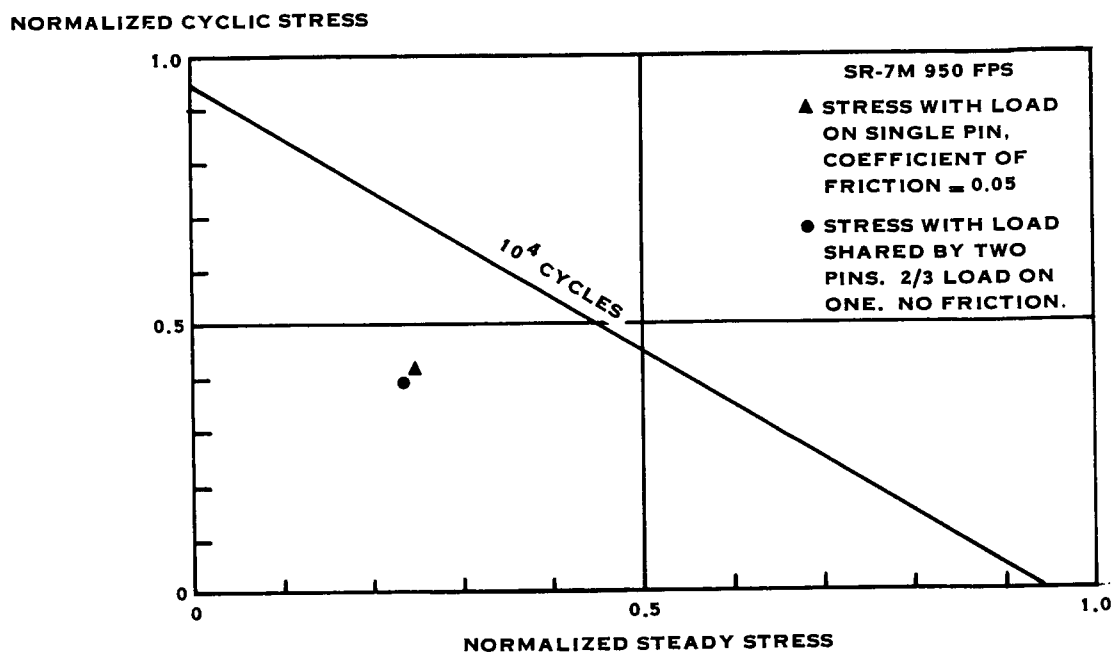


FIGURE 8-7. PITCHLOCK PIN BENDING STRESS GOODMAN DIAGRAM (AMS 6415 40-44 RC)

NORMALIZED CYCLIC HERTZ STRESS

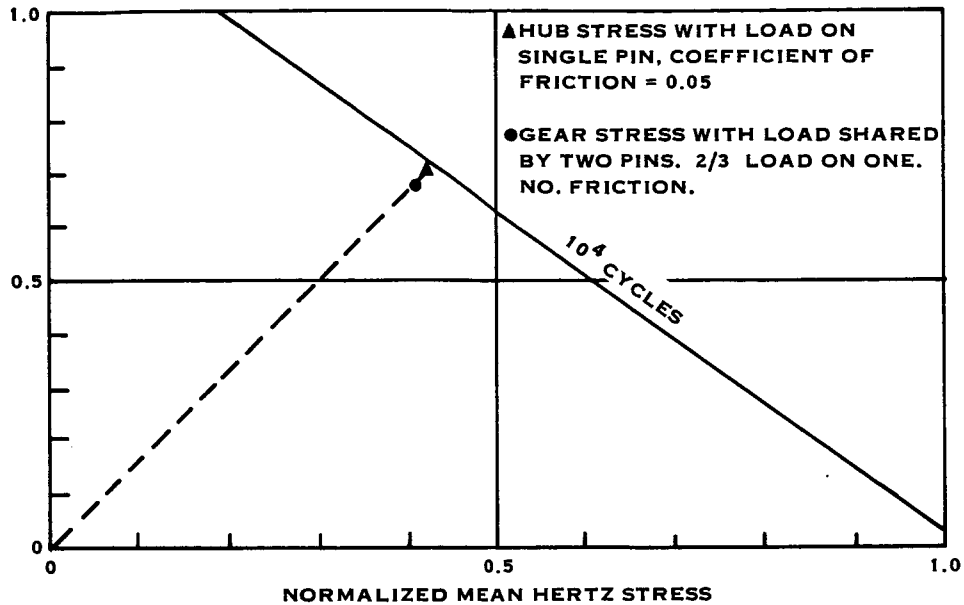


FIGURE 8-8. HERTZ CONTACT STRESS ALLOWABLE (AMS 6415 40-44 RC)

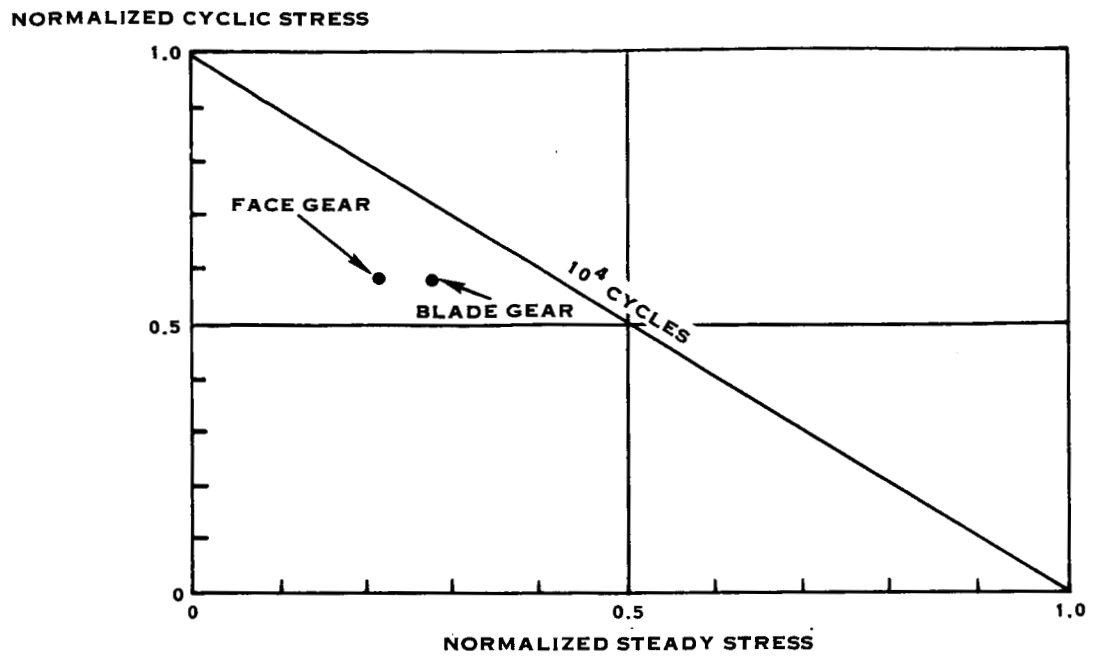


FIGURE 8-9. GOODMAN DIAGRAM AMS 6415 40-44 RC GEAR STRESSES

APPENDIX C
LIST OF TABLES

- 8-1. Model Design Conditions Analyzed
- 4-1. Iteration Summary, Stability and Frequencies
- 6-1. Aeroelastic Model Blade Load Summary
- 6-2. Aeroelastic Model and SR-7L Blade Frequencies.

TABLE 3-1. MODEL DESIGN CONDITIONS ANALYZED

SR-7A AERO/ELASTIC MODEL

<u>PARAMETERS</u>	1 JETSTAR DES/CR	2 WIND T. PERFM	3 WIND T. MAX RPM
SHP/D**2	32.0	120.0	0.0
FWD VEL	0.80 MN	0.80 MN	0.80 MN
ALTITUDE (FT)	35,000	7520 EQ	7520 EQ
TIP SPEED (FPS)	800	911.7	950
RPM	7484	8622	8886
EXCIT FACTOR	0.0	0.0	0.0
BETA 3/4 (DEG)	57.57	57.57	VARIES*
HORSEPOWER	133.4	501	"
THRUST (LBS)	75	244	"

* BETA 3/4 OF 39 DEG GIVES MAXIMUM C.T.M.

TABLE 4-1. ITERATION SUMMARY, STABILITY AND FREQUENCIES

		ONSET OF FLUTTER	RESONANT FREQUENCIES (RELATIONS)					
INTERACTIONS TO MATCH PRELIMINARY SR-7L BLADE	> LAP PDR (9 FT DIA)	0.92 MN	○	○	○		○	○
	● MODEL, EXACT-SCALE FEA, .72 IN. DIA. SHANK	0.79 MN	□		□	□		□
	● MODEL, EXACT-SCALE FEA, .625 IN. DIA. SHANK	0.88 MN	□	□	□		□	□
	● MODEL 7, NEW CONST FEA, PDR GEOM	0.95 MN	□	□	□		□	□
INTERACTIONS TO MATCH FINAL SR-7L BLADE	> LAP DDR BLADE (9 FT DIA)	0.79 MN	◇	◇	◇		◇	◇
FINAL SELECTED	● MODEL 8, NEW FEA, DDR DEFL GEOM, .625 SHANK (± 75° GRAPHITE)	0.85 MN	▽	▽	▽		▽	▽
	● MODEL 9, SAME AS 8 EXCEPT .68 DIA SANK, (± 75° GRAPHITE)	0.55 MN	▽	▽	▽		▽	▽
	● MODEL 9C, SAME AS 9 EXCEPT CORRECTED GRAPHITE TO 0.80 DEG	0.82 MN	▽	▽	▽		▽	▽
	● MODEL 10, SAME AS 9C EXCEPT .66 DIA SHANK, ± 25° GRAPHITE	0.55 MN	▽	▽	▽		▽	▽
	● MODEL 11 SAME AS 9C EXCEPT .66 DIA SHANK, ADDED MASS LE	0.83 MN	▽	▽	▽		▽	▽
			2P	3P	4P		5P	6P

TABLE 6-1. AEROELASTIC MODEL BLADE LOAD SUMMARY

CONDITION	PROP SPEED, RPM	B, DEG	CENTRIFUGAL FORCE, FZ NEWTONS (LBS)	SHEAR FORCES, NEWTONS (LBS)			(β) ANGLE, DEG	BENDING MOMENTS, N·M (IN·LBS)			(γ), ANGLE, DEG
				FX	FY	FR		MX	MY	MR	
10 668 M CRUISE (35 000 FT)	7484	57.57	17 392 (3 910)	372 (83.7)	41.4 (9.3)	375 (84.2)	174	29.8 (264)	1.6 (1.4)	29.8 (264)	267
WIND TUNNEL - COND. 1	8622	57.57	23 179 (5 211)	770 (173)	120 (27)	778 (175)	171	29.4 (260)	23.4 (207)	37.5 (332)	231
WIND TUNNEL - COND. 2	8886	57.57	26 620 (5 935)	818 (184)	129 (29)	827 (186)	171	31.2 (276)	24.9 (220)	39.9 (353)	231
TAKEOFF CLIMB	7484	38.36	17 392 (3 910)	471 (106)	80 (18)	480 (108)	189	31.9 (282)	14.2 (126)	34.9 (309)	265
VACUUM CONDITION *	8886	37.57	24 402 (5 486)	16.5 (3.7)	-62.7 (-14.1)	65 (14.6)	275	91.5 (810)	-46.9 (-415)	102.8 (910)	317

* SAME ANGLE SETTING AS TAKEOFF/CLIMB

$$FR = \sqrt{FX^2 + FY^2}, \quad MR = \sqrt{MX^2 + MY^2}$$

TABLE 6-2. AEROELASTIC MODEL AND SR-7L BLADE FREQUENCIES

<u>MODE</u>	<u>SR-7A FREQ, Hz</u>	<u>SR-7L FREQ, Hz</u>	<u>SR-7A FREQ X TIP RADIUS, CM-CYCLES/SEC (IN-CYCLES/SEC)</u>	<u>SR-7L FREQ X TIP RADIUS, CM-CYCLES/SEC (IN-CYCLES/SEC)</u>	<u>DIFF. (%)</u>
1	207.5	43.2	6457 (2542)	5926 (2333)	+9.0
2	376.0	80.1	11699 (4606)	10986 (4325)	+6.5
3	468.6	101.0	14580 (5740)	13856 (5455)	+5.2
4	642.5	148.3	19990 (7870)	20335 (8006)	-1.7
5	782.3	168.6	24341 (9583)	23127 (9105)	+5.2

APPENDIX D
DESIGN LAYOUTS

**ORIGINAL PAGE IS
OF POOR QUALITY**

THE MEANLINE OF CONTACT
BETWEEN BLADE & HUB MUST MAKE A
CONTACT ANGLE OF $45 \pm 5^\circ$.

ITEM 6 ID **A** _____
ITEM 6 DATUM **B**

SECTION A-A
SCALE: 2/1

VIEW B
SCALE: 20/1

④- SECTION H-H WITH
ITEM ③ OMITTED, SCALE 1:1

ITEM 10, SCALE 2:1

SPINNER & HUB CO-ORDINATES
ITEMS 1, 2, 3, 4 \triangleleft 4
004 TOTAL TOL. ON SURFACE OF
BASIC CONTOUR

AXIAL LG R ²	ZIA T ²
BSC	BSC
2.000	2.000
0.960	2.149
0.295	1.284
2.322	1.780
0.749	2.178
0.973	2.310
1.903	1.831
2.337	3.947
3.471	4.578
4.605	4.877
5.733	4.791
6.410	5.236
5.174	5.125
6.180	5.965
	5.808
16.347	7.332

VIEW F SCALE 2:1

REAR VIEW, ITEM ①

THE PURPOSE OF THIS LAYOUT IS TO DEFINE A HUB SPINNER AND RETENTION FOR THE SR-7 AERO-ELASTIC MODEL

10	10	BLADE	789719	7. SPIN. FAN 66 GEORGIN SMALL FAN	REF. L-13231-12, 789719
11	11	BLADE CENTER	785334-2		
12	12	LOCK W/TH MASH BUSH 1/4"	765378		
13	13	SPACER	765378	AM56415, 26-00-R, REF	L-13231-11
14	14	SEAT, SPRING	765306-4	AM56415, 14-00-AC, REF	
15	15	WASHER, IN WAVE	765306-3	CAE 1025, REF	
16	16	SCREW, 1/4" D	785334-1	CAE 1025, REF	
17	17	WASHER, FLAT	57455A31	CRES	
18	18	PLUG, VLN IN 789719	789719-60	3 POINT ATTEL 10-1	
19	19	FLAT WASHER	075320-013	102774, 25-00-05, REF	
20	20	FLAT WASHER	57455A31	102774, 25-00-05, REF	
21	21	PIN, WADNESS	674828-0-3	102774, 25-00-05, REF	
22	22	PIN, WADNESS	674828-0-3	102774, 25-00-05, REF	
23	23	GEAR, FACE	787742-1	AM56415, 26-00-R, REF	
24	24	GEAR, FACE	787742-1	AM56415, 26-00-R, REF	
25	25	BLK, SPINNER	787742-1	AM56415, 26-00-R, REF	
26	26	BLK, SPINNER	787742-1	AM56415, 26-00-R, REF	
27	27	SPINNER	787742-1	AM56415, 26-00-R, REF	
28	28	WASHER, FLAT	57455A31	AM56415, 26-00-R, REF	
29	29	WASHER, FLAT	57455A31	AM56415, 26-00-R, REF	
30	30	WASHER, FLAT	57455A31	AM56415, 26-00-R, REF	
31	31	WASHER, FLAT	57455A31	AM56415, 26-00-R, REF	
32	32	WASHER, FLAT	57455A31	AM56415, 26-00-R, REF	
33	33	WASHER, FLAT	57455A31	AM56415, 26-00-R, REF	
34	34	WASHER, FLAT	57455A31	AM56415, 26-00-R, REF	
35	35	WASHER, FLAT	57455A31	AM56415, 26-00-R, REF	
36	36	WASHER, FLAT	57455A31	AM56415, 26-00-R, REF	
37	37	WASHER, FLAT	57455A31	AM56415, 26-00-R, REF	
38	38	WASHER, FLAT	57455A31	AM56415, 26-00-R, REF	
39	39	WASHER, FLAT	57455A31	AM56415, 26-00-R, REF	
40	40	WASHER, FLAT	57455A31	AM56415, 26-00-R, REF	
41	41	WASHER, FLAT	57455A31	AM56415, 26-00-R, REF	
42	42	WASHER, FLAT	57455A31	AM56415, 26-00-R, REF	
43	43	WASHER, FLAT	57455A31	AM56415, 26-00-R, REF	
44	44	WASHER, FLAT	57455A31	AM56415, 26-00-R, REF	
45	45	WASHER, FLAT	57455A31	AM56415, 26-00-R, REF	
46	46	WASHER, FLAT	57455A31	AM56415, 26-00-R, REF	
47	47	WASHER, FLAT	57455A31	AM56415, 26-00-R, REF	
48	48	WASHER, FLAT	57455A31	AM56415, 26-00-R, REF	
49	49	WASHER, FLAT	57455A31	AM56415, 26-00-R, REF	
50	50	WASHER, FLAT	57455A31	AM56415, 26-00-R, REF	
51	51	WASHER, FLAT	57455A31	AM56415, 26-00-R, REF	
52	52	WASHER, FLAT	57455A31	AM56415, 26-00-R, REF	
53	53	WASHER, FLAT	57455A31	AM56415, 26-00-R, REF	
54	54	WASHER, FLAT	57455A31	AM56415, 26-00-R, REF	
55	55	WASHER, FLAT	57455A31	AM56415, 26-00-R, REF	
56	56	WASHER, FLAT	57455A31	AM56415, 26-00-R, REF	
57	57	WASHER, FLAT	57455A31	AM56415, 26-00-R, REF	
58	58	WASHER, FLAT	57455A31	AM56415, 26-00-R, REF	
59	59	WASHER, FLAT	57455A31	AM56415, 26-00-R, REF	
60	60	WASHER, FLAT	57455A31	AM56415, 26-00-R, REF	
61	61	WASHER, FLAT	57455A31	AM56415, 26-00-R, REF	
62	62	WASHER, FLAT	57455A31	AM56415, 26-00-R, REF	
63	63	WASHER, FLAT	57455A31	AM56415, 26-00-R, REF	
64	64	WASHER,			

7 FOLDOUT FRAME

APPENDIX D (CONTINUED)

ORIGINAL PAGE IS
OF POOR QUALITY

[illegible]

ORIGINAL PAGE IS
OF POOR QUALITY

ORIGINAL PAGE IS
OF POOR QUALITY

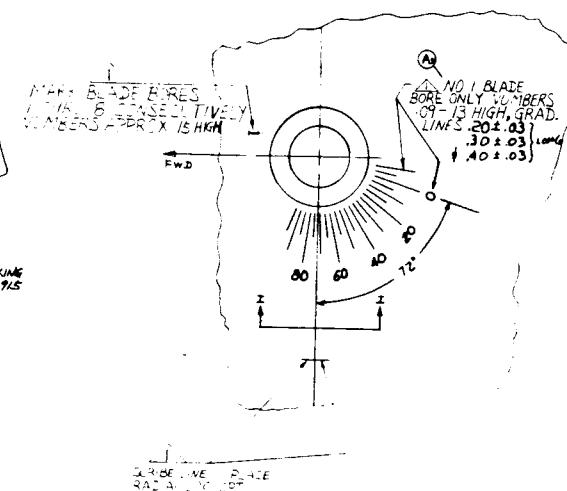
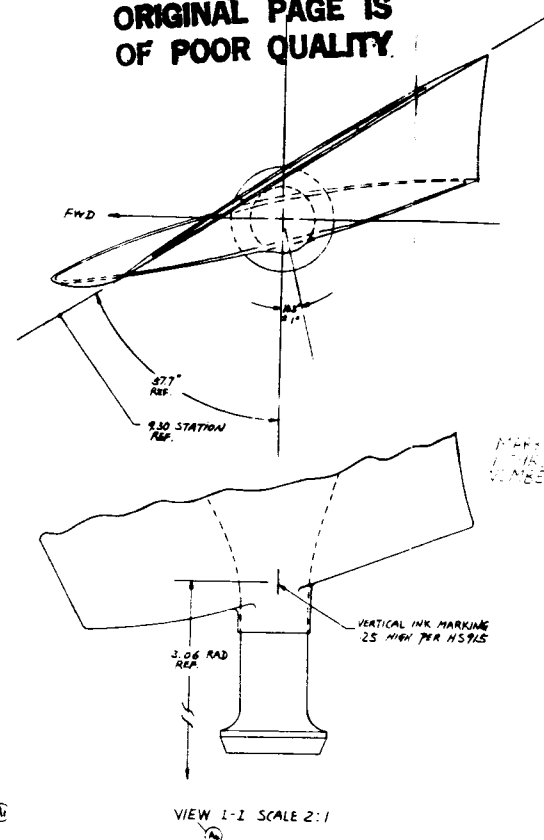
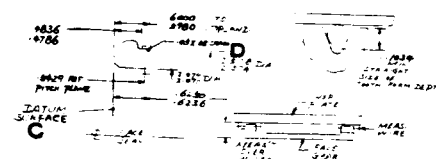
[illegible][illegible]

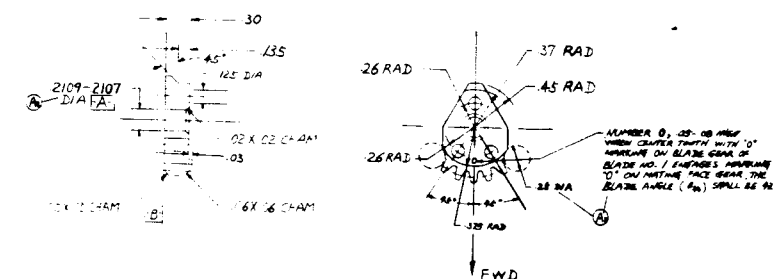
TABLE 1		MACHINE	
W/EN SPAYEAS		THEN RADIAL VESS	
C/ER 3 TEETH IS		INCL ECC C/ER NO	
100 WIRE CHALL			
DATA	430	4912	4924
4855	4908	4912	4922
4872	4905	4907	4919
4881	4902	4907	4917
4886	4900	4908	4918
4883	4897		

VIEW D-I
SCALE 2/1
HUB ONLY

7 FOLDOUT FRAME



APPENDIX 7 INSPECTION DATA



ITEM 6
SCALE 2/1

FOLDOUT FRAME

REFERENCES

1. Wolowicz, C.H., Bowman, J.S., Gilbert, W.P., "Similitude Requirements and Scaling Relationships as Applied to Model Testing", NASA Technical Paper 1435, August 1979
2. Hunt, G.K., "Similarity Requirements for Aeroelastic Models of Helicopter Rotors", C.P. No. 1245 Aeronautical Research Council Current Papers, Structures Dept., R.A.E., Farnborough, 1973
3. Scroton, C., Lamborne, N.C., "Similarity Requirements for Flutter Model Testing", Agard Manual on Aeroelasticity, Volume IV, Chapter 6, 1960

1. Report No. NASA CR174791		2. Government Accession No.		3. Recipient's Catalog No.	
4. Title and Subtitle SR-7A Aeroelastic Model Design Report				5. Report Date	
				6. Performing Organization Code 73030	
7. Author(s) D. Nagle, S. Auyeung, J. Turnberg				8. Performing Organization Report No. HSER-9251	
9. Performing Organization Name and Address Hamilton Standard Division United Technologies Corporation P.O. Box 1000 Windsor Locks, Connecticut 06096				10. Work Unit No.	
				11. Contract or Grant No. NAS 3-23051	
12. Sponsoring Agency Name and Address National Aeronautics and Space Administration Washington, D.C. 20546				13. Type of Report and Period Covered Contractor Report	
				14. Sponsoring Agency Code	
15. Supplementary Notes Project Manager David A. Sagerser, Advanced Turboprop Project Office, NASA Lewis Research Center, Cleveland, Ohio 44135					
16. Abstract A scale model was designed to simulate the aeroelastic characteristics and performance of the 2.74 meter (9 ft.) diameter SR-7L blade. The procedures used in this model blade design are discussed. Included in this synopsis is background information concerning scaling parameters and an explanation of manufacturing limitations. A description of the final composite model blade, made of titanium, fiberglass, and graphite, is provided. Analytical methods for determining the blade stresses, natural frequencies and mode shapes, and stability are discussed at length. Also within the scope of this program was a design of the model hub, spinner, and pitch change mechanism. This report contains a description of this hardware, as well as a summary of the hub and pitch change loads and stresses.					
17. Key Words (Suggested by Author(s)) Prop-Fan Aeroelastic Model Structural Design			18. Distribution Statement [REDACTED] October 15, 1988		
19. Security Classif. (of this report) Unclassified		20. Security Classif. (of this page) Unclassified		21. No. of Pages 126	
22. Price*					